Iridescence and Circular Dichroism in Cellulose Nanocrystal Thin Films

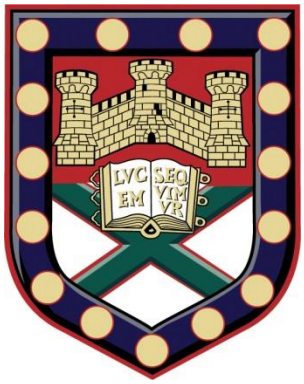

Daniel James Hewson

School of Physics

University of Exeter

A thesis submitted for the degree of

Doctor of Philosophy

September 2017

Structural Colouration in Cellulose Nanocrystal Thin Films

Submitted by Daniel James Hewson to the University of Exeter as a thesis for the degree of Doctor of Philosophy in Physics
July 2017

I certify that all material in this thesis which is not my own work has been identified and that no material has previously been submitted and approved for the award of a degree by this or any other University.

Signature: ……..

Date:……...

Abstract

Only in recent times has the true potential of cellulose as a high-end functional and sustainable material been realised. As the world's most abundant resource cellulose has been utilised by man throughout history for timber, paper and yarns. It is found in every plant as a hierarchical material and can be extracted and converted into fibres which are of great use, especially in the form of nanofibrous materials. This thesis has focused on the utilisation and ability of cellulose nanocrystals (CNCs) to generate structural colour in fabricated thin films. This has been achieved in two ways: Firstly, the natural morphology of CNCs and their ability to form a suspension have been applied to a layer-by-layer (LbL) regime to produce tunable Bragg reflecting thin films. Secondly, a novel technique combining profilometry and spectroscopy has been developed to estimate the distribution of CNCs within EISA thin films and correlate this with the optical properties of the film.

This thesis reports the successful fabrication of synthetic CNC LbL Bragg reflecting thin films. The film was compiled using an additive layer-by-layer technique which allowed the construction of a multi-layered thin film and control over individual layer thicknesses and refractive index.

Also reported is the discovered reflection of both left and right handed circularly polarised light (CPL) from CNC EISA thin films. These reflections were found to correlate with CNC distribution within the thin films. The distribution of CNCs was estimated using a novel technique which combined spectroscopically measured film absorbance as a function of the volume of the film area under investigation. The specific volumes were calculated using profilometry measurements and the beam spot size used in the spectroscopy measurements.

Acknowledgements

I have been very much inspired by the incredible focus, enthusiasm and the dedication to science of my supervisors, Professor Stephen Eichhorn and Professor Peter Vukusic. Without their guidance and readily shared experience the work in this thesis could not have been achieved; so, to them I express my sincere gratitude. I owe a great debt to my wife and children whose support; patience and encouragement have been unfailing and have spurred me on in times of difficulty and discouragement. I would also like to thank my parents for their temporal support and for providing much needed holidays! I must thank Dr Sebastian Mouchet for taking the time to cross the t's and dot the i's of this thesis and for his homeland, Belgium for making good things to eat. Thank you to Dr Luke McDonald, Dr Tim Starkey and Dr Matt Nixon for their amusing banter, curry nights and no less important photonics advice and support. I have had the privilege of working with two research groups, The Cellulose and Natural Materials Research group and the Natural Photonics Research group. The collected experience of the two groups has greatly influenced my work; the friendships I have developed within each group have made my life as a PhD student all the more enjoyable and rewarding. I am very grateful for the expertise and collaborative efforts of Professor Jamie Grunlan and Dr Ping Tzeng at the Polymer Nanocomposites Laboratory and Dr Christian Hacker at the Bio-Imaging Suite here at the University of Exeter. I must also thank Nick Cole for the skill and effort he puts into everything he builds and particularly thank him for building (from scratch) the goniometer used to obtain data presented in this thesis. To keep me going I have eaten much cake that has been lovingly provided by family members, cake in which I have enjoyed with David Richards, a good friend who went on before me to complete his thesis and whose valuable advice has helped me and my efforts to present my own.

Contents

List of Figures

List of Tables

List of Abbreviations

ARS	Angle resolved spectrophotometry
CIE	International Commission on Illumination
CNC	Cellulose Nanocrystal
CP	Circular polarisers
CPL	Circularly polarised light
DP	Degree of polymerisation
EISA	Evaporation induced self-assembly
LbL	Layer-by-layer
LCP	Left handed circularly polarised
MSP	Microspectrophotometry
PBG	Photonic band gap
POM	Polarised optical microscopy
RCP	Right handed circularly polarised
RGB	Red, green, blue
RI	Refractive index
SEM	Scanning electron microscopy
TEM	Transmission electron microscopy

Chapter 1 Introduction

The human brain interprets the response of incident waves of visible light on the retina of the eye. These interpretations generate the perception in the human mind of the form, texture and colouration of objects from which light waves propagate. Understanding of what it is exactly that generates the idea of colour is still developing[1], but what is known is the effective role it plays in influencing human behaviour[2–5]. This effect is not limited to humans, colour informs decision making across the animal kingdom and has the power to invoke emotional and physiological responses as animals and humans seek a mate[6], warn off predators or decide what to eat[7]. The human response is especially strong when the colour observed is particularly striking as is the case with structurally coloured stimuli. Unlike the more common colouration of pigments and dyes, structural colour is generated by the interference of visible light with physical structures possessing nanoscale dimensions. Such structures give rise to iridescent colour and vary in complexity from simple thin films to intricate gyroid structures both of which are found in nature. Natural iridescent systems notable for their variety and brilliance have inspired scientists to mimic their structures and manipulate the resultant properties. The mechanisms that give rise to these colours are of interest to researchers representing a wide variety of primary fields[8–10]. Many examples of iridescent colour are found in Coleoptera beetles[11–13], butterflies[14,15] and bird feathers[8,16]. The optically brilliant appearance of many beetles is derived from

photonic structures found in the species integument[13,17] which in some cases have also been found to show fluorescent behaviour[18]. The simplest form of photonic structure associated with the beetle exterior comprises very thin layers possessing an alternating contrasting refractive index (RI). Constructive interference of reflected light, or Bragg reflection, can be achieved by such systems when the optical thickness of each periodic layer times the RI is on the order of $\lambda/4$ and the viewing angle is close to 90°[19,20]. Successful, affordable fabrication of such structures could make structurally coloured systems useful for sensing[21,22], the potential of which has been demonstrated by Deparis *et al*. (2014).[23] Other potential applications are optical filters[24,25] and the widespread replacement of pigment-based coatings[26,27]. Structurally coloured systems in beetles have been found to show variation in colour appearance when liquid is introduced[18,28] demonstrating their potential for sensing applications. The iridescent effect can only be generated by structural systems and is particularly conspicuous to the human eye which also lends them to industries where aesthetics are important. The complexity of these structures also makes them useful for security where marks of authentication are required. The development of the technique to apply layers of nanoscale thickness to given substrates, known as Layer by Layer assembly (LbL), has made fabricating Bragg reflecting systems cost efficient and has opened up the use of a broad range of materials[24,29]. Cellulose nanocrystals (CNCs) are one material shown to be effective for LbL films[30] and one that has the potential to improve the process cost and efficiency. Cellulose is the main structural component in all plant life making it the most abundant material on the planet. The inherent mechanical properties of cellulose give plants their structural integrity and have long been exploited technologically in useful materials such as paper and fibre yarns. CNCs, extracted from plant cell walls by acid hydrolysis possess

excellent mechanical, thermal and electrical properties that are finding applications in many high end products[31,32]. In addition, cellulose nanocrystal suspensions are known to exhibit interesting optical properties[33], self-assemble in confinement[34] and even display colouration in flexible and shape memory films[35,36]. Such properties are derived from liquid crystalline phases of the rod-like cellulose nanocrystals which are believed to possess an intrinsic right handed twist[37,38] and self-assemble in solution above specific concentrations. The structural ordering of self-assembling CNCs undergoes chiral twisting to form a chiral phase known as a cholesteric structure which, in the case of CNCs, possess a left handed twist[39]. Chiral structures possess optical properties that include circular dichroism, pseudo-Bragg reflections and strong rotatory power[40]. These properties are readily observed in solutions of CNCs from which the structures responsible for them can be frozen in upon evaporation of the solvent in a process called evaporation induced self-assembly (EISA). The optical properties of chiral structures are much sought after in responsive photonic material technologies[41] and CNC iridescent films offer a unique way of generating visible colour appearance using a material that is renewable and sustainable[42]. The problem in producing CNC thin films is achieving homogeneity throughout. Between the drying mechanics and the self-assembly process structural defects and anomalies are inevitable which impact on the optical efficiency of the film. Using the LbL method to produce Bragg reflectors is one way around this as it ensures homogenous layering, but at the sacrifice of some of the optical properties. The dichroic properties are based on the presence of cholesteric structures, formed during the self-assembly process, but heavily influenced by the drying mechanics.

The aim of this thesis is twofold: Firstly, to investigate the use of CNCs in an LbL regime to fabricate tunable structurally coloured thin films. CNCs are a suitable material for LbL

assembly, but can their properties be utilised, using LbL to fabricate a Bragg reflecting film? Secondly, to understand how the drying mechanics of CNC droplets effects the distribution of CNC material within the EISA thin film and to explore relationships between this and the films optical properties. A variation in distribution may affect and help explain variations in optical properties across the film, particularly circular dichroism which is of particular interest to current researchers of CNC thin films[37,38,43,44]. The variation in CNC distribution may also be responsible for the development of defects in the layered structure which may be a contributing factor to variations in optical properties of the film.

The following Chapters will outline the background and theory behind the principles of structural colour, the material cellulose and the LbL process used and the experimental results of this thesis. Chapters 2-4 are dedicated to the background and theory and Chapter 5 will present the experimental methods used in this thesis. This will include the methods used to synthesise CNCs, the preparation of CNC EISA thin films, the structural and optical characterisation techniques used and the technique used to measure the CNC distribution in CNC EISA thin films. Chapters 6-7 show and discuss the results obtained from the experiments conducted and Chapter 8 presents conclusions drawn from the results along with suggestions of future work to address unanswered questions/findings.

Chapter 2 Theory of Structural Colour

2.1 Structural Colour

2.1.1 A familiar Phenomenon

The light blue of a cloudless sky is a familiar colour and one that disappears at night, despite the presence of moon and starlight. It also changes hue with the position of the sun; a phenomenon not seen in pigment based materials like grass which maintains an even green from all viewing angles. The compounds responsible for the green colouration of grass can be extracted via chemical or mechanical processing, but no blue material has ever been extracted or precipitated from the sky. Neither does the passing of jet engines disturb or distort this colour. Such characteristics are derived from a system interacting with visible light or a part of it at a given time. This interaction is manifest due to the presence of optical heterogeneities in our earth's atmosphere consisting of molecular and particulate bodies[45]. Whether molecules or particles (such as dust) are responsible has been strongly debated. In 1859 John Tyndall observed that blue wavelengths of light were polarised and scattered more strongly by clear suspensions[46]. 12 years later Lord Rayleigh

showed that the amount of light scattered is inversely proportional to the fourth power of wavelength ($1/\lambda^4$) which means that shorter wavelengths are scattered more strongly than longer wavelengths[47]. Following these investigations Tyndall and Rayleigh believed that dust particles were responsible for the scattering of shorter wavelengths of light in the earth's atmosphere.[16] However, it was realised that if this was the case then greater variation in the sky colour appearance would be observable with changes in humidity and or haze conditions. Accepting the idea that molecules were responsible was hard as they were believed to be too small (~ 0.3 nm). Einstein in 1905 derived a detailed formula to explain the scattering of light from molecules. He concluded that molecules are able to scatter light because the electromagnetic field of the light waves induces electric dipole moments in the molecules[48]. The result in earth's atmosphere is a scattering of almost linearly polarised blue light and the light is polarised more or less to a plane normal to that of the direction of the incident beam[45], which is why the blue colour disappears when viewed in the direct path of the sun. Because the light is scattered in multiple directions, the sky appears blue on earth regardless of the viewing angle. When viewing a sunset, red and orange colours are observed because blue wavelengths are scattered away from the line of sight. Einstein's work agreed with experiment but the explanation still begged the question 'why isn't the sky violet?' as violet wavelengths are shorter than blue wavelengths and would therefore be more readily scattered. The answer to this is found in the way our eyes are setup to detect colour. The cells responsible have varying sensitivities to wavelengths of visible light. This will be explained in more depth in Section 2.4 where a standard for human colour perception is outlined. Better understood but less familiar are the systems found in nature that also produce unique colouration without the use of

pigments or dyes. Mason did much to explain the distinguishing features of structural colour and the various systems that exist in nature[9,49].

Natural systems displaying structural colour can be found in the integument of beetles,[11,50–52] the scaly wings of butterflies,[14,53,54] the feathers of birds[16,55–57] and in the scales of fish[20,58–60]. Structural colouration has also been observed in fossils[61,62] of the above species. These systems consist of microscale structures possessing nanoscale periodicities that interfere with visible light. These periodic structures known as photonic crystals vary in complexity from a simple diffraction grating[63] to 3-dimensional gyroids[64,65]. Such variations produce a range of colour appearances from matt whites to bright metallics known as specular reflectors. The dielectric materials available in nature possess negligible light absorption and are utilised to generate the periodicities mentioned. Typical materials are chitin (arthropod cuticle), keratin (bird feathers) and cellulose (plant structures) and are often in contrast with air cavities or layers of pigmented material such as melanin.

2.1.2 Biological Photonic Crystals

The simplest form of photonic crystal comprises alternating layers with different RIs. This basic 1-dimensional multilayer structure is the most common mechanism utilised by biological systems to achieve iridescence. It is particularly studied in beetles[9,66,67] where scientists interested in structural colouration were particularly taken by the ‘living jewels’ – the name given to a species of the Buprestidae family of beetles boasting resplendent metallic and even specular colours (Figure 2-1). The study of the elytron of this beetle revealed layers of darkly contrasted material embedded at regular intervals of 60 nm in the otherwise pure chitin epicuticle. The increased density of these layers is attributed to melanin pigment deposits which are now known as the most commonly encountered

morphology utilised in nature to produce a periodicity in the RI. The simple multilayer structures observed in these beetles provides an efficient route towards developing artificial intense narrowband angle-dependent colour.

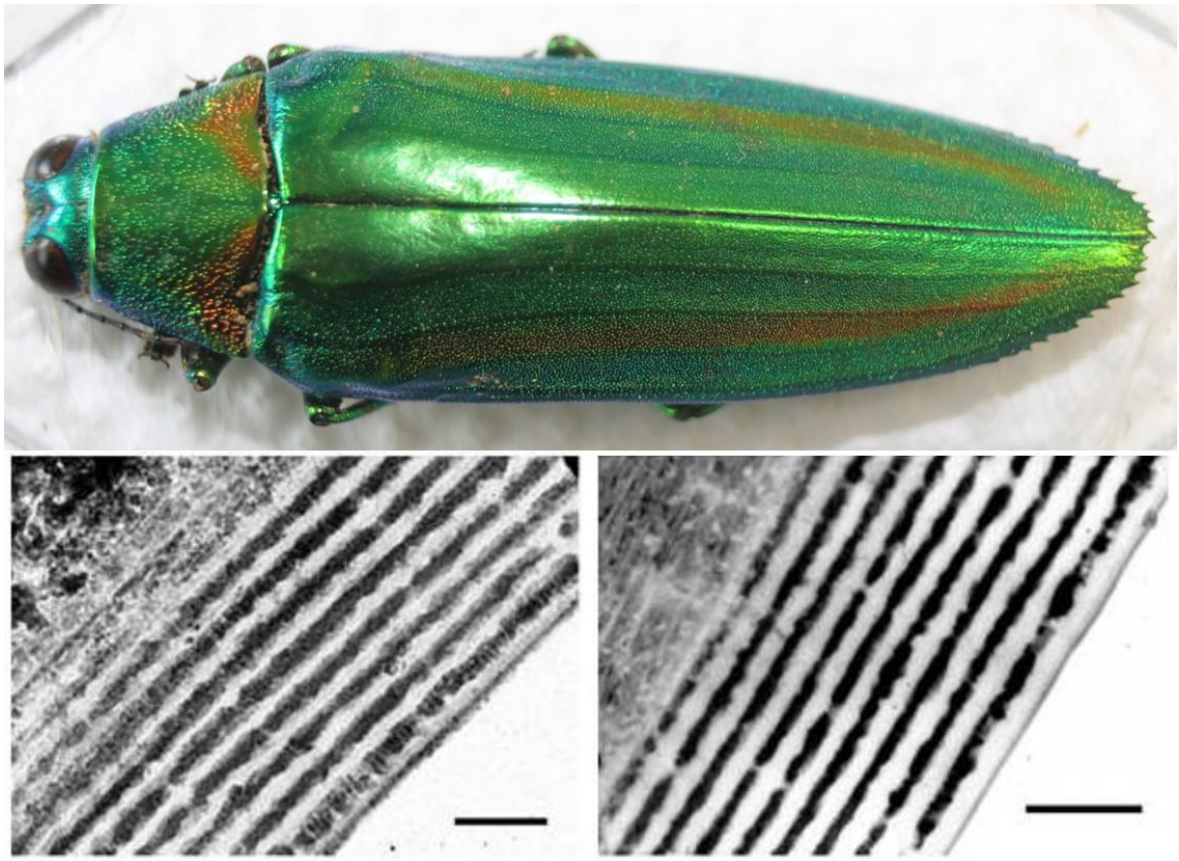

Figure 2-1 Top: Photograph of the iridescent buprestid species *Chrysochroa raja*. Bottom: Typical TEM images showing cross sectional views of the epicuticular multilayer structure for the green region (left) and orange region (right). TEM images courtesy of P. Vukusic[68]. TEM scale is 500 nm.

The 2-dimensional photonic crystal is less common in nature and typically consists of layers of rods stacked against one another, with several different packing geometries identified. Male peacocks conduct some of the most captivating visual displays witnessed

across the animal kingdom. The brilliant iridescent blue and green colours reflected from the feathers of these birds is generated by the ultrastructure of the feather barbules. For the genera *Pavo* and *Afropavo* species each feather barbule is a series of conjoined 'saddle-shaped' segments containing a 2D quasi-square lattice of melanin rodlets inter-bonded by keratin with an air vacuole at the centre of each square within the lattice (Figure 2-2). Yoshioka and Kinoshita[69] investigated these structures and using electron microscopy they observed melanin rods with lengths between 0.5 μm and 2 μm and diameters of 130 arrayed periodically across 8-12 layers. Yellow feather barbules possess 3-6 layers of the same arrangement but with particle diameters of 140 nm.

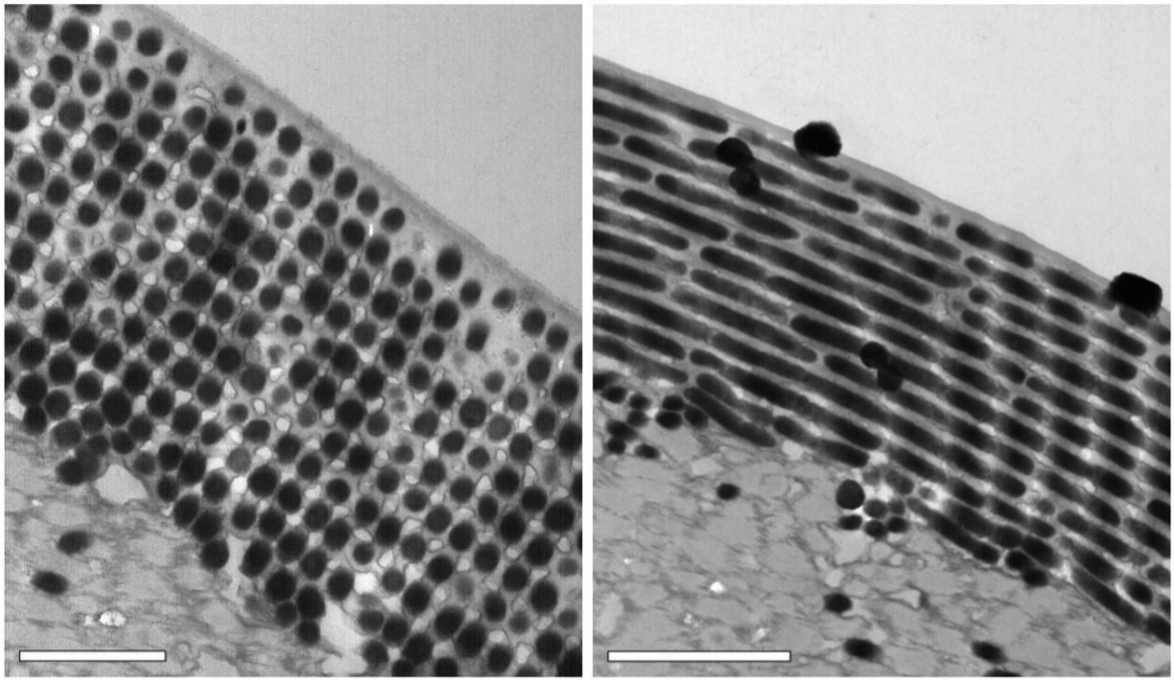

Figure 2-2 Images of (a) transverse and (b) longitudinal TEM cross-sections of a blue Peacock feather, with respect to the barbule axis. (Images courtesy of P. Vukusic). Scales bars: (a) 500 nm; (b) 1 μm.

When analysing the optical properties of such structures it is important to consider the directional dependence of the light reflected by the barbules. This is due to the 'saddle' shape which broadens the reflection over a large angular range[69]. Black-billed magpies have evolved a hexagonal lattice with air channels suspended in the keratin cortex of the barbules. This system exhibits complex optical properties as variation in colour cannot be straight forwardly reduced[70].

Biological structures with 3D ordered systems have been found to exist in greater abundance than 2D configurations. They are especially prevalent in the order Coleoptera where there appears to have been an evolutionary bias towards 3D photonic crystals. The scales of weevils (Figure 2-3top) have been of interest due to their striking colour palette which manifests through a wealth of elytral patterns. These are generated by a mosaic of differently coloured domains, each of which consist of a highly crystalline ultrastructure. SEM images of two of these types of scale are presented in Figure 2-3(a-d) where the photonic crystal takes on an FCC polycrystal structure exhibiting optical periodicity in three-dimensions. individual domains in the yellow scale (Figure 2-3a and c) are identified to be oriented differently. An array of these randomly oriented domains simultaneously exhibit both short range order and long-range disorder[71–75]. The blue scales (Figure 2-3b and d) show a quasi-ordered structure that is consistent across the scale. Such domaining is not exclusive to beetles, but has been described for crystalline structures found in the scales of several butterflies[10,72,76–78].

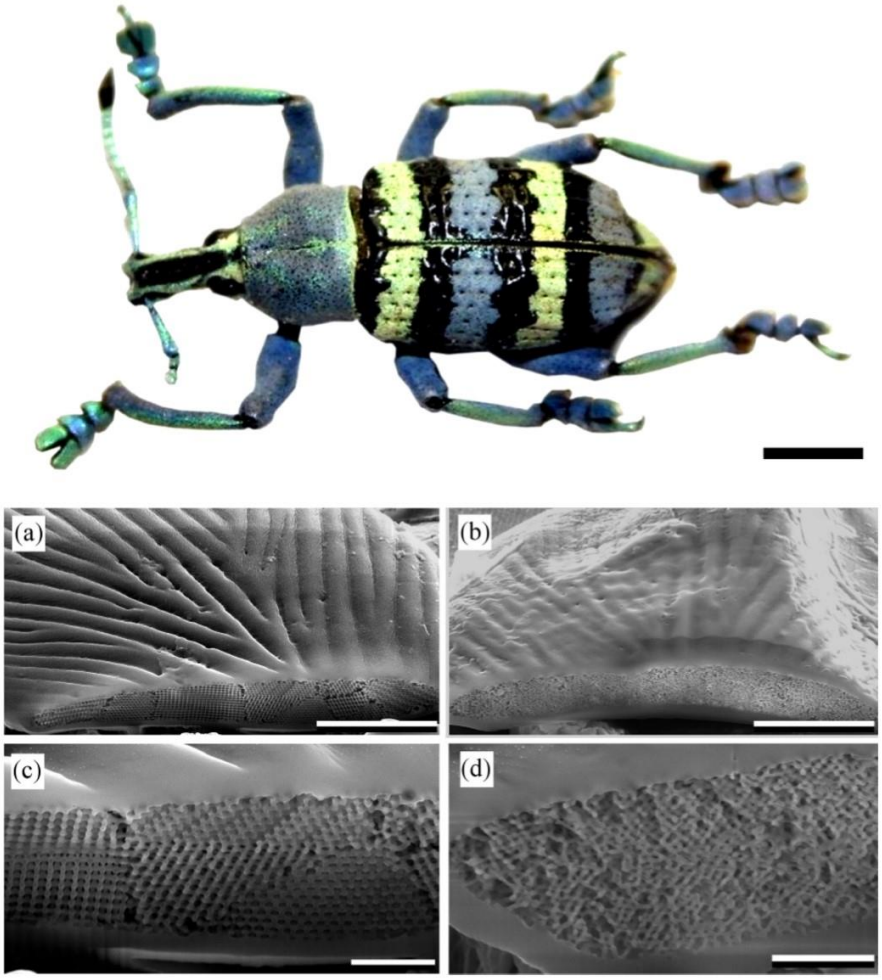

Figure 2-3 Top: Photograph of the weevil Eupholus magnificus. Bottom: SEM images of (a) and (c) fractured yellow scales showing a highly periodic 3D photonic structure; (b) and (d) blue scales, showing contrasting quasi-ordered structure. Images reproduced from Pouya et al.[73]. Scale bars: Top: 4 mm; Bottom: (a) and (b) 10 µm; (c) and (d) 2 µm.

Prum *et al*. have characterised many natural gyroid structures found in butterfly wings[79] and penguin feathers[56] for example and used analysis of such structures to predict colour appearance of 3D amorphous biophotonic structures[80].

2.1.3 Broadband reflectors

The optical behaviour of 1D multilayer morphologies where the periodicity is assumed to be fixed across the crystal structure express coloured appearances for a narrow range of wavelengths. Colour appearances expressing a broad range of wavelengths also exist in nature. They are known as broadband or metallic reflectors and have crystal ultrastructures with variable periodicity. Three sub classifications of multilayer structure in biological reflectors have been identified as: (i) 'chirped stacks, whereby the reflector exhibits a systematic variation in periodicity (Figure 2-4a); (ii) 'multiple filter' stacks, whereby two or more fixed-periodicity interference filters are arranged in sequence (Figure 2-4b), and (iii) chaotic or random stacks where disordered arrangements of layer thicknesses are featured (Figure 2-4c).

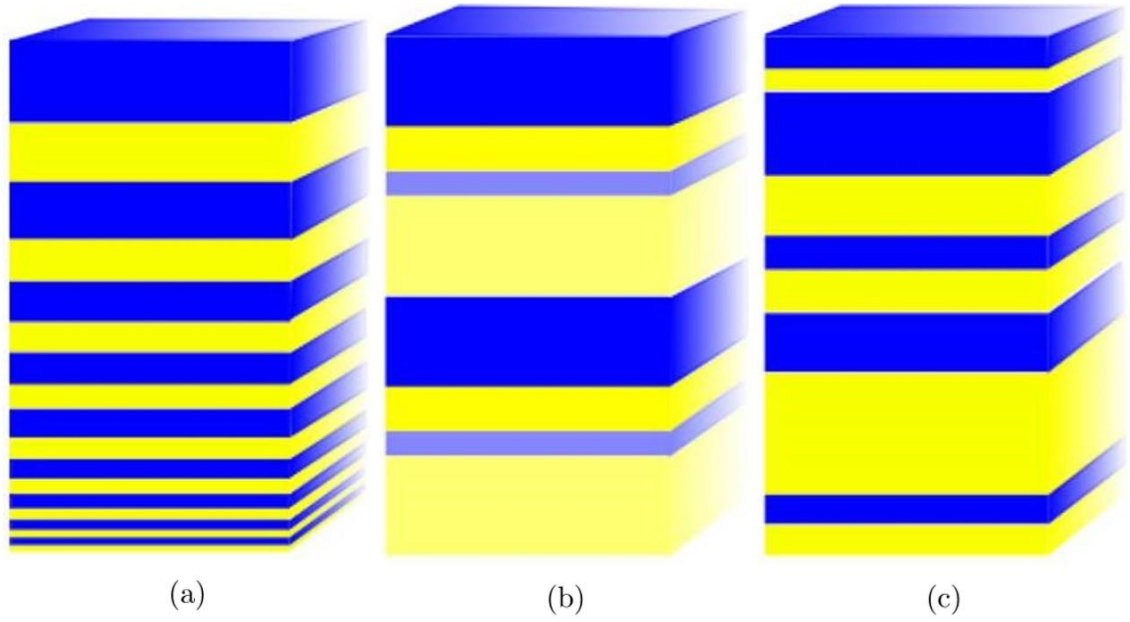

Figure 2-4 The sub classifications of multilayer structure: (a) The 'chirped stack'; (b) The 'multiple-filter stack'; (c) The 'chaotic' or 'random' stack. Diagram courtesy of C. Pouya.

These structural configurations are responsible for broadband reflection in certain beetle species and give rise to specular gold colour appearances[13]. Some insects can alter the colour appearance by expelling/filling cavities with liquid which changes the refractive index and hence light interference. Control of colour appearance gives animals a distinct survival advantage, allowing for adaptation in a changing environment and the ability to evade and/or warn predators.

2.1.4 Synthetic analogues

Synthetic analogues that allow the same degree of control over colour appearance are useful across a range of industries and a variety of methods have been used in the fabrication of structurally coloured thin films. Kolle *et al*. designed elegant multifolding elastically-deformable Bragg reflecting membranes and fibres that are reversibly tunable across the full visible spectrum[81,82]. They used methods to apply alternating layers of refractive index contrasting rubbers stretched over a pinhole where pressure could be applied to achieve concave shaped deformations. One of the problems with using rubber in applications where light induces temperature variation is the control of failure due to creep. They also used a spin coating method to produce a multilayer which was then rolled into a fibre. Rapid sol-gel chemistry was used by Bartl *et al*. to produce Bragg reflectors on substrates with varying geometries[29]. The limitations of such a method are the need to heat at high temperatures (500˚C). Significant savings can be made where high heat processes can be avoided. The Layer by layer technique is a more cost-efficient method and is popular due to the scale up possibilities and low-cost options; these will be discussed further in Chapter 4.

Other approaches include the manipulation of polymeric compounds to form crystalline structures with photonic bandgaps. Block copolymers have been utilised to great effect. Combining well defined polymeric material via a supramolecular assembly process allows control of structure formation on small length scales (5-100 nm). This opens the possibility of mesoporous structures and metamaterials that are active at visible wavelengths. Block copolymer structures can be fabricated from a range of processing conditions that are compatible with solution processing techniques such as layer by layer assembly. Block copolymer assembly generates highly ordered nanostructures in the condensed matter state and yield a combination of uniform patterns with tunable symmetries. Resulting assemblies may be used directly or used as templates to produce complimenting inorganic nanostructures. An example of templating was carried out by Thomas *et al.* who fabricated nanoporous polymers with gyroid nanochannels from the self-assembly of degradable block copolymer, polystyrene-b-poly(L-lactide) (PS-PLLA)[83]. The process is illustrated in Figure 2-5 and is followed by the hydrolysis of PLLA blocks which then underwent a sol-gel process to replace the PLLA with SiO_2. The PS was removed leaving a SiO_2 gyroid structure.

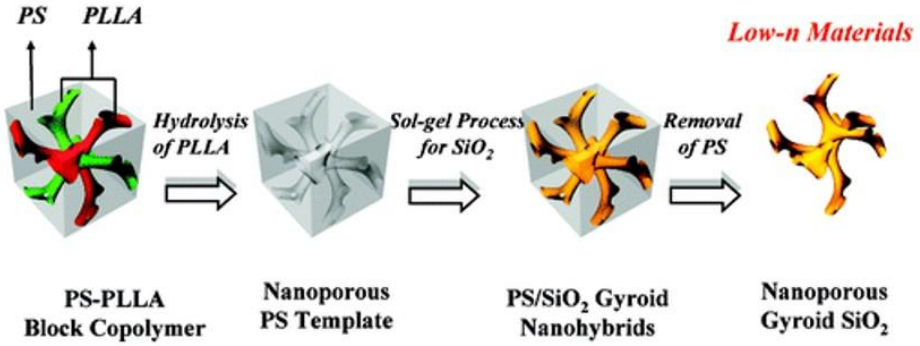

Figure 2-5 Fabrication process of photonic gyroid structure using block copolymer template. Reproduced from Thomas *et al.*, 2010.

The versatility, range of production routes and low cost of block copolymer assembly makes it an attractive platform to control and modulate the interaction of visible light with matter on the nanoscale. They have already been applied to 1D photonic crystals[84–87], Bragg reflectors and antireflective coatings[83,88–90] and offer a promising future for the development of light interference nanostructures.

This thesis aims to exhibit control over colour appearance of a fabricated thin film structure like those discussed above. The objective is to do so using the most abundant and sustainable material on the planet. Cellulose is not suitable for block copolymer assembly but is suitable for layer by layer assembly, the benefits of which are discussed later in Chapter 4. One-dimensional multilayer structures lend themselves more to scalable operations and will be the starting point. The following sections will present the underlying theory of the interference of physical structures with visible light starting with thin films and then expanding to multilayer and chiral structures.

2.2 Thin Film Interference

Often the dynamic interference of visible light in thin transparent materials like soap bubbles and oil on water produce beautiful visual effects. This iridescence is associated with the interference between light and either single or multiple thin surface layers. From these thin films narrow band wavelengths of visible light are coherently reflected leading to a unique display of colour observable to the naked eye. Varying conditions in any given situation determine the observed interference pattern created, which is why the colours

observed in soap bubbles can change. For example, a film of oil on water is bound by parallel planes as illustrated in Figure 2-6.

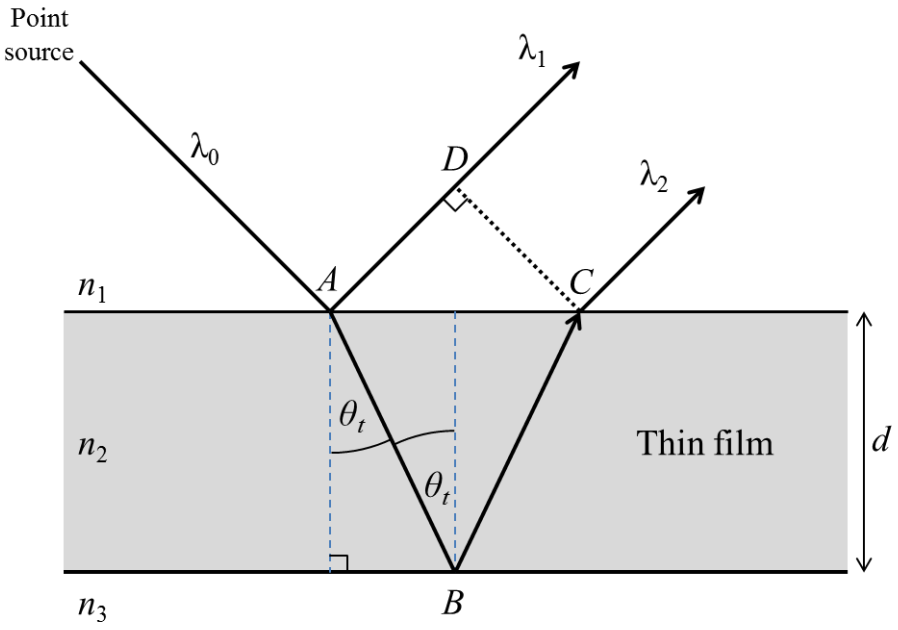

Figure 2-6 Schematic diagram showing the reflection of an incident wave (λ_0) from a film of thickness *d* and refractive index n_2. Reflected waves λ_1 and λ_2 emerge either constructively or destructively depending on the phase difference induced by the thickness of the film.

The setup considers the use of a monochromatic light source and only considers the first two reflected waves λ_1 and λ_2 as reflected from the n_1-n_2 and n_2-n_3 interfaces, where $n_{1\text{-}3}$ denote the related refractive indices (RI). The path lengths that each wave follows is different but as λ_1 and λ_2 emerge, they do so in parallel and can be brought together at a point on a focal plane of an objective lens such as the retina of the eye. The path lengths of λ_1 and λ_2 are $\left(\overrightarrow{AB} + \overrightarrow{BC}\right)$ and $\left(\overrightarrow{AD}\right)$ respectively. The equation for calculating the optical path difference (Λ) for the reflected waves is[91]

$$\Lambda = 2n_2 d\cos\theta_t. \quad (1)$$

Where d is the film thickness and θ_t is the incident angle of the transmitted wave. Now we consider the associated phase difference of the emerging and recombining waves. The phase difference is the product of the free-space propagation number k_0 (where $k_0 = 2\pi/\lambda$) and the optical path difference (Λ). Factoring the relative phase shift of π radians (φ) experienced by the reflected beams we then have

$$\delta = k_0\Lambda \pm \phi \quad (2)$$

where ϕ represents the additional relative phase shift of $\pm\pi$. Equation 2 will now be assessed to establish whether the waves emerge constructively or destructively. Constructive interference will occur when δ is equal to 2π or integer multiples of this, hence

$$m\lambda \pm \phi = 2n_2 d\cos\theta_t, \quad (3)$$

where m is an integer. The waves will emerge destructively when out of phase by a factor of π equal to δ, hence

$$\left(m + \frac{1}{2}\right)\lambda \pm \phi = 2n_2 d\cos\theta_t. \quad (4)$$

Having expressions for the reflection of a wave from two interfaces and the either constructive or destructive recombining of these waves, we now move on to consider additional reflections that occur within the thin film. Figure 2-7 illustrates the continuous

reflection (*r*) in and transmission (*t*) through the film of an incident wave. Emerging waves may all contribute to the resulting reflection intensity.

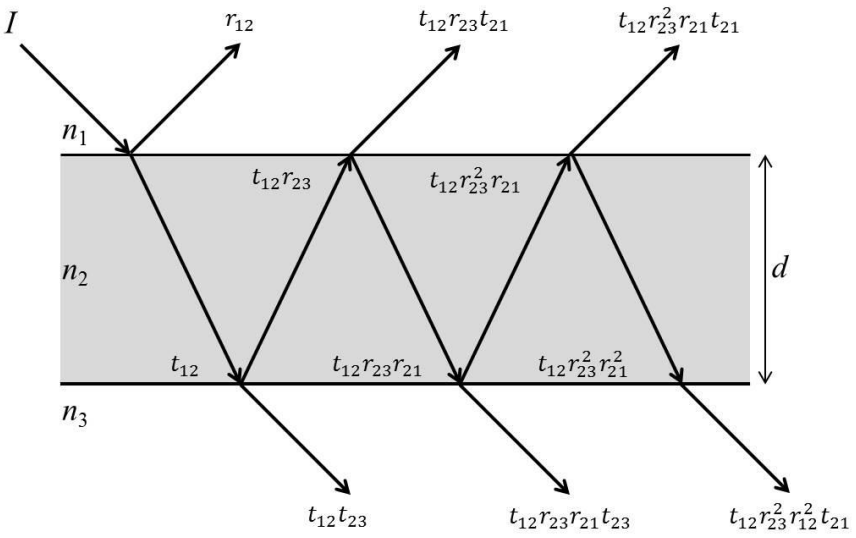

Figure 2-7 Schematic diagram showing the reflected and transmitted waves in a thin film with a RI of n_2 an incident medium RI of n_1 and exit medium RI of n_3.

From the behaviour highlighted in Figure 2-7 it is understood that there are an infinite number of reflections to consider. The expressions for calculating reflection can be reduced and subsequently, Stoke's relations (which state that $r_{ab} = -r_{ba}$ and $r_{ab}^2 + t_{ab}t_{ba} = 1$) can be applied to give an expression for reflection amplitude and corresponding reflection intensity from the film as follows

$$r = \frac{r_{12} + r_{23}e^{-i(2\delta)}}{1 + r_{23}r_{12}e^{-i(2\delta)}}, \tag{5}$$

$$R = |r|^2 = \frac{r_{12}^2 + r_{23}^2 + 2r_{12}r_{23}cos(2\delta)}{1 + r_{23}^2r_{12}^2 + 2r_{12}r_{23}cos(2\delta)}. \tag{6}$$

These are Fresnel's equations. Another method for calculating reflectance is the characteristic matrix of the investigated thin film[91]. This method can later be expanded to accommodate multilayered systems and forms the basis of the mathematical modelling used in this work. The characteristic matrix of a thin film considers the electric field (***E***) and the magnetic field (***H)*** properties at the edge of the interface boundaries. The interfacial boundaries (denoted a and b) are split into tangential components of the ***E*** and ***H*** fields to give forward and backward propagating components which are linked by the tilted optical admittance (η) to give

$$\begin{bmatrix} B \\ C \end{bmatrix} = \begin{bmatrix} E_a/E_b \\ H_a/H_b \end{bmatrix} = \begin{bmatrix} cos\delta & (i\ sin\delta)/\eta_2 \\ \eta_2(i\ sin\delta) & cos\delta \end{bmatrix} \begin{bmatrix} 1 \\ \eta_3 \end{bmatrix} \tag{7}$$

where $\begin{bmatrix} B \\ C \end{bmatrix}$ is the characteristic matrix of the thin film and E_a, E_b, H_a and H_b are the amplitudes of $\vec{\boldsymbol{E}}$ and $\vec{\boldsymbol{H}}$ fields in materials a and b respectively. The optical admittance (η_s) of the system is defined as:

$$\eta_s = \frac{H_a}{E_a} = \frac{C}{B} = \frac{\eta_3 cos\delta + \eta_2(i\ sin\delta)}{cos\delta + (i\ sin\delta)\eta_3/\eta_2}. \tag{8}$$

The optical admittance relates to the incident medium in a relationship that defines the reflectance from the characteristic matrix as follows[92]:

$$r = \frac{\eta_1 - \eta_s}{\eta_1 - \eta_s} \tag{9}$$

and

$$R = \left(\frac{\eta_1 - \eta_s}{\eta_1 + \eta_s}\right)\left(\frac{\eta_1 - \eta_s}{\eta_1 + \eta_s}\right)^*. \tag{10}$$

2.3 Multilayer Interference

Here we consider periodic multilayered systems where thicknesses and RIs of layers repeat at regular intervals (Figure 2-8). The periodic structure consisting of layers with two different RIs.

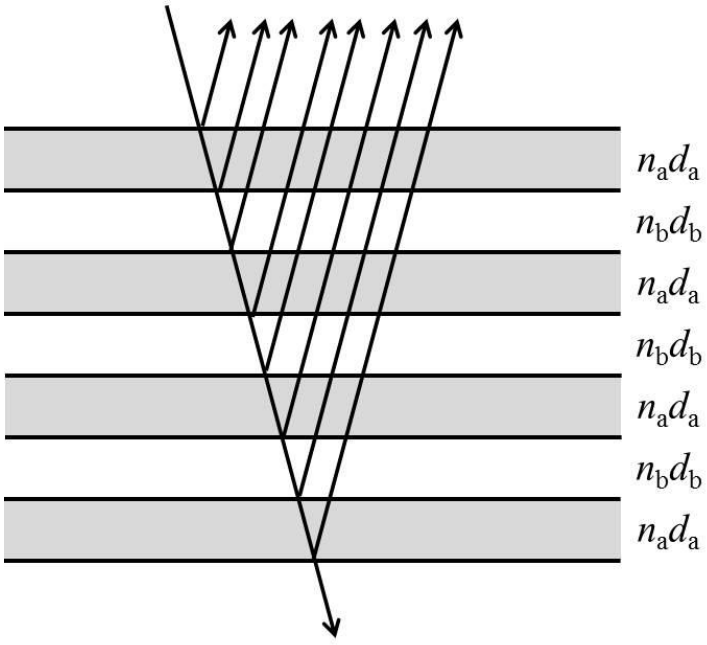

Figure 2-8 Schematic of an 'ideal' multilayer in which light reflected from every interface interferes constructively. This occurs when $n_a d_a = n_b d_b = \lambda/4$.

To calculate reflection from a multi-layered thin film we use the characteristic matrix of a 1-dimensional thin film, as described above, and adapt it to fit a system with *q* layers. Each

layer will require its own matrix and in the system an exit medium *m*. The following expression describes such a multilayer stack accounting for *q* layers;

$$\begin{bmatrix} B \\ C \end{bmatrix} = \prod_{j=1}^{q} \left\{ \begin{bmatrix} cos\delta_2 & (i\ sin\delta_j)/\eta_j \\ \eta_{j+1}(i\ sin\delta_j) & cos\delta_j \end{bmatrix} \right\} \begin{bmatrix} 1 \\ \eta_m \end{bmatrix}. \tag{11}$$

.

This method is known as the Transfer Matrix Method. An expression for the reflected intensity is used to extract the optical properties of the multilayer stack and is given by

$$R = \left(\frac{\eta_1 B - C}{\eta_1 B + C}\right)\left(\frac{\eta_1 B - C}{\eta_1 B + C}\right)^{*}. \tag{12}$$

For a full derivation for the above expressions please refer to Thin Film Optical Filters by H. A. Macleod[92].

2.3.1 Factors affecting reflectance from Multilayer systems

Biological and natural multilayer systems can produce a diverse array of vivid colourful effects. The unique optical displays from such systems are determined by the interplay between contributing variables associated with the structure and its constituent materials. The contributing variables include the number of layers in the system, the angle-dependence of reflection from the system and the disparity between the refractive indices of the n_a and n_b layers.

2.3.2 Effect of the number of layers

The difference in layer number of a given multilayer system is only significant where relatively few layer numbers are concerned. A return in reflection diminishes once a

critical number of layers is reached where subsequent changes in reflectance become negligible. This effect is demonstrated in Figure 2-9(a) where reflectance from a theoretical ideal multilayer with a peak reflectance at 500 nm is shown for 3, 9 and 27 layers. Reflectance from the 3-layer system exhibits broad band behaviour and would appear relatively dull to the eye.

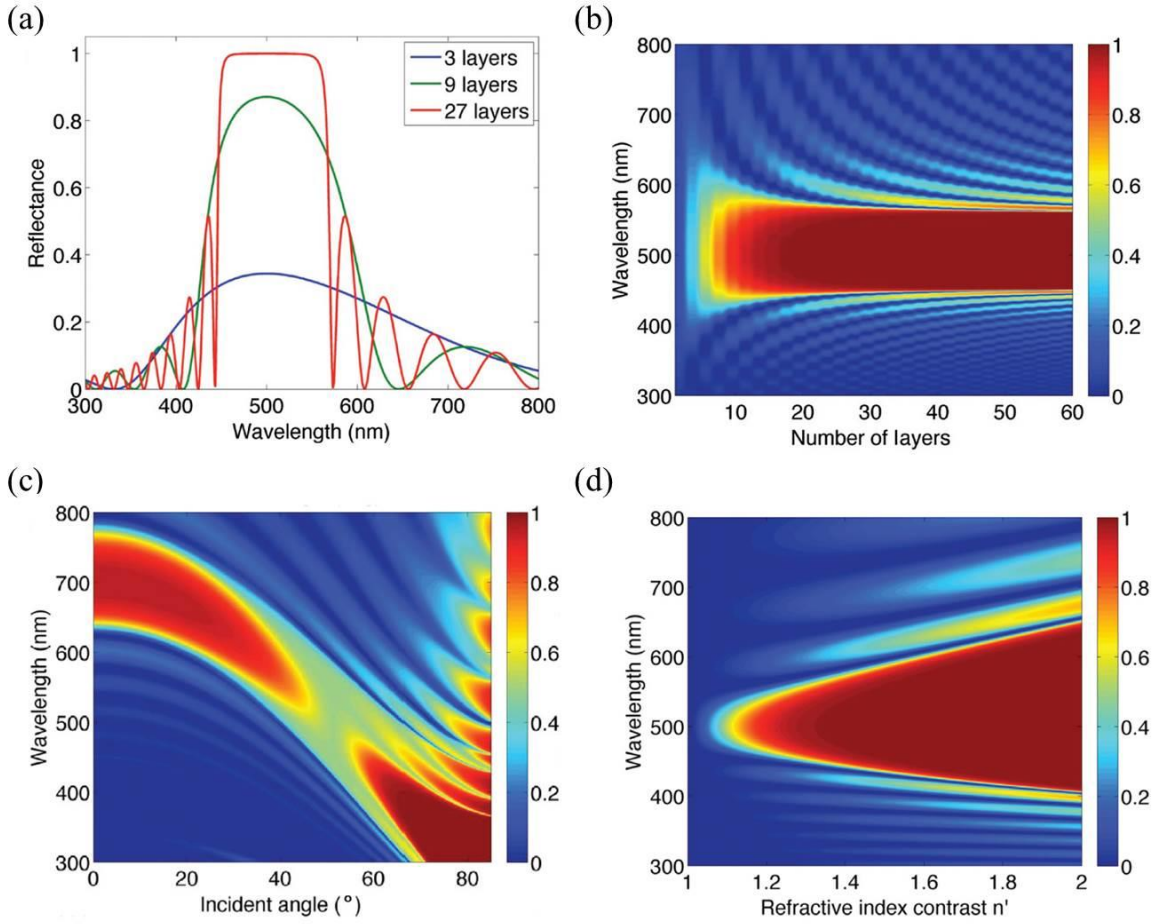

Figure 2-9 Data demonstrating the effects of key variables on peak reflectance in multilayer systems reproduced from Starkey *et al.*[93]. (a) Normal incidence reflectance of an ideal multilayer for 3, 9 and 27 layers. (b) A reflectance map showing the theoretical variation of normal incidence reflectance with increasing layer number, the colour-scale represents reflected intensity. Reflectance was calculated for a multilayer with λ_{peak} =500 nm. (c) A reflectance map showing reflection intensity as a function of incidence angle from an ideal multilayer with λ_{peak} =700 nm. (d) Reflectance map showing reflection intensity as a function of refractive index contrast

Reflectance from 9 layers exhibits more of the characteristic spectral features typically associated with multilayer reflectors. These include a maximum narrow band in reflectance at the peak wavelength and a series of maxima and minima side bands. The difference in peak reflectance between 3 and 9 layers is far greater than between 9 and 27 layers. The peak reflectance for an ideal multilayer at normal incidence comprising alternating high RI (n_a) and low RI (n_b) layers can be calculated using iterative methods[94] where

$$R = \frac{\left(\frac{n_a}{n_b}\right)^{2s} n_a^2 - n_{inc}n_{out}}{\left(\frac{n_a}{n_b}\right)^{2s} n_a^2 + n_{inc}n_{out}} \tag{13}$$

and s denotes the number of high and low RI pairs in the system of 2s+1 layers. The RI of the incident and exit media is denoted by n_{inc} (RI of the incident media) and n_{out} (RI of the exit media), respectively. As the number of layers increases equation 13 reduces to

$$R \cong 1 - \left(\frac{4n_{inc}n_{out}}{n_a^2}\right)\left(\frac{n_b}{n_a}\right)^{2s} \tag{14}$$

And the peak reflectance rapidly approaches unity. The region of 100% reflectance is known as the photonic band gap (PBG). Figure 2-9(b) shows a reflectance map of reflectance intensity for the same system but with many more layer numbers. In this map it is clear to see the peak reflectance increasing until it approaches that of a multilayer of infinite layers. The spectral width of a multilayer's PGB is governed by the constituent RIs of the layers[95].

2.2.3 The angle dependence of reflection

The change in hue with viewing angle is a phenomenon known as iridescence and is notably produced by periodic structures. By varying the the incident angle, as illustrated in Figure 2-6 and as represented by θ_t in Equations 1 and 3, the optical path length through the periodic structure changes. An increased angle of incidence results in shorter wavelengths of light emerging constructively from the structure. This behaviour is presented graphically in Figure 2-9(c) where the reflectance maximum shifts towards shorter wavelengths (blue-shifts) with increasing angle of incidence. A strong blue-shift is shown in the map where peak reflectance at ~700 nm shifts to ~300 nm as incidence angle increases. Reflectance intensity however, is not constant and decreases to a minimum at the Brewster angle[96]. Beyond this point reflectance intensity rapidly increases.

2.2.4 The effect of refractive index contrast

The disparity between the refractive indices of the n_a and n_b layers has a significant effect on reflectance. Figure 2-9(d) shows the dependence of normal incidence unpolarised reflection as a function of increasing RI contrast. As the contrast in RI increases the

intensity and band width of reflection also increases. Sheppard demonstrated this in 1995 with the equation[97]

$$r = \frac{n_{\text{air}} n_{\text{H}}^{2m} - n_{\text{S}} n_{\text{L}}^{2m}}{n_{\text{air}} n_{\text{H}}^{2m} + n_3 n_{\text{L}}^{2m}} \tag{15}$$

where H represents the high RI, L the low RI, S is the substrate and m is the number of double layers. It can be seen from this equation that reflectance (r) increases as the difference between n_{H} and n_{L} increases. The extent to which biological multilayer systems can produce a complete PBG by RI disparity is limited by the materials available[95]. An advantage to the design of fabricated multilayer systems is the range of high-index materials available which may include metals and semiconductors.

2.4 Cholesteric phases and chiral reflection

The CNCs considered in this thesis undergo self-assembly to form a cholesteric liquid crystalline phase which may be preserved in a dry film following the evaporation of the solvent. To understand liquid crystalline phases, it is first useful to define the basic states of matter: gases, liquids and solids. In crystalline, amorphous and polymeric solids, atoms occupy fixed positions and occupy a definite volume, the bulk of which can withstand a shear stress. Movement of individual atoms is possible and only achieved with great difficulty due to reduced thermal motion. Gaseous states, in contrast, are characterised by the random, translational motion of molecules that experience little molecular interaction

and occupy no definite volume. Liquids are not as straight forward and possess a combination of some of the characteristics found in both solids and gases. The molecules in a liquid are free to move randomly and cannot withstand shear stress. Instead they only experience hydrostatic pressure or tension and is why the pressure in a liquid is the same in all directions. So, like a gas, liquids are fluid and part from gaseous behaviour where volume is concerned, because like a solid the molecules in a liquid occupy a definite volume. Another significant difference between a liquid and a gas is that liquids have structure and produce coherent diffraction patterns [98]. A study of this structure lead Bernal *et al.*[99] to develop the random packing model that helped them define liquids as 'homogeneous, coherent, and essentially irregular assemblages of molecules containing no crystalline regions'. A liquid crystal state is intermediate between the irregular assemblages of molecules in a liquid and a crystalline solid. Within liquid crystal states, molecules diffuse from one place to another while maintaining a degree of orientational order and sometimes a degree of positional order. The ordered molecules in a liquid crystal generally have one molecular axis that tends to point along a preferred direction. This means liquid crystal phases are typically formed by amphiphilic molecules and certain organic molecules which have a high degree of anisotropy such as rod or disc-like molecules. There are many types of liquid crystal, all with a common attribute of anisotropy. It is the interactions between anisotropic molecules that promote orientational and positional order in a fluid medium. Typically, the long axis of such molecules will align to express a preferential direction with a certain degree of deviation. The deviation of the long axis of any given molecule by θ from this preferred direction can be measured.

Soap and phospholipids are commonly known rod-shaped molecules capable of forming liquid crystalline phases that take on the form of micelles and vesicles. Such molecules are referred to as mesogenic and form in one of two systems: either a thermotropic system or a lyotropic system[100]. A thermotropic system is temperature dependent and the liquid crystalline phase will only occur within a certain temperature that ranges between the crystalline melting point and the isotropic liquid temperature transition. The lyotropic system is of most relevance to this study and is where crystalline phases are formed at lower temperatures by the addition of a low molecular weight solvent. Lyotropic solutions have been shown to form liquid crystalline phases independent of temperature where instead, the formation is driven by the concentration of a suspension. The self-assembly process occurs spontaneously above a critical concentration of the polymer in solution. The above systems involve rigid-rod polymers such as cellulose nanocrystals. Mesogenic phases in liquid crystalline polymers (LCPs) naturally form particular structures known as smectic, nematic and cholesteric phases (Figure 2-10). These three phases were identified by Friedel in 1922 and are now known as the Friedelian classes[100]. It can be seen in Figure 2-10(a) that the nematic liquid crystalline phase has long range orientational order but no short range positional order where the alignment of the crystals is imperfect but the centres of mass of the objects are distributed randomly.

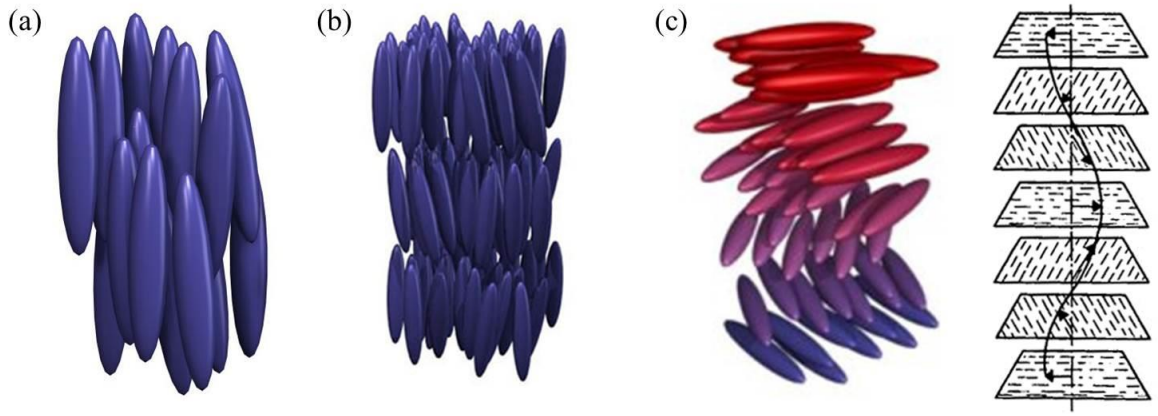

Figure 2-10 Representations of rod shaped nanocrystal arrangements in the three Friedelian classes of liquid crystals: (a) Nematic; (b) Smectic; (c) Cholesteric.

The smectic phase shown in Figure 2-10(b) adopts a more clearly defined layer structure and is a result of molecules that are naturally amphiphilic such as those found in detergents and soaps. The phospholipid bilayer of cell membranes is an example of a smectic order. Like the nematic phase, the alignment of a smectic phase is imperfect but has long range orientational order[100]. The cholesteric phase is similar to that of the nematic phase only it undergoes twisting about an axis perpendicular to the director (Figure 2-10c). The gradually twisting cholesteric has a progressively rotating direction of components made up of multi-laminate neighbouring planes[101]. The twist is a spontaneous arrangement and a result of an intrinsic chiral or asymmetric characteristic of the constituent molecules. The helix formed by the gradual rotation between planes of nematic molecules is temperature-dependent[100]. At high temperature the molecules have greater thermal energy and this generally results in a larger angle of rotation which creates a tighter pitch. Cholesteric structures occur naturally and have been observed in crab and insect integument[10,51,53]. The optical properties of such systems are well understood.

2.4.0 Pseudo Bragg Reflections

The arrangement of CNC layers described in Section 2.3.2 consists of optical elements piled so that principle axes of the successive elements are turned through a small angle α. This rotation presents periodic refractive index variations to a light beam with a given orientation and behaves like a multilayer reflector as described in Section 2.2. The light is then diffracted when the Bragg type condition:

$$\lambda = nPsin\theta_{\mathrm{B}} \tag{16}$$

is satisfied, where n is the mean refractive index and θ_{B} is the Bragg angle. Figure 2-11 highlights the Bragg parameters for reflection from a structure with a periodic variation in refractive index (n_1 and n_2).

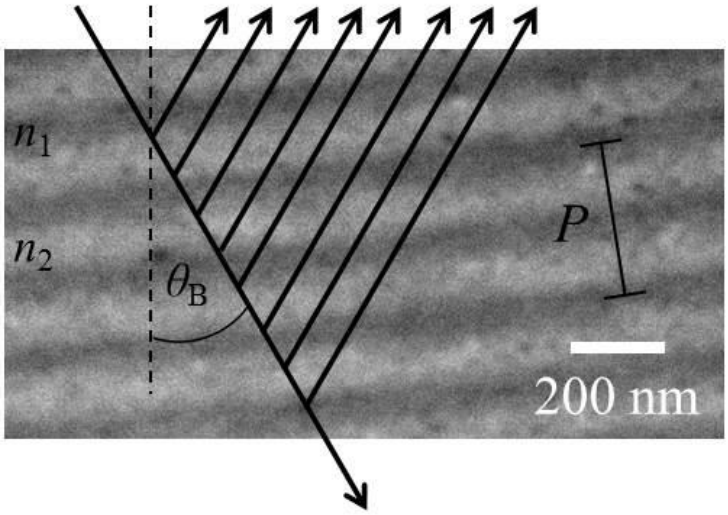

Figure 2-11 Typical transmission electron microscope image of a CNC thin film cross section with Bragg conditions overlaid on the image.

The periodicity in the structure gives rise to a photonic bandgap where, for a given incidence angle of white light, a narrow band of light is constructively reflected. Where

variation also exists in the orientation of regions of a sample then multiple wavelengths of incident light will be selectively reflected producing multifarious coloured effects.

2.4.1 Birefringence

The optical anisotropy of uniaxial crystals gives rise to a difference in the electric field of the components of reflected and transmitted polarised light. This is due to the relative permittivity of uniaxial crystals being different for electric fields in different directions. Each polarisation experiences a difference in the refractive index; one of high (n_{H}) and one of low (n_{L}) refractive index. This phenomenon, known as birefringence (B) is a measure of the difference between these two refractive indices which is responsible for the optical retardation of light passing through or reflected from the medium, $\mathrm{B} = |\, n_{\mathrm{H}} - n_{\mathrm{L}} \,|$. In a nematic liquid crystal this means that light polarised parallel to the director propagates according to one index of refraction, and light polarised perpendicular to the director has another index of refraction. The retardation of polarised light passing through anisotropic crystals with a given thickness (t) is: $\Gamma = \mathrm{B} \times t$. When observed between crossed polarisers birefringent effects give rise to interference colours which are indicative of how the optical axis of the uniaxial crystals is aligned with respect to the retardation wave plate. A typical colour interference pattern is shown in Figure 2-12 where the alignment of the optical axis of the uniaxial crystals with respect to the retardation wave plate determines the appearance of colour[102]. Crystals aligned with their optical axis parallel to the wave plate appear blue and those aligned at a 90° angle appear yellow. At a 45° angle to the wave plate the crystals appear “pinky-red”.

Polarised optical microscopy (POM) is a useful tool for quickly identifying the crystal alignment throughout a given sample. The image shown in Figure 2-12 shows a multiphase region of a thin film where the crystalline regions are 10-100 μm across and are distributed relatively evenly.

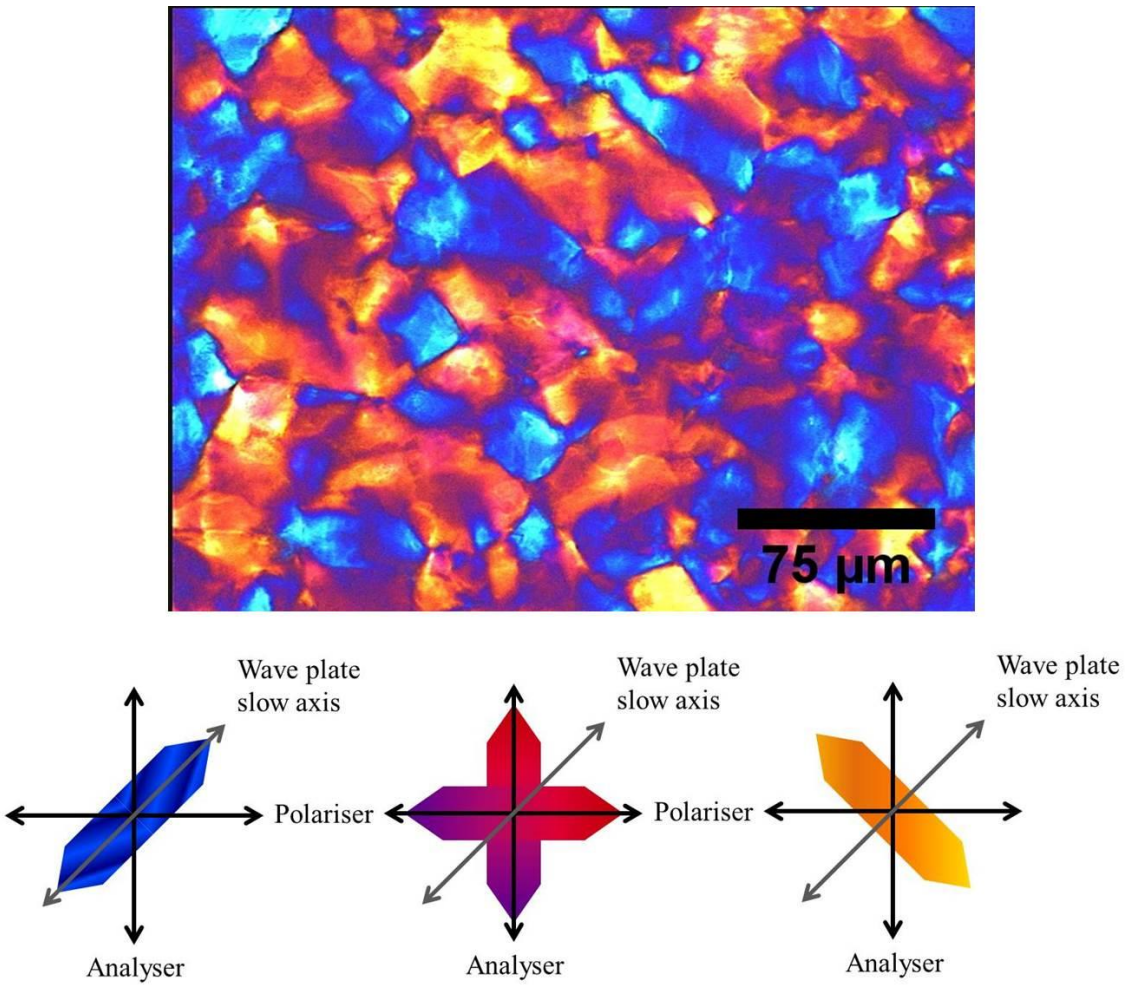

Figure 2-12 Typical polarised optical microscope (POM) image of a birefringent CNC thin film (top) and a schematic showing colour appearance generated by alignment of the birefringent uniaxial crystal optical axis with the optical axis of the retardation plate. Image is unpublished data.

2.4.2 Circular Dichroism

Circularly polarised light is generated by inducing a π/2 phase shift between the two orthogonal components of plane polarised light. The handedness of the circularly polarised (CP) light is either left (LCP) or right (RCP) and depends on which of the orthogonal planes of polarisation has undergone a phase shift. The chiral structures of cholesteric mesophases are optically active and selectively reflect like handedness or transmit opposite handedness as illustrated in Figure 2-13.

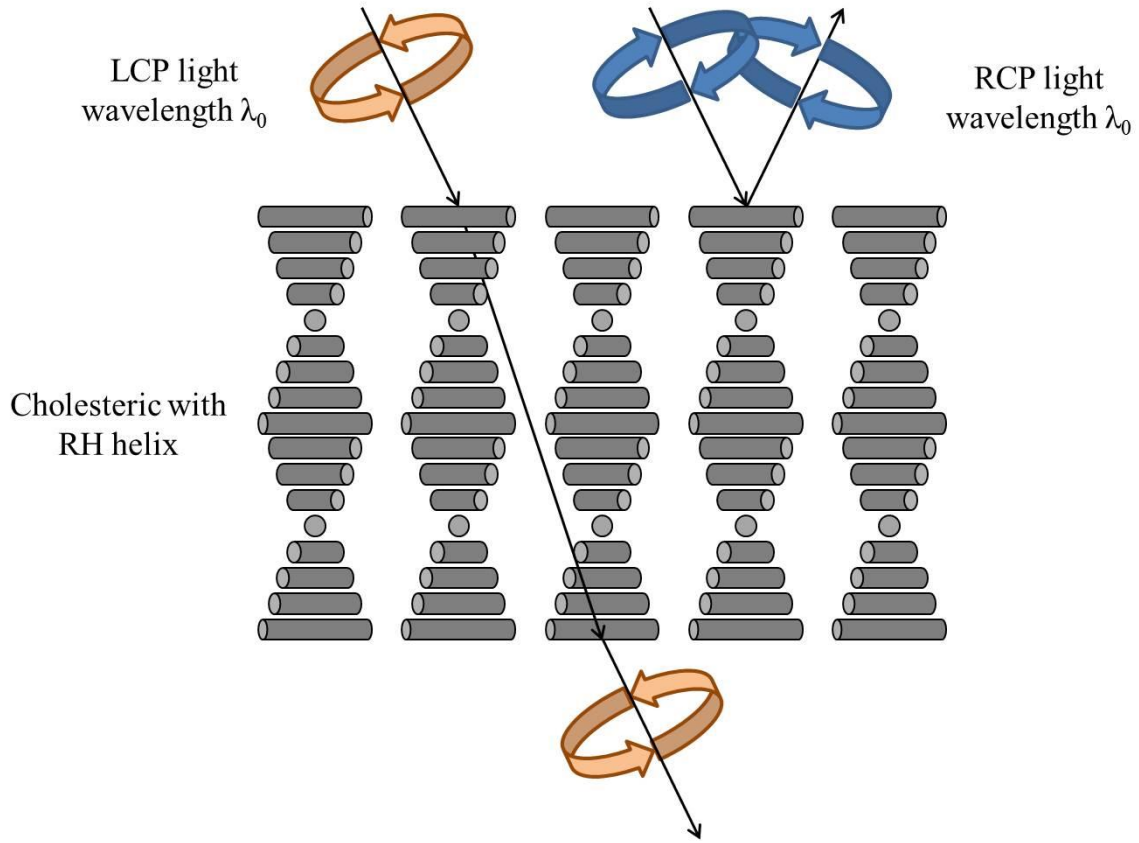

Figure 2-13 Specific cholesteric optical effect where selective transmission and reflection of LCP and RCP light occurs when $\lambda_0 = nP$.

The mathematics used to model the reflection from structures that induce elliptical changes to the polarisation of incident light will be presented here and is based on the work by R. C. Jones[103]. Jones calculus is used to model the reflection of incident light along the helical axis of a cholesteric structure within a thin film. Jones' method accounts for the optical rotation produced by many optical elements piled so that the principle axes of the successive elements is turned through a small angle α. Each optical element is an infinitesimally thin birefringent layer. The Jones vector

$$\mathbf{E} = \begin{bmatrix} E_x(t) \\ E_y(t) \end{bmatrix} \tag{17}$$

represents the electric state of a beam where $E_x(t)$ and $E_y(t)$ are the instantaneous scalar components of **E**. In order to preserve phase formation, φ_x and φ_y the appropriate phases are included and equation 18 becomes

$$\mathbf{E} = \begin{bmatrix} E_{0x}e^{i\varphi_x} \\ E_{0y}e^{i\varphi_y} \end{bmatrix}. \tag{18}$$

The perpendicular (s) and parallel (p) polarisations are given by

$$\mathbf{E}_\mathrm{s} = \begin{bmatrix} E_{0x}e^{i\varphi_x} \\ 0 \end{bmatrix} \text{ and } \mathbf{E}_\mathrm{p} = \begin{bmatrix} 0 \\ E_{0y}e^{i\varphi_y} \end{bmatrix}. \tag{19}$$

E is then equal to the sum of the two components in equation 20 and after factoring is given by

$$\mathbf{E} = E_{0x}e^{i\varphi_x}\begin{bmatrix} 1 \\ 1 \end{bmatrix} \tag{20}$$

where the amplitudes are equal and the phase difference is zero. To gain simpler expressions the irradiance can be normalised to unity. Dividing each vector in equation 20 by the same scalar quantity gives s and p states of

$$\mathbf{E}_{\mathrm{s}} = \begin{bmatrix} 1 \\ 0 \end{bmatrix} \quad \text{and} \quad \mathbf{E}_{\mathrm{p}} = \begin{bmatrix} 0 \\ 1 \end{bmatrix}. \tag{21}$$

The normalised Jones vectors for right and left circularly polarised light follow as

$$\mathbf{E}_{\mathrm{RCP}} = \frac{1}{\sqrt{2}} \begin{bmatrix} 1 \\ -i \end{bmatrix} \quad \text{and} \quad \mathbf{E}_{\mathrm{LCP}} = \frac{1}{\sqrt{2}} \begin{bmatrix} 1 \\ i \end{bmatrix} \tag{22}$$

Now that the polarisation states have representative vectors ($\mathbf{E}_i$), the changes induced by passing through a birefringent material can be considered. A monochromatic polarised incident wave, $\mathbf{E}_{\mathrm{in}}$, incident upon birefringent chiral layers will emerge altered possessing the new vector $\mathbf{E}_{\mathrm{out}}$. The alteration of the vector is explained mathematically using a 2x2 matrix (**J**) (the elements of which are complex), expressed as

$$\mathbf{E}_{\boldsymbol{out}} = \begin{bmatrix} a_{11} & a_{12} \\ a_{21} & a_{22} \end{bmatrix} \mathbf{E}_{in}. \tag{23}$$

where *a* represents the possible polarisation state induced by the medium on the incident light. This matrix calculus method determines the linear transformation of the Jones vector of a plane wave by reflection or transmission. As described above the incident wave will interact with piled optical elements which here will be represented by the matrices $\mathbf{J}_1$, $\mathbf{J}_2, \ldots, \mathbf{J}_{n-1}, \mathbf{J}_n$, then

$$\mathbf{E}_{out} = (\mathbf{J}_n \mathbf{J}_{n-1} \cdots \mathbf{J}_2 \mathbf{J}_1)\mathbf{E}_{in}. \quad (24)$$

The matrices need to be applied in the correct order, as they do not commute, so a particular coordination system is used to specify the orientations of the incident and emergent light beams relating to each Jones matrix. The Jones matrix for a RCP optical element is

$$\frac{1}{2}\begin{bmatrix} 1 & i \\ -i & 1 \end{bmatrix} \quad (25)$$

and for an LCP optical element

$$\frac{1}{2}\begin{bmatrix} 1 & -i \\ i & 1 \end{bmatrix}. \quad (26)$$

This method allows the calculation of resulting polarisation states of light waves emerging from a given optical system. This is achieved by taking the product of the Jones vector and the Jones matrix as described above.

2.4.3 Rotatory Power

The supramolecular organisation of the cholesteric mespohase gives rise to high values of rotatory power (Ω) which can be estimated from the de Vries formula[40]:

$$\Omega = \frac{\pi P}{4\lambda^2} \cdot \frac{\Delta n^2}{1 - (\lambda/\lambda_0)^2} \tag{27}$$

where P is thickness, λ is the incident wavelength, λ_0 is the mean wavelength of the reflection band and Δn the birefringence in a plane perpendicular to the optical path and to the helix axis. Plane polarised light transmitted through a typical optically active solution or crystal will undergo rotation of 1-2 radians per mm pathlength whereas plane polarised light transmitted through a cholesteric mesophase parallel to the helix axis can have its plane rotated by up to 100 radians per mm.

2.5 Colourimetry using CIE values

Quantitative links between visible wavelengths of light and the physiological perceived colours in human vision were defined in 1931 by the Commission Internationale de l'Eclairage (International Commission on Illumination; CIE). Electromagnetic radiation with wavelengths in the visible region of the spectrum is detected by two types of photoreceptor cell in the retina of the human eye called rods and cones. The cone cell photoreceptors differentiate wavelength and facilitate colour perception. They consist of three cone cell light detectors which are sensitive to either short wave lengths (S, 420-440 nm), to medium (M, 530-540 nm) and long wavelengths (L, 560-580 nm) of light[104]. The spectral sensitivity of these S, M and L cells is presented in Figure 2-14(a). The mathematical relationships developed to define colour spaces that are used to quantify human vision are based on colour matching functions (CMFs). These functions describe

the amounts of red, green and blue light which, when mixed, match a monochromatic light of wavelength λ of constant radiant power. The amounts may be negative (Figure 2-14b) and have been standardised by the CIE.

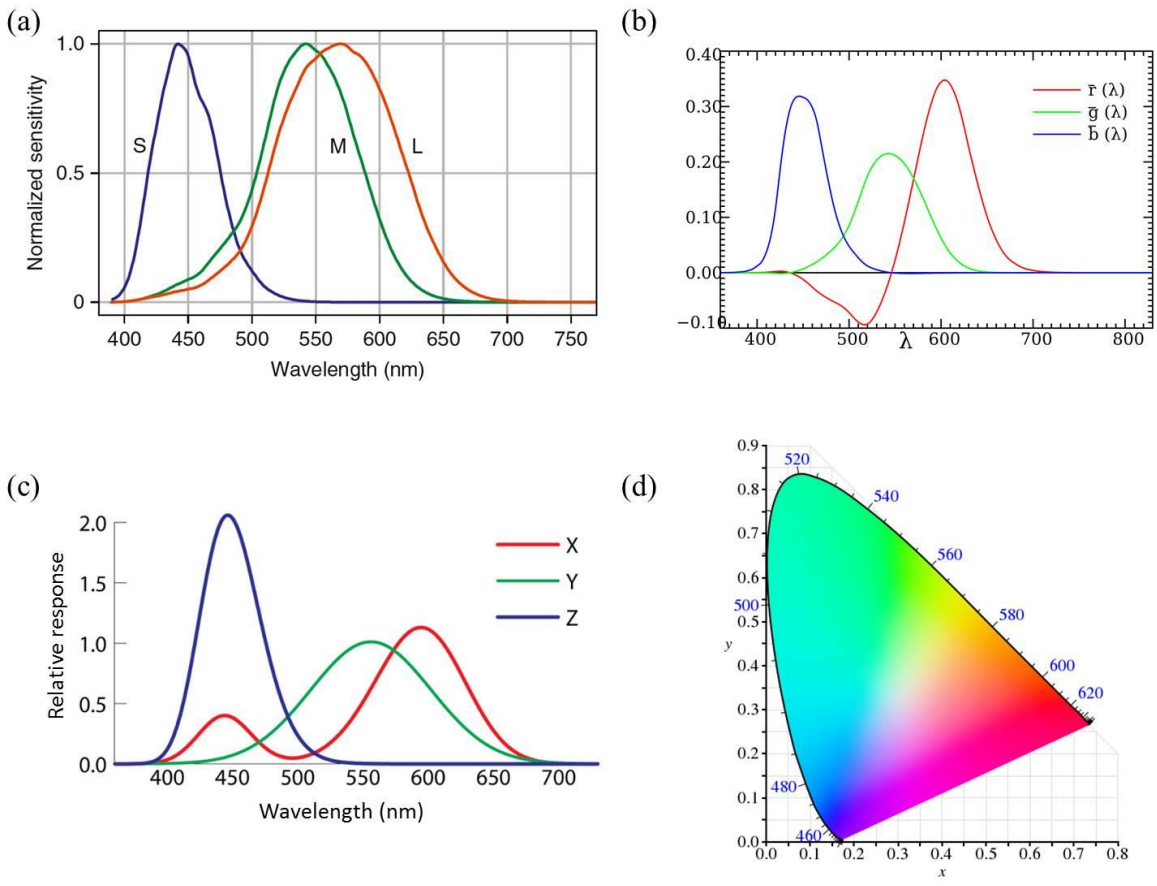

Figure 2-14 (a) Spectral sensitivity curves of the long, medium and short wavelength sensitive (L, M and S) cones. Reproduced from Foster (2010)[104]. (b) The CIE 1931 RGB colour matching functions. (c) X, Y and Z spectral sensitivity curves. Reproduced from Wyman et al. (2013)[105]. (d) The CIE 1931 colour space chromaticity diagram.

The sensitivities together represent an average human perception of colour and provide what is called a tristimulus specification of the objective colour of the visible spectrum.

The RGB colour space makes use of monochromatic primary colours of wavelengths 700 nm (red), 546.1 nm (green) and 435.8 nm (blue)[106]. They are defined by the CIE RGB colour matching functions[107] $\bar{r}(\lambda), \bar{g}(\lambda), \text{and } \bar{b}(\lambda)$ (which are the spectral response curves for the S, M and L cones) from which the RGB tristimulus values are obtained

$$R = \int_0^\infty S(\lambda)\bar{r}(\lambda)d\lambda, \tag{28}$$

$$G = \int_0^\infty S(\lambda)\bar{g}(\lambda)d\lambda, \tag{29}$$

$$B = \int_0^\infty S(\lambda)\bar{b}(\lambda)d\lambda, \tag{30}$$

where $S(\lambda)$ is the spectral power distribution of a given colour. These were later reformatted in to the mathematically equivalent CMFs $\bar{x}(\lambda), \bar{y}(\lambda)$ and $\bar{z}(\lambda)$ (Figure 2-14c). The tristimulus values X, Y and Z (Figure 2-14c) define the CIE colour space that encompasses the colour sensations experienced by the average human. These are used to define an object's perceived colour as follows

$$X = k\int_{380}^{780} \bar{x}(\lambda)s(\lambda)R(\lambda)\mathrm{d}\lambda \tag{31}$$

$$Y = k\int_{380}^{780} \bar{y}(\lambda)s(\lambda)R(\lambda)\mathrm{d}\lambda \tag{32}$$

$$Z = k\int_{380}^{780} \bar{z}(\lambda)s(\lambda)R(\lambda)\mathrm{d}\lambda \tag{33}$$

where k is a normalisation constant given by

$$k = 100/\int_{380}^{780} \bar{y}(\lambda)s(\lambda)\mathrm{d}\lambda \tag{34}$$

and where s is the spectral energy distribution of the illuminant and R is the measured reflectance of an object. When the tristimulus values are normalised against one another we have

$$x = \frac{X}{X+Y+Z}, \tag{35}$$

$$y = \frac{Y}{X+Y+Z}, \tag{36}$$

$$z = \frac{Z}{X+Y+Z}. \tag{37}$$

Only two of the above parameters are required to define any hue of colour since $x + y + z = 1$. The parameters conventionally used are x and y ($z = 1 - x - y$), also known as the chromaticity coordinates which are subsequently plotted on the CIE colour triangle (Figure 2-14d).

Chapter 3 Cellulose

3.1 Synthesis and structure

The presence of structural material in plants was first observed by Nägeli in the mid-1800s who observed brick-like structures surrounding plant cells. He concluded that plant cell membranes were composed of sub-microscopic crystalline particles that he called micelles[108]. These were confirmed in the early 1900s by Meyer and Mark. The micelles were discovered to be made of polymer chains known as cellulose, the molecular formula of which ($C_6H_{12}O_6$) had already been established by the French chemist Anselm Payen in 1838. The structure of the $C_6H_{12}O_6$ molecule is shown in Figure 3-1(a) and represents the long chain cellulose polymer. A single molecule, called glucose is the repeat unit and made up of a pyranose ring consisting of 5 carbon atoms and 1 oxygen atom. Attached to the carbon atoms are hydrogen atoms, hydroxyl groups and a hydroxymethyl group on the 5th carbon atom. The repeat units of the cellulose polymer are glucose monomers which form a 1, 4-β glucan chain with neighbouring monomers rotated by 180° with respect to each other (Figure 3-1a)[109]. Polymerisation of glucose monomers is catalysed in the plasma

membrane by cellulose synthase (CesA) proteins[110]. Each CesA unit (Figure 3-1b) produces one polymer chain and typically exist as a rosette subunit which has six-fold symmetry[110]. A rosette contains six rosette subunits which produce 36 chains simultaneously (Figure 3-1b). These chains spontaneously bundle together forming microfibrils (2-4 nm in diameter to several microns) in the cell wall and represent the micelles observed by Nägeli.

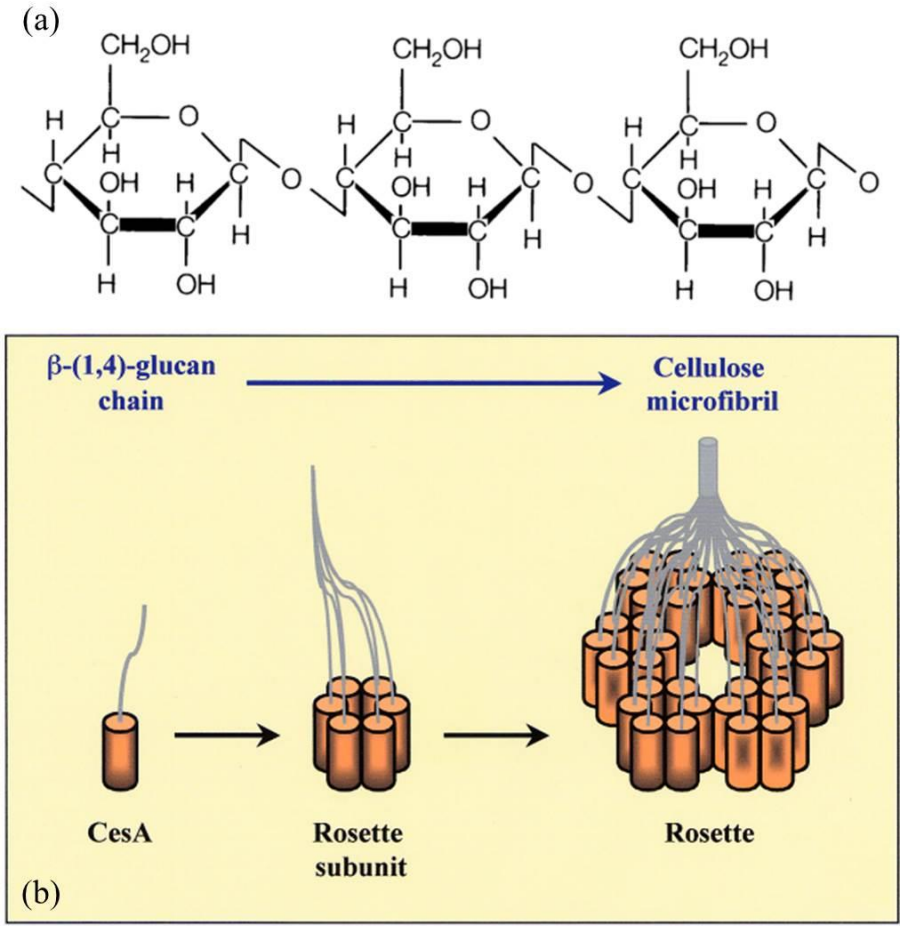

Figure 3-1 (a) Two repeat units of cellulose. (b) The CesA protein responsible for the synthesis of polymeric cellulose chains and the protein clusters responsible for the formation of cellulose microfibrils. Image published by Doblin *et al*. 2002[110].

The rotation of monomers produces a relatively flat polymer chain allowing adjacent chains to interact at proximity to each other. The polymer chains interact via hydrogen bonding, hydrophobic interactions between the flat pyranose rings and Van der Waals forces which all contribute to sustaining a highly crystalline structure[111]. Measurements of the size of these molecules or micelles was undertaken by Staudinger and Neale who identified the continuation of polymer chains into irregular amorphous networks and assumed cotton cellulose to be built up of almost continuous unit lengths [108]. It is now known that these continuous molecules form a primary and a secondary plant cell wall each consisting of 20-30% and 50% cellulose content respectively. The degree of polymerization (DP) varies for each plant, with the primary wall cellulose DPs to fall between either 250-500 or 2,500-4,000 and the DP in the secondary wall to fall between 10,000 and 15,000.[112] Cellulose is the main structural component in the cell wall but not the only component. The cell wall consists of cellulose fibrils and fibres interacting with matrix polysaccharides, called hemicelluloses. Lignin and pectin are two other matrix materials found in the cell wall, and they also interact with the cellulose fibrils to make up what is known as the cellulose-hemicellulose network.

3.2 Cellulose Nanocrystal Synthesis and Characterisation

In the mid-1900s the degradation of cellulose was of particular interest to scientists who employed scanning electron microscopy (SEM) to visualise the texture, on the colloidal scale, of cellulose fibres[113,114]. In the mid-1900s Ranby developed our understanding of the properties of colloidal cellulose and the chemistry of manipulating cellulose micelles[114,115]. Shortly after, in 1953 Mukherjee and Woods visualised what are now called cellulose nanocrystals (CNCs) by SEM analysis[116]. In 1959 Marchessault *et al*. included a

homogenising treatment to the hydrolysed cellulose crystallites which they observed produced a stable suspension and in gel form they observed liquid crystal textures[117]. Little more was published on the liquid crystal behaviour of colloidal cellulose until the 1990s when this unique behaviour was rediscovered by Gray *et al.*[33], whose work will be discussed further in Section 3.4.

Cellulose was degraded by acid hydrolysis to produce these CNCs, which is still the most common method used today[19,118–120]. The method takes cellulose in the form of wood, cotton or tunicates for example, which is then converted into a pulp via blending at high speed in water. Delignification takes place prior to this if necessary, which involves the removal of the matrix material lignin. A strong acid is then added to the pulp solution and stirred vigorously for a specified length of time. The acid protonates the ester bonds, breaking the cellulose chain bundles down into smaller crystals many of which will be nano-sized (Figure 3-2a). Further processing via filtration and centrifugation removes any larger aggregates reducing the size distribution of the crystals. Characterisation of the sulfate half-ester content on the surface (as shown in Figure 3-2b) of the CNCs can be determined by conductometric titration[121,122] and can be increased via TEMPO-mediated oxidation. TEMPO (2,2,6,6-Tetramethylpiperidin-1-yl) compounds oxidise cellulose monomer hydroxide groups to carboxylic acids[123,124] (Figure 3-2b) the presence of which increase the surface charge. This process results in the formation of double bonds between the 4, 5 carbon atoms in the ring. The electron used to form this bond is taken from the 1, 4 glycosidic linkage which breaks the backbone of the polymer chains.

Little is known about how the rod shape of CNCs is formed or hoe the acid interacts with the material to produce such morphology. Initial thoughts considered distinct regions of alternating amorphous and crystalline regions (Figure 3-2a).

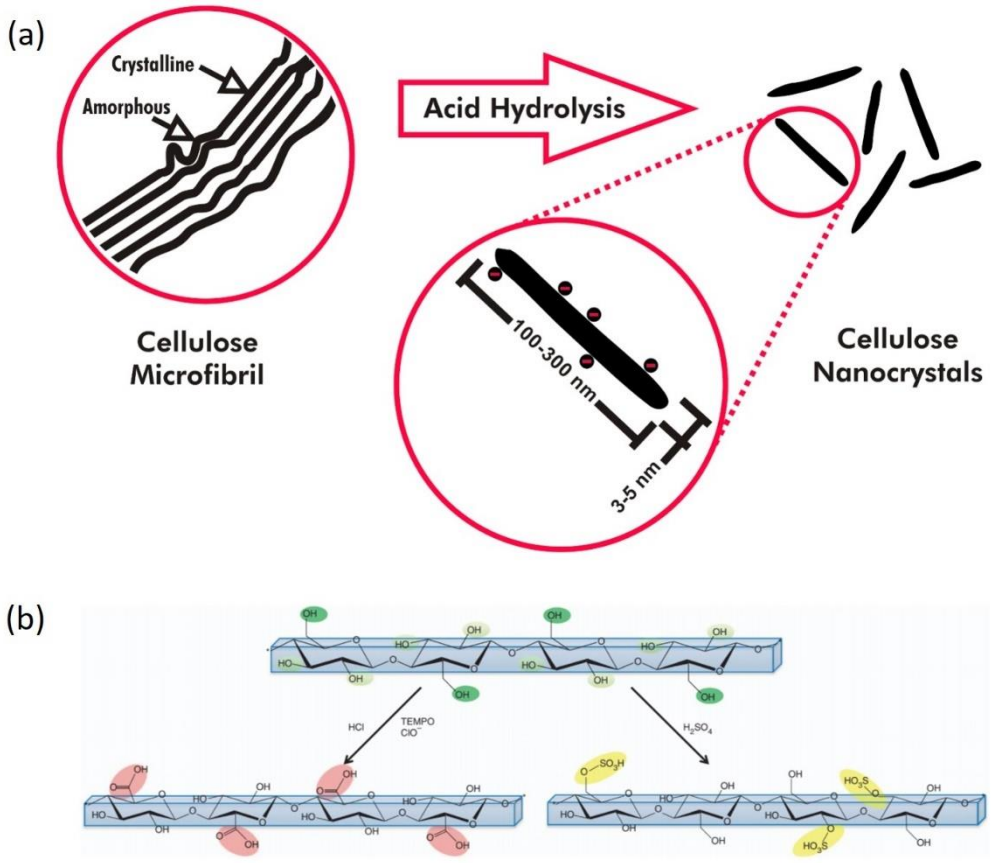

Figure 3-2 (a) Schematic showing the conversion of cellulose microfibrils to cellulose nanocrystals via acid hydrolysis. (b) Schematic of the two routes for producing anionic CNCs, resulting in carboxylate (left) and sulfate half ester (right) surface groups.

The acid would more readily break down the amorphous regions releasing the crystalline rods. This model contrasts with observations of cellulose where the presence of regularly repeating amorphous regions would be identifiable. The morphology of CNCs is well understood for various cellulose sources. Their morphologies range from rods to whiskers which possess a certain degree of surface roughness. In addition, how the cellulose chains emerge from plant cells to form highly crystalline bundles with 2-4 nm diameters[125] is also known. The individual cellulose chains are highly crystalline and possess chirality, a

physical feature which is perpetuated throughout the individual fibre bundles[126]. The aggregation of these fibre bundles into microfibrils could form much like match sticks would if they were stuck together with their long axis aligned parallel but arranged with ends at varying heights in an irregular brick like fashion. The gaps between the imperfectly packed fibre bundles are most likely responsible for the surface roughness of CNCs and it would then follow that hydrolysis acts more readily between neighbouring fibres releasing them from the bundle. It should also be noted that the amorphous hemicellulose network intertwined with the cellulose microfibrils is more readily hydrolysed than the resistant crystalline structure of cellulose. Once hydrolysed the breakdown of the hemicellulose may weaken the interfibrillar bonding and leave pores accessible to the acid during hydrolysis.

Once CNCs have been produced they can be kept as a suspension or undergo drying via lyophilisation[127–129]. Efforts to reduce the waste while maintaining high CNC yields have employed the use of milder acids which prevent the degradation of cellulose into soluble sugars which cannot be economically recovered. Instead the unwanted cellulosic solid residues are collected via centrifugation and converted to cellulose nanofibrils by mechanical nano-fibrillation[130]. Chemical treatment is necessary to produce CNCs but mechanical processes can be used to separate cellulose into the constituent cellulose nanofibrils (CNFs). High pressure homogenization, high-intensity ultrasonic treatments and cryocrushing are such techniques used to extract CNFs which may then undergo chemical treatment to form CNCs. Direct chemical treatment is preferential as it reduces energy consumption and yields CNCs with higher crystallinity[131].

Cellulose source materials vary, as do their properties[131]. The main sources of cellulose used to synthesise CNCs are plants, Algae, specific types of bacteria and tunicates. Plants provide an abundant source of cellulose the most commonly used are wood pulp and cotton

fibres. They produce highly crystalline, relatively low aspect ratio rod shaped crystals. Other plants of interest are jute, ramie, sisal flax and hemp. Highly crystalline cellulose is found in the cell wall of many types of algae. Some algae produce cellulose with degrees of crystallinity as high as 95%.[132] Specific types of bacteria produce cellulose pellicles which yield CNCs that have a unique nanostructure, high purity, good dimensional stability and greater mechanical strength than other forms[133]. Tunicates are marine invertebrates capable of producing large amounts of cellulose which they use to build leathery skeletal structures within their integumentary tissues[134]. They use enzyme complexes to produce cellulose with properties that may vary depending on the species. Tunicates produce long rod shaped CNCs that have the highest aspect ratio of the cellulose source materials.

Table 3.1 Overview of source dependent dimensions of CNCs. Reproduced from George *et al.*[133].

Source	Preparation method	Length (nm)	Width (nm)	Aspect ratio (L/D)
Wood	H_2SO_4 hydrolysis	100-300	3-5	20-100
Cotton	HCl hydrolysis	100-150	5-10	10-30
Ramie	H_2SO_4 hydrolysis	70-200	5-15	~12
Sisal	H_2SO_4 hydrolysis	100-300	3-5	~60
Valonia	H_2SO_4 hydrolysis	1000-2000	10-20	50-200
Tunicates	H_2SO_4 hydrolysis	>1000	10-20	~100
Bacteria	H_2SO_4 hydrolysis	100-1000	10-50	2-100
Bacteria	HCl hydrolysis	160-420	15-25	7-23

The various length and widths of the CNCs produced from different source material are listed in table 3.1 above. The range in CNC dimensions offers a selection when considering a CNC source for a specific application, particularly as a reinforcing material in composites. CNCs are highly crystalline and offer boast good mechanical properties. The first experimental determination of the crystal modulus of cellulose was conducted by Sakurada et al. By using x-ray diffraction combined with a series of weights to load fibre bundles in tension they arrived at a value of 138 GPa for cellulose-I[135]. Others later confirmed this via similar experiments on plant cellulose fibres[136] and more recently the crystal modulus has been determined using sound velocities of X-rays in plant fibres. These experiments yielded higher values of 220 GPa[137] which is claimed to be unlikely accurate[31], particularly when theoretical derivations have given values in the range 100-160 GPa[138–140]. What is said to be likely is that once the amorphous fraction of cellulose is removed by hydrolysis then the resultant CNCs should have a modulus close to that of the crystal. To investigate this further, on what is a difficult scale to work with, Sturcova *et al.*[141] used Raman spectroscopy to follow molecular deformation of the CNCs while deformed in a 4-point bending test and estimate the modulus. It was Hamad and Eichhorn in 1997 who first used this technique to show that molecular deformations could be followed by mapping the shift in the characteristic Raman peak (1095 cm^{-1}) produced by cellulose[142]. For tunicate CNCs a value of 143 GPa was obtained and for other acid hydrolysed material values of 50-100 GPa[143]. More direct mechanical measurements have been made using an AFM bending stiffness technique where the deflection of the probe pressed onto an affine object is measured. The reported values were 145.2-150.7 GPa[144] for unmodified and TEMPO modified tunicate CNCs.

3.3 Mechanics of drying droplets

CNCs in solution will form chiral nematic crystalline phases above a critical concentration[33,39,145]. In addition to the spontaneous self-assembly of CNCs in solution are the factors that influence film formation in droplets. The substrate, the concentration and size of the suspended nanoparticles all effect the droplet behaviour[146,147]. These additional factors influence the self-assembly process and are important to consider because the liquid crystalline phases formed can be 'frozen' into a dry film[19,148–153].

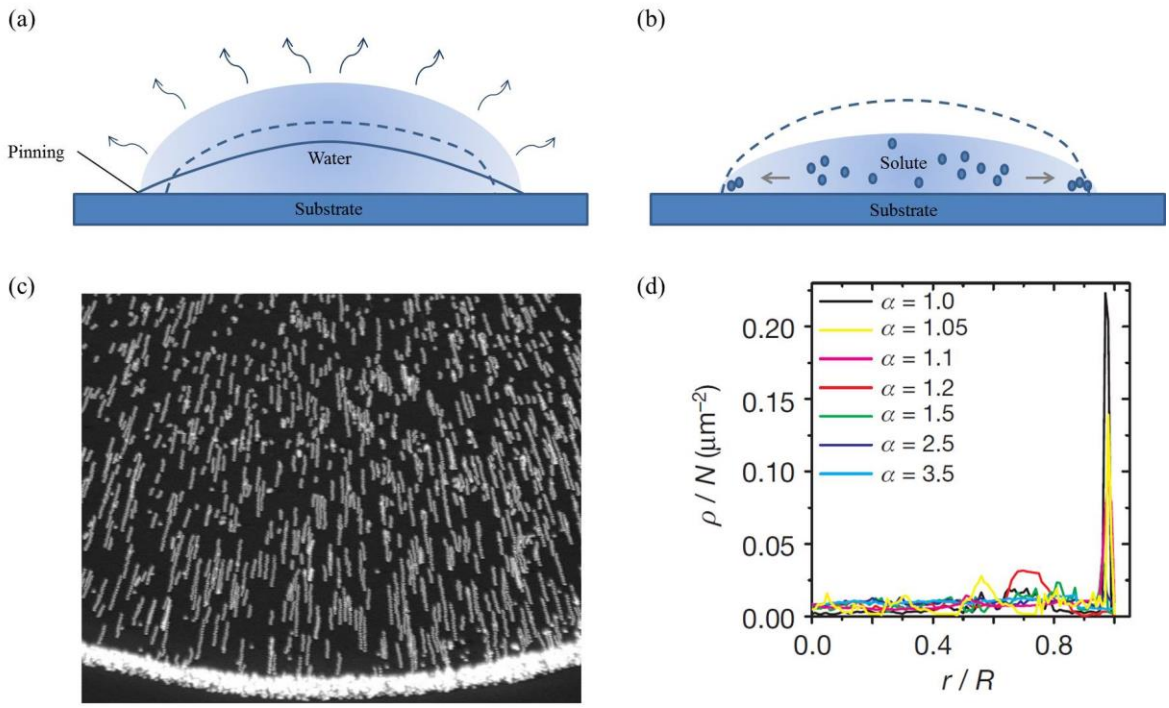

Figure 3-3 (a) Schematic highlighting the receding drop profiles of free moving contact lines (dashed line) and pinned contact lines (solid line). (b) Low contact angle results in faster rate of evaporation at the edge of the droplet. Water is replenished from the centre of the drop which carries with it the suspended solute material. (c) Spheres in water during evaporation. Multiple exposures are superimposed to indicate the motion of the microspheres. Reproduced from Deegan *et al.*(d) The Droplet-normalised particle number density, ρ/N, plotted as a function of radial distance from the centre of the drop for ellipsoidal particles with various major-minor axis aspect ratios (α). Reproduced from Yunker *et al.*[154]

The evaporation of solvent from a droplet is a non-equilibrium process, is complex and difficult to control. The resulting phenomenon is the coffee-ring effect and is produced by the interplay of factors like surface tension, fluid dynamics, evaporation and capillarity. As the solvent of a suspension evaporates its edges are pinned by the suspended particles which means the edges cannot recede towards the middle of the drop and a constant diameter is maintained (Figure 3-3a)[155]. This occurs despite the edges of the drop being thinner than the middle. Thus, to maintain a liquid region at the edge liquid must be replenished from the middle creating capillary flow towards the edges of the droplet[156]. The coffee-ring is produced as suspended particles are carried in the flow and deposited at the edge (Figure 3-3b)[154]. The morphology of the particles can influence the contact angle which will affect the rate of capillary flow[157,158]. In addition to the capillary flow, small temperature differences generate surface tension gradients between the top of the drop and the contact line which induce solvent movements called Maragoni flow[159,160]. The term coffee-ring comes from the stain often left behind by a coffee cup on the surface it was sitting on. The dried coffee ring is darkest around the edge and lightest towards the middle. The coffee-ring is also effective in systems with constituents ranging from large colloids[159,161–163], to nanoparticles (such as CNCs)[164] and to individual molecules[165]. An example of a coffee ring is shown in Figure 3-3(c) where microspheres in water have accumulated toward the edge of the drying droplet. As the solvent is replenished solute material, in this case spheres, is deposited towards the droplet edge where, in the final dry film, it is found to be radially distributed with a concentration distribution which is significantly higher at the edge (Figure 3-3d). The plot in Figure 3-3 (d) shows how significantly high the density of microparticles can be towards the edge of the dried

droplet, where the density variation towards the centre is negligible. Droplets of CNC suspensions behave as described above. The droplets are pinned and the replenishing solution from the interior of the droplet deposits higher concentrations of CNC material around the edge of the drying film.

Particle morphology has been found to affect particle deposition. One such difference is between smooth anisotropic ellipsoids and smooth isotropic spheres where anisotropic ellipsoids deform the air-water interface and smooth isotropic spheres do not[166–168]. The deformation of the air-water interface induces a strong interparticle capillary attraction between the ellipsoids causing them to form a loosely packed network. This network can cover the entire air-water interface leaving a uniform distribution of ellipsoids when evaporation has finished. Spheres on the other hand simply pack densely at the drop's edge producing a coffee-ring. CNCs are rod shaped and Mashkour *et al.* showed that upon reaching the drying line the rod-shaped CNCs undergo up to a 90 degree rotation to align parallel to the edge of the film[169]. The schematic in Figure 3-4(a) shows a section of film and highlights how the long axis of the CNC rods is aligned parallel to the dry edge. CNCs reaching the edge in a perpendicular fashion rotate to align with parallel with the growing nematic arrangement. Figure 3-4(b) highlights this alignment in a dried CNC film viewed between crossed polarisers and Figure 3-4(c) highlights the difference in organisation of CNCs alighed towards the edge of a dry film and CNCs in the middle of the film. Mashkour *et al*. described the surface tension torque (STT) phenomenon which is responsible for the CNC rotation at the edge of the drying film. CNCs that are close to the dry boundary layer (shown in Figure 3-4a) are affected by a STT which results as a function of the surface tension force of the liquid and the contracting force between two immiscible materials. A very clear drying effect is seen on the formation of a CNC film

formed via EISA which is important to consider when developing homogenous optically active films. Peiss *et al.* also showed that the relationship between the rate of evaporation and the radius of drying drops is non-linear[170].

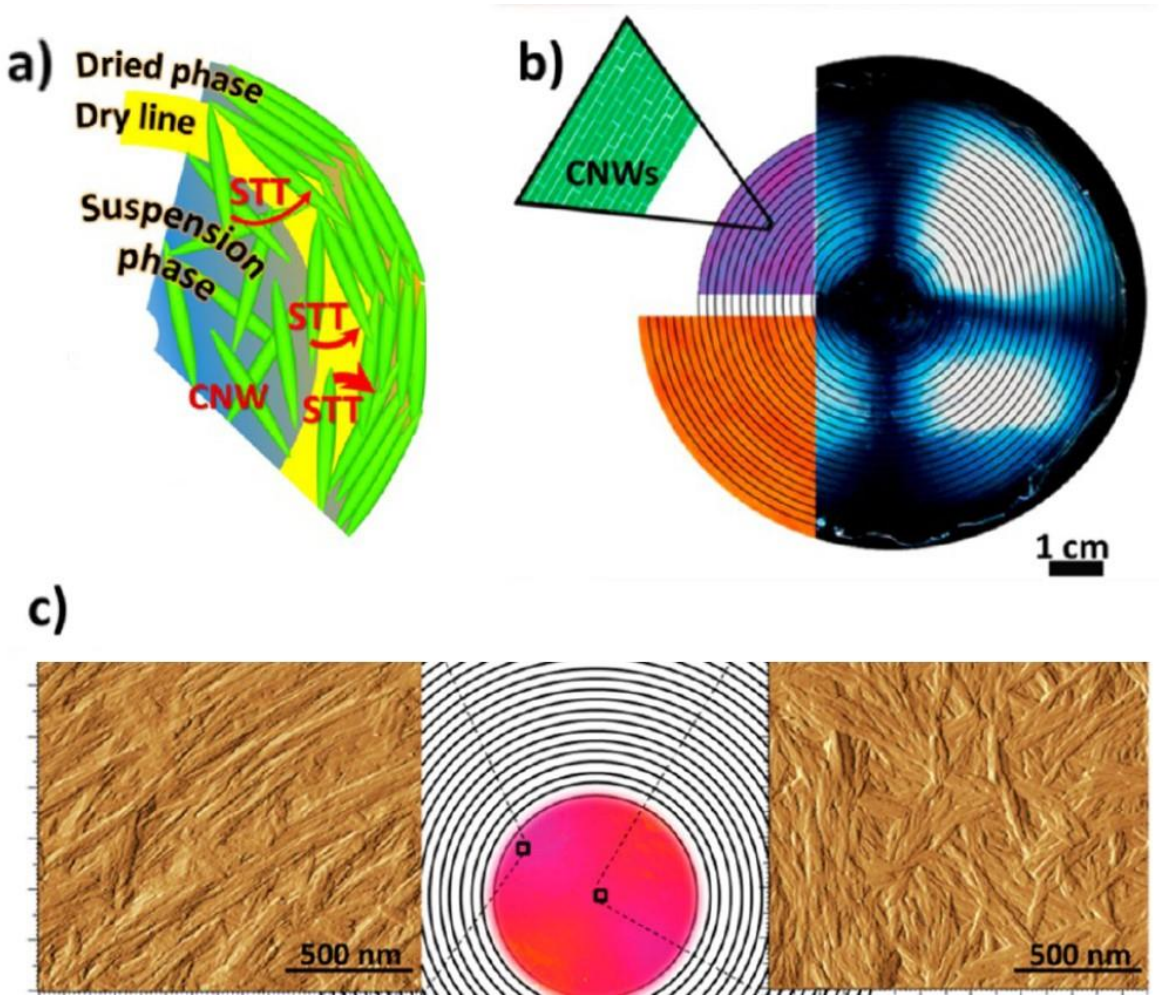

Figure 3-4 (a) A schematic showing the approach to and rotation of CNCs at the drying line. (b) Observation of a curved nanopatterned CNC-PVA film between crossed polarised films. (c) AFM micrographs from the surface of the CNC film in (b). The left image was taken toward the edge of the film and the right image was taken from the centre of the film. Reproduced from Mashkour *et al.*[169].

The combined effects of these behaviours contribute to the inhomogeneous distribution of solid material within EISA films and may help to explain the variation in optical behaviour across such films[148]. CNC spheres have been formed using microfluidics to avoid the need for a substrate which means a more even evaporation rate from the spherical droplet[34]. The behaviour and formation of the CNCs at the droplet surface interface are the same and align parallel to the surface[34].

One of the difficulties in measuring the local particle density of anisotropic particles with large packing fractions is the surface saturation. Individual particles cannot be differentiated. The AFM images in (c) give a sense of directionality but no confidence could be had in a quantitative study of local particle density. An understanding of local particle density is important when trying to understand optical behaviour which is of interest to this study. The packing of and concentration of particles determines parameters such as refractive index and the pitch of the cholesteric structures formed which in turn effect optical behaviour. Defects may also be present where variations in local particle density are found against a constant final dry film height. Defects also affect optical properties. To overcome this problem, a novel technique was used to quantify particle distribution using a combination of profilometry and optical microscopy.

3.4 CNC Thin Films

CNC thin films can be prepared simply by casting a CNC suspension on a substrate and allowing the solvent to evaporate. As the solvent evaporates the CNC concentration increases and crystalline phases start to form in the shape of ellipsoidal tactoids[171] (Figure

3-5a). The tactoids are crystalline phases of ordered CNCs in solution. Liquid crystalline phases in CNC suspensions were observed by Werbowyj et al.[172] in 1976 and confirmed to form chiral nematic phases by Revol et al. in 1992[33]. The microdomain tactoids possess a lamella-like structure made up of nematic layers with a perpendicular chiral twist[33,171]. The illustrations in Figure 3-5 describe what happens as the evaporation of the solvent progresses. The tactoids coalesce to form layers that lie parallel to the substrate and film surfaces (Figure 3-5b-c). The chiral twist is maintained by a small degree of rotation between each layer. Mu and Gray explained the appearance of ring formation to be a product of the mass transfer effect on CNC concentration and thickness throughout the film[148]. The variation in concentration is responsible for the variation in the pitch of the frozen in chiral nematic structure [148].

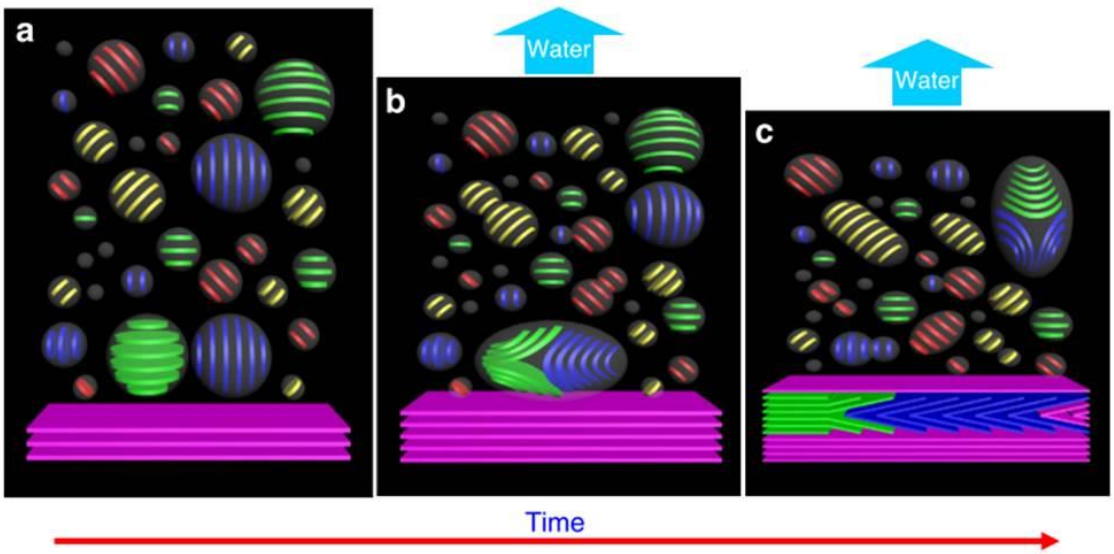

Figure 3-5 Models of the structure and transformation of tactoids reproduced from Wang et al. 2015[171]. (a-c) Schematic diagrams of the tactoids and their transformations as the solvent evaporates from the CNC suspension. A typical fusion mode which leads to the defects of folded layers is shown.

The layers produced in the final film still possess the helicity in the z-axis formed in solution (Figure 3-6a). The periodicity of the resulting chiral structure gives rise to an optical band gap and the films then interfere with visible light to express optical properties such as iridescence, an example of which is shown in Figure 3-6(b). The optical characteristics of chiral structures were explained in Section 2.3. Filters are required to distinguish between the various polarisations of light reflected from the film. The chirality in CNC thin films is reported to preferentially reflect Left Handed Circularly Polarized (LCP) light, indicating a left handed twist in the cholesteric structure[39,173]. The Bouligand curvature observed in SEM images also confirms that curvature is consistent in one direction only[39,171,173].

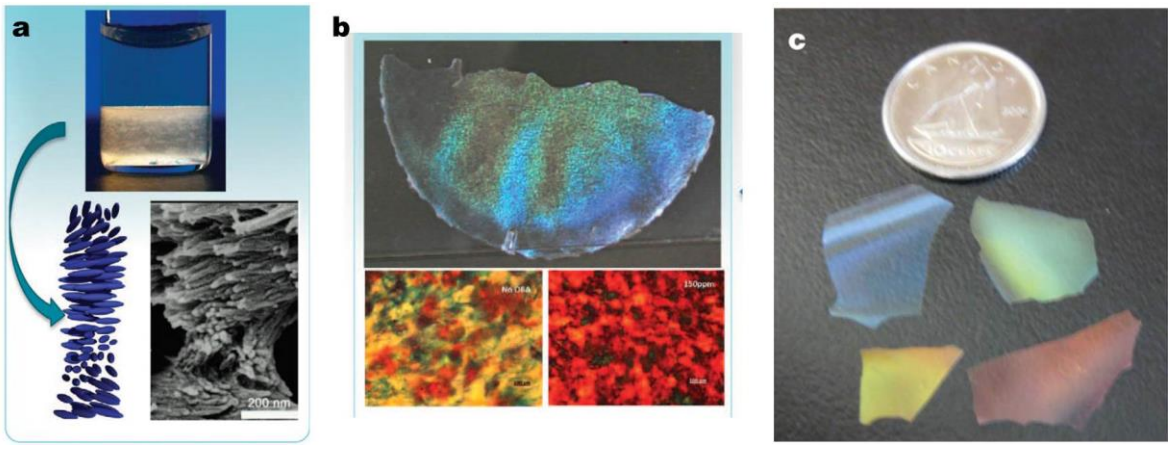

Figure 3-6 Images showing the utilization of CNC chiral nematic phases. (a) The chiral nematic liquid crystal phase and its coexistence with an isotropic phase in a CNC suspension, reproduced from Lagerwall *et al.*[19] Below is a schematic and an SEM image, reproduced from Majoinen *et al.*[39], of the helical arrangement of CNCs. (b) Images expressing the optical characteristics of CNC thin films, reproduced from Zhang *et al.*[174]. (c) Photograph of Silica films made by templating the CNC helical structure, reproduced from Shopsowitz et al.[175]

Cellulose fibrils have been observed to possess a right handed twist[38,126] which would intuitively produce a left handed twist when stacked[37]. The angle dependence of the reflection of LCP light has also been shown to be consistent over a broad range of angles[173] which is only true for the still liquid state as the tactoid microdomain phases are randomly oriented and reflect at all angles. Once the film has formed and is dry, then angle dependence of reflected CPL decreases with increasing incident angle[173]. The reflection of both LCP and RCP sates has only been reported to reflect from engineered films[176] and natural systems that include a quarter wave plate in a cholesteric structure which changes the polarisation state of the incident light[13].

Mechanical and magnetic interference during film formation can induce alignments to produce films with tuneable optical properties[63]. These manipulate the properties discussed and have not yet introduced new optical properties. The optical structures CNCs form can also be used as a template for introducing optical periodicity into materials with different refractive indices[177–179] (Figure 3-6c) and to develop inverse glass structures that scatter light[180]. Iridescent colours and control of the chiral helix orientation in CNC thin films have been shown to correlate to the structural properties and homogeneity respectively of the films. These effects were induced by applying a shear flow to the drying suspensions[181,182]. Many have also demonstrated tunability by chemical treatment, such as introducing ions and other molecules to the CNC suspension/CNC surface[44]. The addition of glucose (1-10%) to CNC suspensions was shown to have this effect. Higher percentages of glucose inhibit mass transfer in the drying droplet and the formation of shorter pitched structures shifting the reflection band to longer wavelengths, oranges and reds[148]. Another chemical method by Azzam *et al*. involved grafting the thermoresponsive polymer polyetheramine on to the surface of TEMPO-oxidised CNCs[183]. This functionality

introduced variation in the viscoelastic properties of the final suspension as a function of temperature[183]. The result was a reversible temperature-triggered liquid to gel transition. Tunability may also be controlled by mechanical treatment. Chen *et al*. showed that large iridescent CNC films that are highly oriented can be made using a vacuum assisted self-assembly method with a prolonged ultrasonic pretreatment[184].

Much has been done to influence and control the pitch of the photonic band gap and overall homogeneity of CNC thin films[19]. There are, however fundamental issues related to the sensitive balance between liquid crystal formation and gelation/glass formation and the possibility of controlling the alignment of CNCs in either helical or non-helical states that have yet to be fully understood. This thesis will show that the variation in film structure induced by the drying mechanics can produce optical behaviours not yet seen in CNC thin films. It will also demonstrate that a tunable, homogenous Bragg-reflecting film can be made by combining CNCs and other organic materials.

Cellulose

Chapter 4 Layer by Layer Assembly

4.1 The development of Layer by Layer Assembly

Early in the 20th Century the fundamental properties of liquids and solids were of particular interest to scientists such as Lord Rayleigh and Henri Devaux. Among them was Irving Langmuir, who with his contemporaries discussed and established the nature of chemical forces and their role in the cohesion of and interaction between a broad range of solids and liquids. Their experiments included observations of oil thin films on water and measurements of film thicknesses and surface tensions. They used small water troughs like the one shown in Figure 4-1a. Devaux was able to determine the areas covered by films from weighed amounts of oils and readily calculated the film thickness which he found corresponded to, what would be, the diameter of a single molecule. In the case of triolein, the thickness of the film created on water was calculated as 1.1 nm which corresponded to the theoretical value for the diameter of a molecule of triolein at 1.13 nm [185]. Able to measure film thicknesses, Devaux could then correlate this to the physical properties of the liquids. Of his thin film work, Devaux concluded:

"This general conclusion: the characteristic mechanical properties corresponding to certain states of a body, the surface tension of a liquid or the rigidity of a solid, persist almost intact down to molecular thicknesses, disappearing abruptly the minute we go further."

Inspired by this Irving Langmuir went on to explain the cause of spreading of oils on water and in 1941 while working at General Electric he demonstrated that one layer of thorium ions is absorbed on a monomolecular layer of barium stearate on water. He then showed that when this thoria-covered surface is brought into contact with dilute solution of sodium silicate, a layer of silica is absorbed. He explained these interactions were due to the fact that the adsorption of ions on a surface is limited to a single layer [186]. Out of these experiments and the new understanding they led to, grew ideas of being able to assemble thin films by depositing monomolecular layers on to substrates. Langmuir soon went on to develop these ideas and created techniques for depositing thin films from liquids to solid substrates. Working with Langmuir, Blodgett invented a vertical dipping lever [187] (Figure 4-1a-b) to immerse a solid substrate, aligned perpendicular to the liquid surface, in an oil covered trough. A monolayer film was transferred from the liquid surface to the surface of the solid substrate. A short while later Schaefer designed a horizontal deposition technique (Figure 4-1c) that transferred the monolayer without the need for immersion. The illustrations in Figure 4-1 show how these techniques worked and include the published illustration of the original setup used by Blodgett (Figure 4-1a).

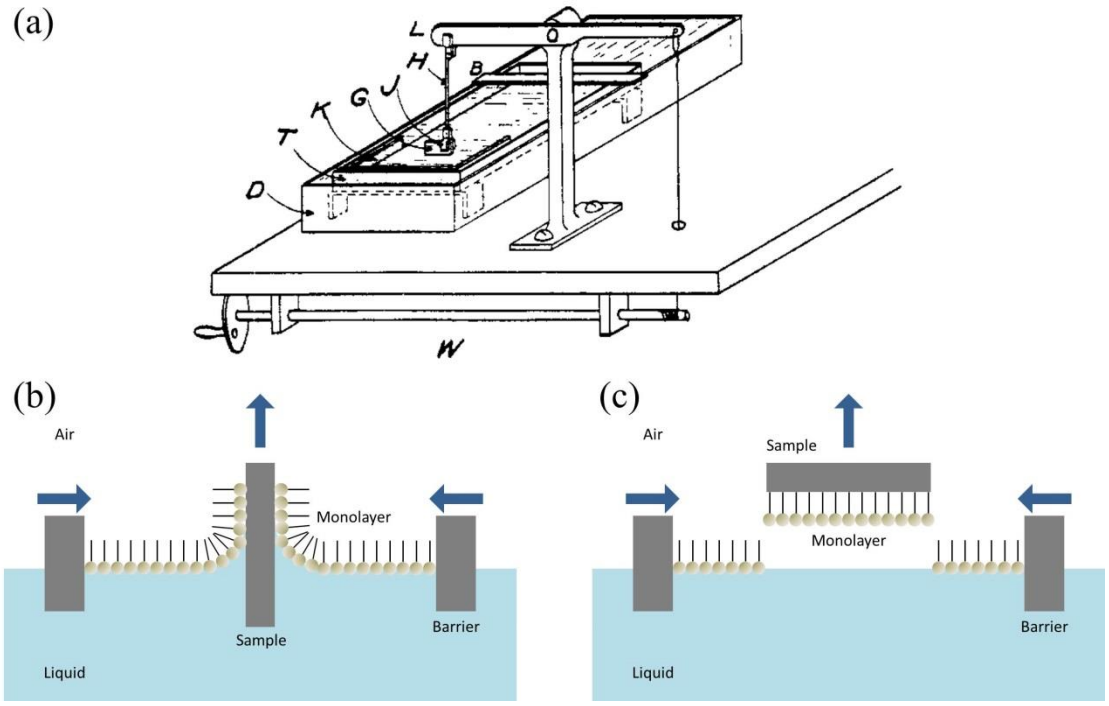

Figure 4-1 a. Illustration published by Blodgett of the layer by layer setup used to deposit monomolecular layers onto a substrate. The letters are as follows: T: trough, D: water bath, B: metal barrier coated with paraffin wax, K: pen made of detachable strips of glass, G: glass slide substrate, L: Lever, W: windlass, H: rod, J: clamp. b-c. Langmuir-Blodgett and Langmuir-Schaefer vertical and horizontal methods for depositing monomolecular layers from a liquid to a solid substrate.

In the 1960s Iler went on to develop our understanding of the LbL technique and introduced an adaptation of this technique using aqueous solutions of colloidal particles to produce multi-layered thin films, some of which displayed interference colours [188]. The method Iler used was simple, the process consisted of a substrate, in this case black plate glass and well-characterised inorganic solutions. The black plate glass was siliceous and anionic in nature, presenting a hydrophilic surface to the first 0.25% suspension of boehmite alumina (cationic in nature) it was wetted with. The excess solution was rinsed off the glass surface and the substrate was air-dried. The substrate was then wetted with an

anionic solution of 2% colloidal silica adjusted to pH 3 and again followed by rinsing and drying. Iler identified two factors the formation of visible films depends on [188]:

1. *When a single layer of colloidal particles is adsorbed from an aqueous solution onto a smooth, wettable solid surface of opposite ionic charge, no further adsorption occurs because the ionic charge on the surface is reversed and the remaining particles in solution are repelled and are subsequently washed off. By repeating the operation, films of any desired thickness can be built up.*
2. *When the thickness of the adsorbed film is over about 50 nm and thus approaches the order of magnitude of the wavelength of visible light, the film becomes visible in reflected light, providing the refractive index of the film is between those of air and of the substrate.*

The formation of thin films is driven by the difference in electronegativity of oppositely charged particles which gives rise to the adsorption of monolayer thin films onto solid substrates. Monolayers are produced, because once the initial layer has bonded the charge is altered and any remaining particles are repulsed and subsequently washed away.

4.2 Electrostatic Self-Assembly

The underlying principle behind LbL is the electrostatic interaction between oppositely charged atoms within particles and molecules. This process is known as electrostatic self-assembly (ESA). These interactions are responsible for the diffusion-driven kinetics of the assembly process and result in the bonding of neighbouring atoms with different electronegativties. The unpaired electrons of atoms in neighbouring molecules attract positively charged atoms. Such non-bond interactions occur between the oxygen atoms in water molecules and is responsible for the folding of long chain polymers. Amphiphilic

molecules possess both polar and apolar parts. An example of an amphiphilic molecule (or amphiphile) is a fatty acid. Electrostatic interactions cause these molecules to form bilayer membranes that make up endothelial cell walls. They also self-assemble in solution to form liposomes and micelles. Techniques to produce vesicles have applications in drug delivery. The natural charges present in polymeric and particulate materials are utilised to deposit thin layers and build multilayer stacks. An illustration of this is provided below in Figure 4-2.

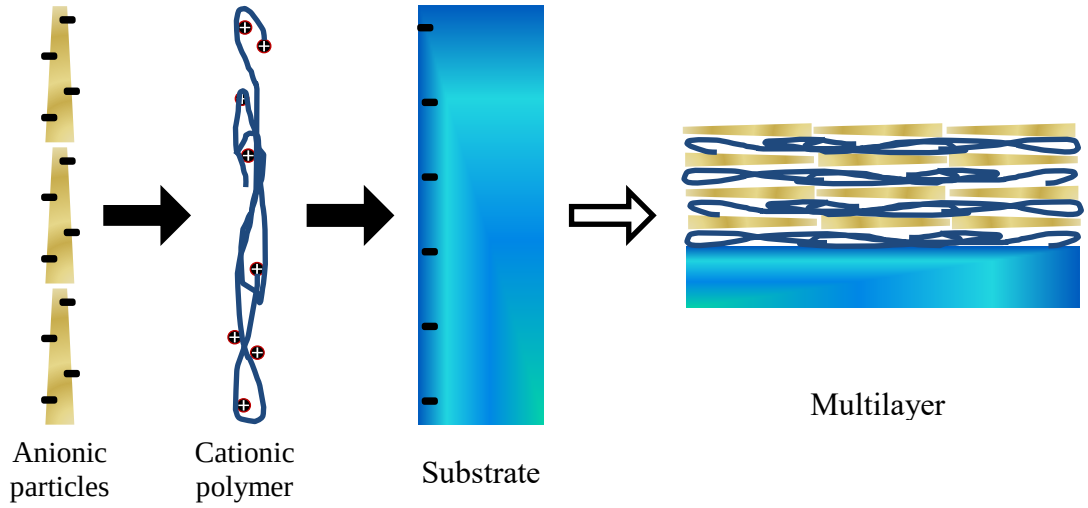

Figure 4-2 Schematic of the layer deposition by electrostatic interaction to produce multilayer thin films.

This stepwise growth process involves consecutive cycles of alternating adsorption of polyanions and polycations onto a charged surface. The material adsorbed is limited to the remaining charge on the current surface following neutralisation of adsorbed material. Resaturation leads to a reversal in charge on the substrate and any excess unbound material is either repelled or washed off before dipping into a subsequent solution[189]. A cation or anion needs to have a sufficient charge density, bearing a minimal number of charged groups below which ESA will not work. Quantifying this is difficult due to the other

variables that affect the process such as the additional strong interactions of the starting materials which may reduce the minimum charge required[190]. With a limit on adsorption, the build-up of layers can be finely controlled. Such tuning is possible due to the manner in which precise control of thin film structure is possible through adjustment of solution concentration[191,192], pH/ionic strength,[193,194] temperature[195,196], molecular weight[197,198] and deposition time[31,199] of the aqueous deposition mixtures.

4.3 LbL: A Universal Technique

Over the past two decades the demand for functional thin films for high end applications has increased. LbL is now a prevalent method used to produce thin films and various production techniques have been developed (Figure 4-3). These techniques are illustrated in Figure 4-3 and include spin and spray coating and the use of electromagnetism and fluidics to induce adsorption. The immersive technique (Figure 4-3A) is the technique described in Section 5.1 introduced by Iler and is the technique used in this study. Following Iler's approach a substrate is simply immersed alternately into solutions of cationic and anionic polymers/particles where suspended material is adsorbed onto the surface to cover the substrate in a uniform layer with a given thickness. The spin coating method (Figure 4-3B) utilises the technology used to apply coatings via spinning of the substrate[200]. The spinning can either occur during material application or immediately after the material has been applied[201,202].

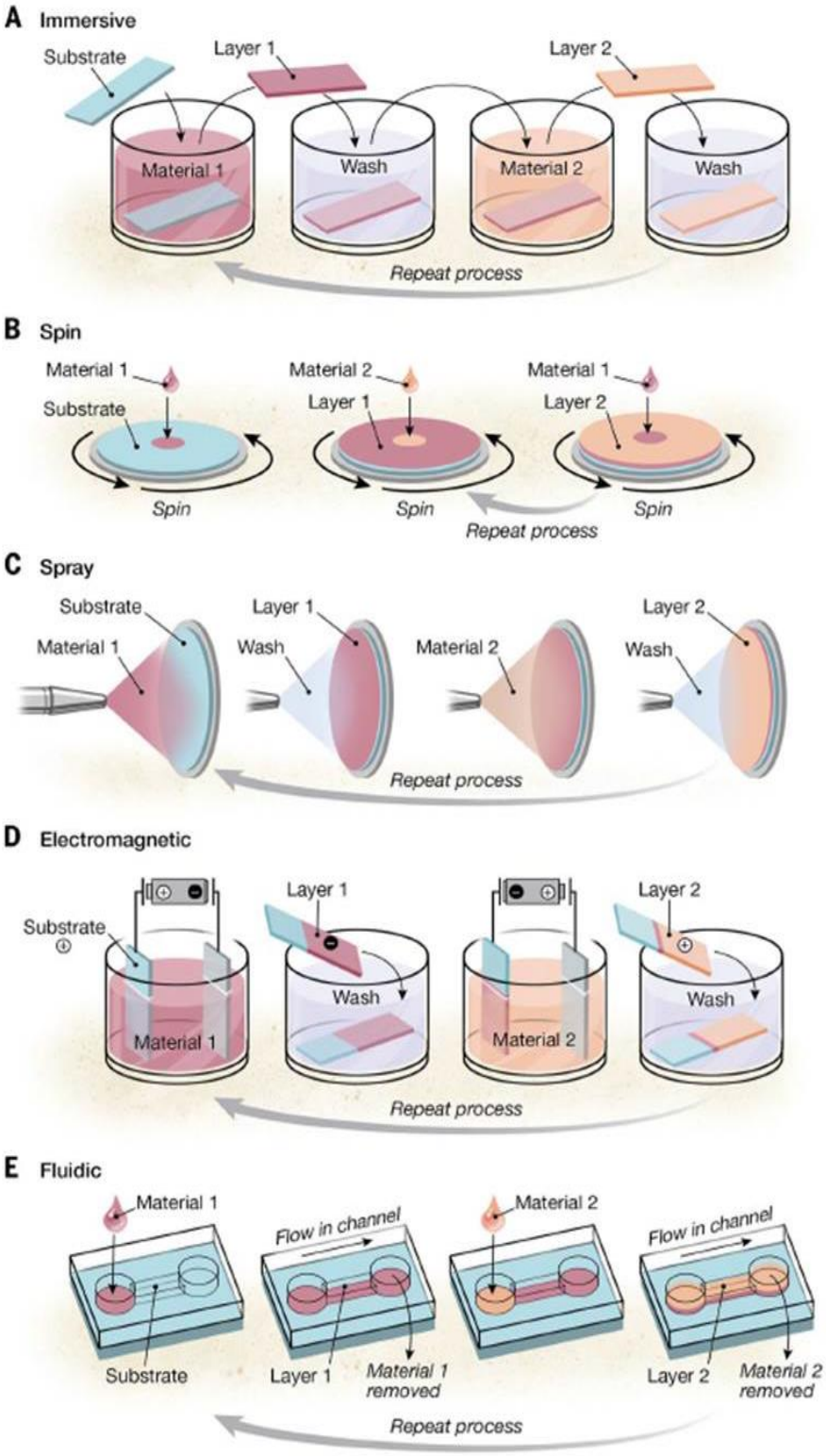

Figure 4-3 Layer by Layer (LbL) assembly technologies. (A-E) Schematics of the five major technology categories for LbL assembly published by Richardson et al.[203]

The spinning method has the advantage of being quick (~30 s layer deposition) but is limited to small sample areas that must be flat, excluding complex shapes accessible to the immersive technique. Layer deposition can also be achieved by aerosolising polymer solutions and spraying them directly onto substrates (Figure 4-3C)[204]. This method can be applied to larger and more complex geometries and would require dynamic control of the spray nozzle to ensure an even distribution. For flat substrates, the spray assembly method also lends itself well to operating on a commercial scale. Figure 4-3E illustrates the electrodeposition method where an applied electric charge or magnetic field is used to effect the layering process[205]. Electrodeposition can be used to deposit ions, polymers and colloids onto the electrodes themselves or onto substrates placed between the electrodes[206]. The final method, fluidic assembly, makes use of a vacuum or pressure to move liquids through channels to coat the channel walls[207]. This method is more equipment intensive but has the advantage of being able to apply coatings to unusual materials such as nanocellulose aerogels and liquid crystals. This approach can also be used to deposit materials like reduced-graphene oxide in a uniform multilayer[208,209].

4.4 A Method for Fabricating Bragg Stacks

Methods such as thermal evaporation, spin-coating, multi-layer extrusion and sol-gel chemistry are techniques that have been used to successfully fabricate 1D photonic crystals, but are limited in their range of materials and scale. Other methods used to deposit Bragg stacks include chemical vapor deposition (CVD)[210,211] and physical

vapor deposition (PVD).[212,213] These techniques are size-limited and have lots of process complexity. An additional approach is the use of sol-gel processing via spin coating, dip coating or casting. Despite its simplicity compared to vapor deposition, sol-gel techniques suffer from issues of poor uniformity and cracking (heat treatment is required to improve this) over larger areas.[22] The LbL technique stands as a potential solution to all of these problems, offering versatility, use of a broad range of materials and scope for fine-tuning of both structure and properties. The multifunctionality of LbL assemblies enable its application in drug delivery[214,215], gas barrier/separation[216,217], biosensing[218,219], wettability control[220,221] and flame retardency[222,223]. Most importantly, this simple deposition process makes industrialization possible, with the potential for scaling up to a continuous dipping[40] or even a continuous spraying process.[41] The versatility of the LbL technique means that cellulose nanocrystals can be introduced and more will be discussed on their suitability in Chapter 6. Successful, affordable fabrication of such structures could make Bragg reflectors useful for sensing[21,22], optical filters[24,25], and the widespread replacement of pigment-based coatings[26,27]. The iridescent effect can only be generated by structural systems and is particularly conspicuous to the human eye which also lends them to industries where aesthetics is important. The complexity of these structures also makes them useful for security, where marks of authentication are required.

Demonstrated in this thesis is the suitability of CNCs for an LbL regime and the use of this regime to produce tunable iridescent thin films. The significance of this is found in the fact that cellulose is the most abundant resource on the planet, which when combined with the adaptability and scalability of the LbL process makes for a cost-effective method for producing a broad range of colour solutions for a host of potential applications.

Chapter 5 Experimental Methods

CNCs were used to form photonic structures via an LbL deposition technique and EISA. The following sections will outline the materials and methods used to fabricate the thin films and characterise their structural and optical behaviour. Also presented here are the methods used to calculate CNC EISA thin film volumes and measure the distribution of CNCs across the diameter of the films.

5.1 Synthesis of CNC photonic structures

5.1.1 Synthesis of LbL Bragg stacks

The method used to fabricate CNC Bragg stacks was based on the immersive LbL deposition method described in Section 4.3. The layer-by-layer deposition technique provided the control required building up layers with specific thicknesses. The technique

also accommodates the use of a broad range of materials which can be manipulated to obtain tailored refractive indices.

5.1.1.1 Synthesis of cellulose nanocrystals

CNCs were derived from cotton using sulphuric acid hydrolysis, adapted from the method published by Clift *et al.* [224]. Following this method, 5.2 g of Whatman No.1 filter paper were shredded into a Waring blender with 250 ml of deionized water. The mixture was blended at high speed to form a pulp that was subsequently poured into a beaker and placed into an ice bath where the solution temperature was maintained below 20°C while 140 ml of 98% sulphuric acid was slowly added. The solution was rigorously stirred throughout. Following the addition of acid, the solution was heated to 50°C and held for 4.5 hours. The mixture was then cooled to room temperature and the CNC solution was repeatedly washed via centrifugation at 3400 rpm for 15 minutes. At the end of each centrifuge cycle the acidic supernatant was discarded and replenished with deionized water. This process was repeated until the suspension reached a pH of 4, after which the suspension was dialyzed for approximately 24 hours in a homemade dialysis unit until the pH was neutral. To remove larger aggregates the suspension was probe sonicated and centrifuged at 10,000 rpm for 5 minutes. The CNCs were retained as a suspension and visualised using transmission electron microscopy (TEM). TEM is described in Section 5.2.3. The length and width of the synthesised CNCs were measured from TEM images using ImageJ software. The data was fit with a Gaussian curve.

5.1.1.2 Conductometric titration

The stable CNC suspension formed is one good reason why CNCs are suitable for an LbL regime. The attractive electrostatic forces between charged particles is the driving force behind particle assembly in the LbL process and means materials used in this method possessing a charge have an advantage over molecules/particles bonded by the weaker van der Waals forces. For effective transfer from a solution to a solid substrate, particularly as far as the immersion technique is concerned, the material also needs to form a stable and well dispersed suspension. These two conditions are sought after for materials used in an LbL process. In the case of CNCs the acid hydrolysis process results in the attachment of sulphate half ester groups to the sixth carbon branch of the CNCs (Figure 3-2b). The sulphate ester groups give the CNC surface an anionic charge which enables CNCs to form a stable suspension in water. This charge also contributes to the diffusion rate onto the immersed substrate. The charge density of CNC particles can be quantified by conductometric titration against a dilute sodium hydroxide (NaOH) solution[225]. The technique indirectly detects surface sulphate-ester groups through the consumption of protons which leads to the neutralisation of the solution and an eventual build-up of excess NaOH. This experiment was based on the method presented by Jorfi *et al*.[226], where 50 mg of CNCs were suspended in 15 ml of aqueous 0.01 M HCl. After 5 minutes of stirring and 30 seconds of probe sonication, the suspension was titrated with 0.01 M NaOH. An Oakton conductometric 2700 meter was used to measure the conductivity (μS) of the suspension. The titration curve produced was evaluated by considering the three regions generated. These regions are magnified in the curve plotted in Figure 5-1 and the data are fitted to separate linear regressions. The conductivity decreases as the protons associated with the acid sulphate esters are consumed and replaced by sodium cations. The conductivity then increases once the required amount of NaOH for neutralisation is exceeded. A control

experiment was run using a solution without the presence of CNCs to assess the accuracy of the titration volume, the value of which was subtracted from the volume determined for the titration containing CNCs.

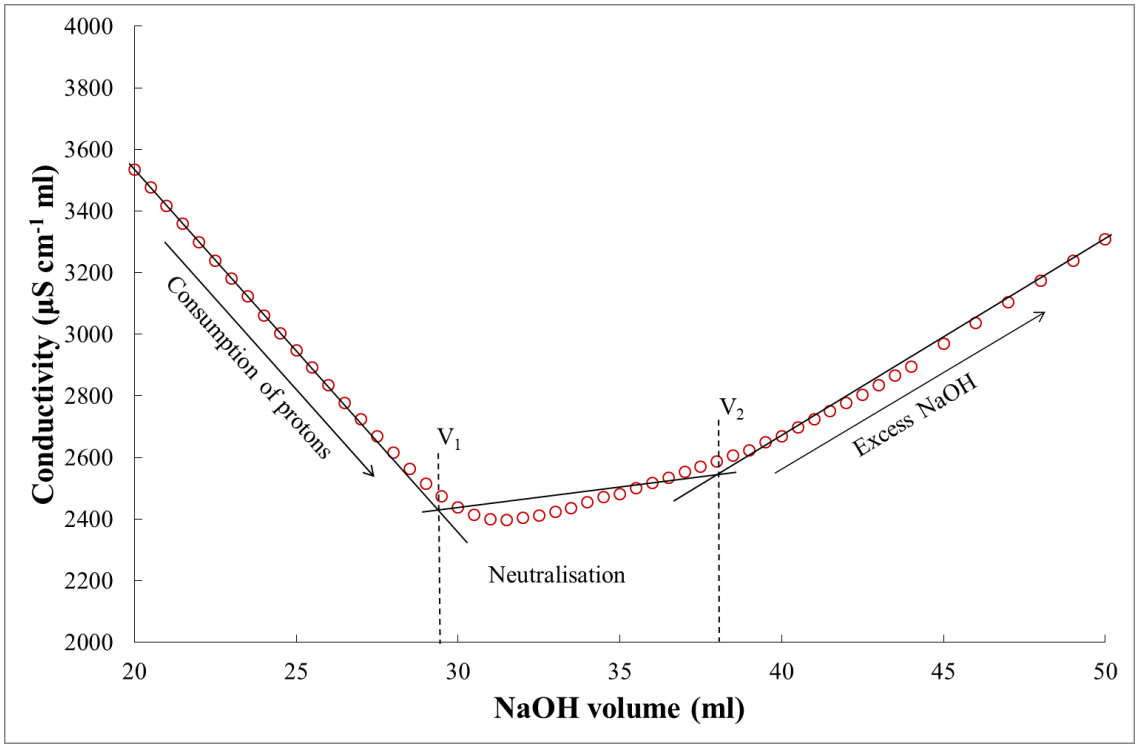

Figure 5-1 Typical titration curve showing conductivity as a function of NaOH volume of an aqueous suspension of CNCs.

The concentration of the sulphate charge density was calculated using the equation

$$\frac{m_{SO_3^-}\,(\text{mmol})}{m_{cellulose}\,(\text{kg})} = \frac{C_{\text{NaOH}} \times V_{\text{NaOH}}}{\text{W}_{\text{CNC}}} \times 10^6 \qquad (38)$$

where C_{NaOH} is the concentration of the base (0.01 M), V_{NaOH} is equal to V_2 minus V_1 and is the volume of NaOH used to titrate the weak acid, and W_{CNC} is the mass (g) of sulphated CNCs employed for the measurement.

5.1.1.3 Materials used in layer construction

The LbL assembly process controls the thickness of the layers in the Bragg stack by varying the number of cation/anion bilayer deposition cycles within each layer. At the same time the refractive index of the alternating layers needs to be controlled to establish the multilayers and achieve Bragg reflection. The alternating high (A) and low (B) refractive index layers are controlled in two ways: Firstly, materials with varying refractive indices can be used and combined in appropriate proportions. Secondly, as has been done here, materials with varying morphologies can be used to produce either denser or very porous structures. Porous structures will have an average RI between the material used and that of air. The asymmetry of the CNC morphology is an additional advantage. The rod-shaped particles have an aspect ratio of ~15 which can be utilised to produce highly porous assemblies when combined with spherical particles (colloidal silica spheres in this case). The porous structure created by a rod sphere combination will result in air pockets as a result of poor packing. The air pockets will lower the average refractive index of the overall layer thus further increasing the RI disparity between the high and low RI layers[227]. The effective refractive index (n_{eff}) can be found from the equation

$$n_{\text{eff}} = n_{\text{CNC}} f_{\text{CNC}} + n_{\text{SiO}} f_{\text{SiO}} + n_{\text{air}}(1 - [f_{\text{CNC}} + f_{\text{SiO}}]) \quad (39)$$

where n_{air} and n_{CNC} and n_{SiO} are refractive indices of air, CNCs and silicon oxide and f_{CNC}, f_{SiO} are the volume fractions occupied by the respective materials. CNCs were combined

with cationic colloidal silica to create a porous structure that makeup the low RI layer (Layer B in Table 5.1). The high refractive index layers (layer A in Table 5.1) were created using materials commonly used in LbL assembly and with morphologies suitable for more effective packing to achieve the opposite effect desired for Layer B. The two materials used were polyethylenimine (PEI), a cationic polymer and anionic vermiculate (VMT) clay 2D platelets. Electrostatic bonding between PEI and the flat face of VMT platelets encourages the high aspect ratio disks to align parallel to the substrate forming dense sheeted layers. The specific concentrations and pH of the solutions prepared are presented in Table 5.1.

Table 5.1 A and B layer materials, solution concentration and pH.

Layer	Sublayer Materials	Concentration (%)	pH
A	PEI	0.1	10
	VMT	1	7
B	CNC	0.1	7
	SiO_2	1	4

Assembly of the materials was as follows; the cationic solutions were prepared by adding 0.1 wt% of branched polyethylenimine (PEI) (Sigma Aldrich) (Mw ~ 25,000 g mol^{-1}), or 1 wt% of colloidal silica (SiO_2) (particle size 12$\pm$2 nm) (Ludox CL) (Sigma Aldrich) into deionized water. The pH of PEI and SiO_2 solutions were adjusted to 10 and 4, respectively, by adding 1.0 M hydrochloric acid (HCl). Anionic solutions were prepared using deionized water to make up a 1 wt% vermiculite (VMT) concentration (aspect ratio ~1100) (trade name Microlites 963++) (Specialty Vermiculite Corp.) solution and a 0.1 wt% CNC

solution. The CNC solution was adjusted to pH 7 using 0.1 M NaOH, and the VMT solution was set for 24 hours before use; the top supernatant part was used at its natural pH (~7.5). Single-side-polished (100) silicon wafers (University Wafer, South Boston, MA) were used as substrates for ellipsometry and scanning electron microscopy (SEM). Fused quartz slides (Structure Probe Inc., West Chester, PA) were used to measure the optical reflection from the films. Both silicon wafers and quartz slides were rinsed with deionized water and methanol before use, then plasma-treated with an ATT0 Plasma Cleaner (Thierry Corp., Royal Oak, MI). Plasma treatment improves adhesion of the first polyelectrolyte layer by oxidizing the substrate surface[24]. The substrate was first dipped into the PEI solution for 5 minutes, followed by rinsing with deionised water for 30 seconds and drying with a stream of filtered air. After the first positively-charged layer was adsorbed, the substrate was dipped into VMT solution for another 5 minutes, followed by another rinsing and drying cycle. Starting from the second bilayer deposition, the remaining layers were deposited using one-minute dip times. This process was undertaken using home-built robotic systems at Texas A&M University. After depositing the required number of PEI/VMT bilayers, the solutions were replaced with SiO_2 and CNCs and dipping continued until the required number of bilayers had been deposited. Two Bragg stacks with alternating A and B layers were prepared, one to reflect in the green region of the visible spectrum and another to reflect in the orange region of the visible spectrum. For simplification, the Bragg stack films will be referred to as either the green reflecting Bragg stack or the orange reflecting Bragg stack. The LbL setup is shown in Figure 5-2(a) and follows the method Iler *et al.*[188] described in Chapter 4, where a solid substrate is alternately dipped into well characterised organic solutions.

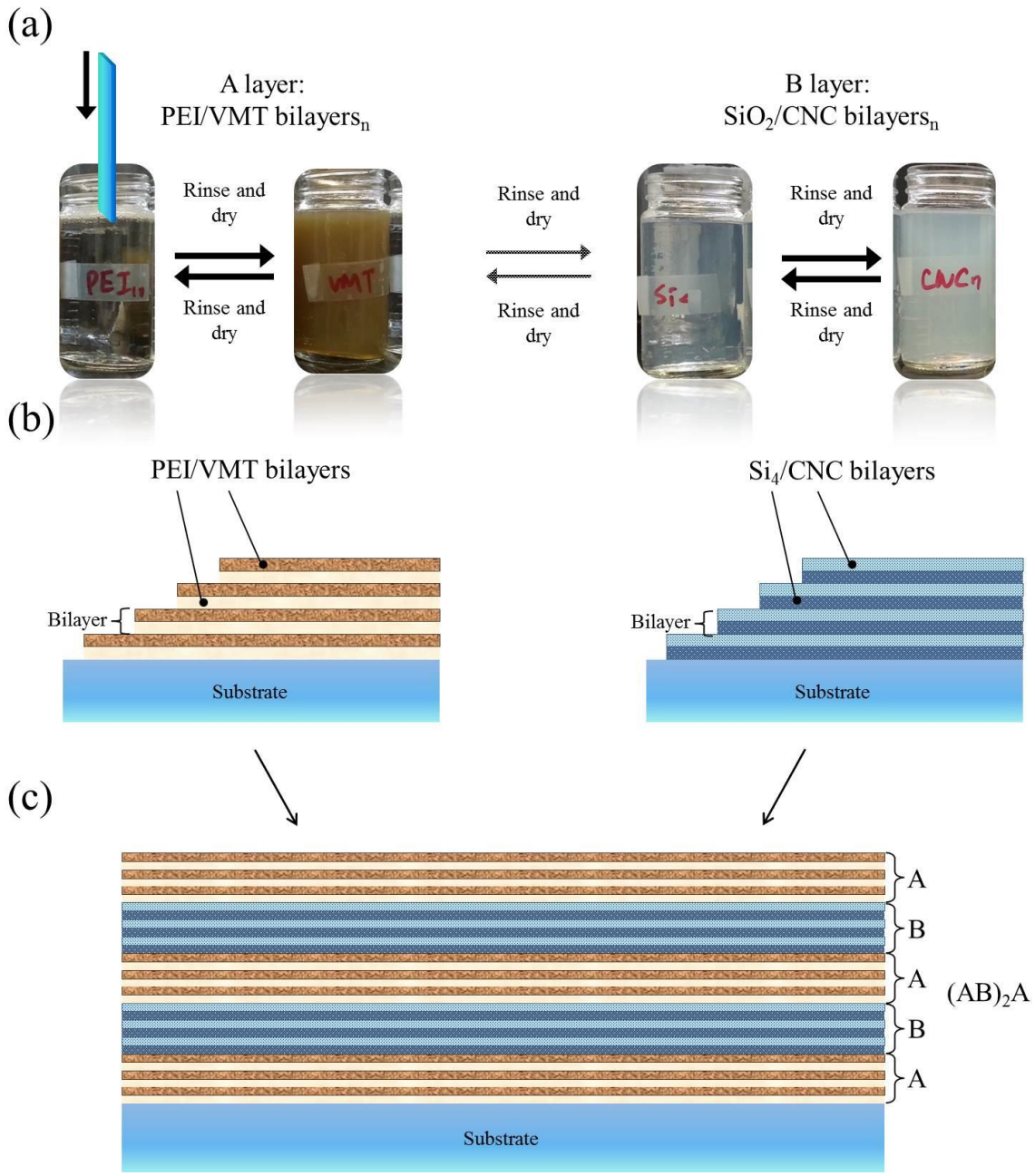

Figure 5-2 Illustrations of the LbL setup (a) wherein bilayers are applied by alternate dipping until the desired thickness for either A or B is reached and bilayer profiles (b) of A and B layers which together form the final Bragg stack (c).

Schematics of the A and B layer cross sections in Figure 5-2(b) show the bilayer configuration brought about by alternate dipping. Once a given thickness is reached for layer A, dipping will then proceed in the two solutions used to build up the B layer creating a stack of A and B layers as shown in Figure 5-2(c). The number of bilayers used in each A and B layer will determine the overall thickness. The number of A and B layers, which in the Figure is denoted $(AB)_2A$ (Figure 5-2c), will determine the thickness of the overall stack which will begin and end with an A layer. The growth profile data was used to model systems that would give narrow band reflection of visible light. The calculations were performed using transfer matrices, where various thicknesses and RI values taken from the growth profiles revealed combinations for stacks that would lead to bright reflectance in the visible region. Two systems were chosen to generate stacks that would reflect green and orange light and also mimic those displayed by the *C. rajah* beetle.

5.1.2 EISA thin films

5.1.2.1 Casting

A 6 wt.% aqueous solution of CNCs was obtained from FP Innovations. The CNCs have a sulphur content of 0.7-0.8% of the CNC mass and NaOH counter ions were used in their synthesis. Aqueous CNC droplets, 10 µl in volume, were deposited on to glass slides and immediately weighed. The droplets were left to dry at ambient temperature and pressure. The mass of the films was calculated as 6% of the droplet weight. The mass value was used to calculate the theoretical volume of a given film. The drop volume of 10 µl produced thin films of a suitable size (between 4-6 mm) so as to be practical to

characterise, particularly where profilometry was concerned as larger drops introduce greater measurement errors. TEM samples of film cross-sections were prepared using the common solvent exchange method which was successfully applied to CNC thin films by Giasson[228].

5.2.3 Calculating CNC Mass Distribution

The distribution of CNC mass was calculated as a relative concentration value using spectroscopic measurements of reflection and transmission (Figure 5-3) to calculate absorption. These measurements were taken using the MSP setup described in Section 5.3.2 where the micrometer stage was used to position neighbouring points across a given film diameter. Calculations of the nanocrystal distribution required knowledge of the volume of the section of film under investigation and the mass of solid material within the section.

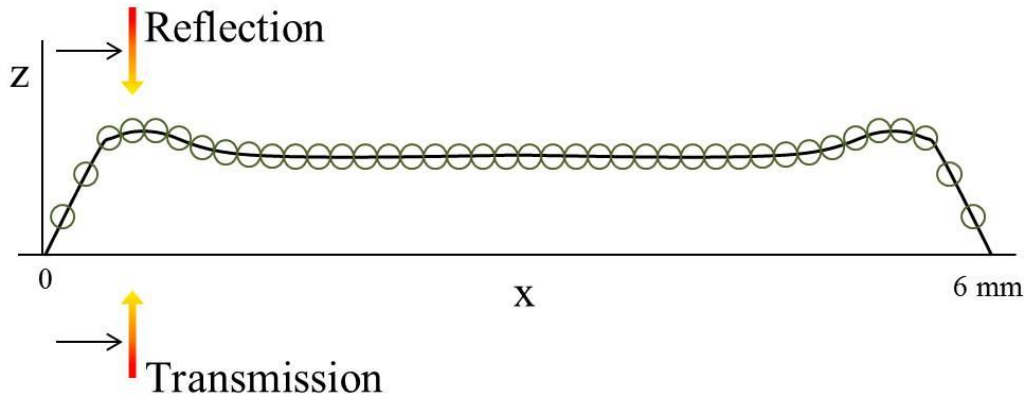

Figure 5-3 Schematic of a cross sectional profile (in height Z) of a CNC film along which reflection and transmission data are recorded using MSP from neighbouring points along x.

While it was not possible to measure mass directly, it was calculated using measured film volumes, the mass of the droplet and the assumption that within a given volume fraction (V_f) there will be a proportional mass fraction (m_f). This assumption is based on an equal rate of evaporation of solvent from around the hemispherical edge of the cast droplet resulting in an even radial distribution of the CNC solute material, hence $V_f \propto m_f$. Once the mass was known, for a given volume of the film, the distribution of that mass with that section of film could be determined spectroscopically. MSP was used to record transmission and reflection spectra from which absorbance (A) could be calculated using the equation

$$1 - (R + T) = A \tag{40}$$

where R and T are the fractions of reflected and transmitted light respectively. Spectra were taken from neighbouring points along the diameter of the film where profilometry data had been previously recorded. This was done so that an average height could be used to calculate the volume from which spectra were recorded, the total volume fraction being proportional to the mass fraction. From these calculations and experimental data, the distribution of CNCs across the diameter of a film can be determined and then used to identify relationships between CNC distribution and the reflection of circularly polarised and unpolarised light.

5.2 Structural Characterisation

5.2.1 Profilometry

Profilometry was used to map 2D cross-sectional profiles of EISA thin films, which were then used to calculate film volumes. Profilometers move a stylus across the surface of a sample and quantitatively measures the change in step height of the stylus as it follows the sample's profile (Figure 5-4a). The changing position of the stylus deflects the laser into a photodiode detector. The deflections are translated into a 2D topographical profiles (Figure 5-4b). Scan lengths can be up to 30 mm and stylus step heights are ~1.2 mm.

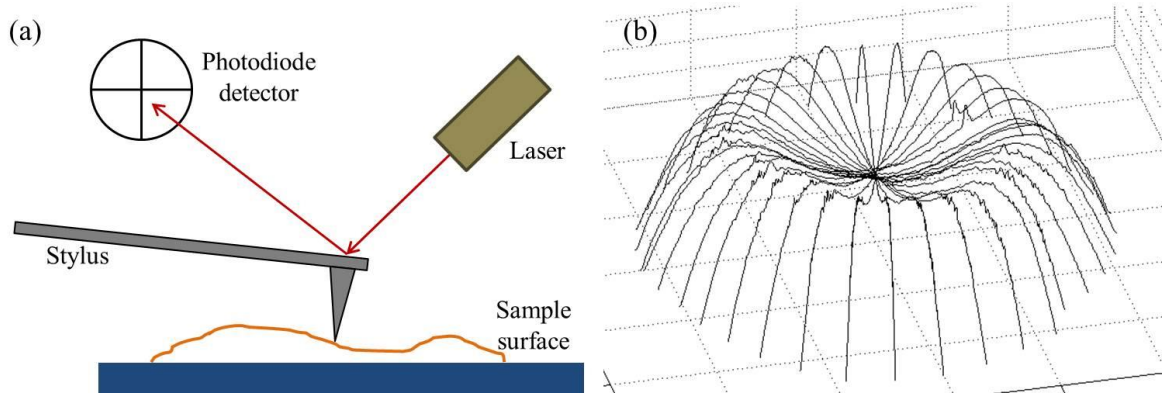

Figure 5-4 Schematics of the profilometer (a) and the compiled 2D film profiles generated by the profilometer (b).

The volume of the film was calculated by first measuring the cross-sectional profiles of solid films using a D100 Alpha step profiler. Profiles were recorded using the stylus arc movement in 'step up' mode with a low stylus force to avoid damaging the samples. The stylus has a 2 μm radius tip. Profilometry measurements were used to obtain multiple

cross-sectional profiles for a given film. The area beneath each cross-sectional profile was calculated using the trapezoidal integration method. Figure 5-3(b) illustrates the how the profiles were compiled. The equation

$$V_{\mathrm{f}} = \sum_{i} \frac{A_i}{2}\left(\frac{\theta}{360}\pi r\right) \tag{41}$$

was used to calculate the volume (V_{f}) of the film, where r is the radius of the drop profile section, A is the area of the profile cross section and θ which is the angle between neighbouring profile sections. For a comparison the volume was calculated again, but this time using a single averaged area according to the equation

$$V = A_{\mathrm{av.}}\pi r. \tag{42}$$

To determine the accuracy of film measurements, theoretical volume calculations were performed. These calculations were based on the mass of CNCs being 6% of the weight of the cast droplet and the individual CNC dimensions. These values made it possible to calculate the volume (V_{CNC}) and mass (m_{CNC}) of a single nanocrystal which were then used to calculate the number (N) of CNCs in the final film (using a density of 1.5 g cm^{-3} for cellulose). The volume of an individual nanocrystal was then multiplied by the total number (N) of CNCs. The theoretical volume values were expected to be smaller than the measured values as the calculation assumes close packing, only accounting for the volume of each individual nanocrystal and not the space between neighbouring CNCs.

5.2.2 Scanning electron microscopy

The ability to resolve distances beyond the capability of the human eye depends on the wavelength of the medium used and the quality of the lenses guiding the medium. Once the wavelengths of light in an optical microscope become the limiting factor (~ 200 nm) a new medium is required to improve resolution. The de Brogile wavelengths of electrons are smaller than the wavelengths of light and enable a finer resolution of the finer elements in a given sample. Scanning electron microscopy (SEM) utilises the resolving power of electrons by accelerating and focusing them into a beam directed at a sample. The beam scans the surface of a sample and electron-sample interactions produce secondary electrons and back scattering of incident electrons. The interactions are detected and used to visualise the surface features of the sample. The typical resolution of a SEM is ~1-20 nm.

Fabricated Bragg stacks and EISA thin films were prepared for SEM investigation by simply scoring the underside of the substrate and then snapping the substrate and sample in two. This snapping method avoids the use of cutting implements which would damage the sample during the cutting process and impair the surfaces to be viewed. The broken fragments were mounted on SEM stubs coated with sticky carbon tape. Because cellulose is a dielectric material and cannot ground accumulated charge, the samples were coated with 5-10 nm of electrically conducting palladium. This coating minimises the build-up of charge on the surface of the sample. The SEM images presented in this thesis were taken using an FEI Nova 600 dual-beam (FIB-SEM) system. The SEM was typically setup to use a low voltage of 5 kV with a 98pA current ta working distance of ~5 mm.

5.2.3 Transmission electron Microscopy

Transmission electron Microscopy (TEM) is an analytical technique used for investigating the variation in constituent materials and ultrastructural properties of samples. The technique requires samples to be prepared in 50-100 nm thin sections which are subsequently placed in the path of an electron beam under vacuum. The interactions of electrons transmitted through a given sample are detected and are translated to changes in image contrast. TEM was used to visualise the synthesised and the CNCs obtained from FP Innovations and the ultrastructure of Bragg stack and EISA thin film cross sections.

CNC suspensions were used to prepare the TEM samples. The suspensions were diluted to form a 0.2 wt% solution. Two drops of the 0.2 wt% aqueous CNC suspensions were placed onto holey carbon film coated TEM copper grids. The filter paper beneath the copper grid drew the droplets away pulling the droplet containing CNCs down onto the grid surface. The grids were allowed to dry and then a drop of 2% uranyl acetate was placed on the grid and left for 20 seconds. The drop was then then wicked away with filter paper. The uranyl acetate provides a negative contrast necessary to distinguish CNCs in the TEM. The prepared grids were then placed into a JM-2100 LaB6 200 kV Transmission Electron Microscope fitted with an AMT XR80 digital camera (3926 × 2472 pixels). An accelerating voltage of 100 kV was used to avoid damaging the CNCs. Measurements of CNC dimensions (length and width) were taken from the TEM images using ImageJ software.

TEM cross sections of the fabricated Bragg stacks were prepared by embedding a fragment of the film prepared on a polyethylene substrate in resin. The resin block was then polished to prepare a face aligned parallel to and that would expose the Bragg stack film face so that when aligned with the microtome, film cross sections could be cut.

Preparation of the CNC film cross sections required a different approach because in water the cross sections would lose structural integrity as they began to dissolve. For ultrastructural analysis of EISA CNC thin films small fragments of the film were initially embedded in 2% agarose (in dH2O) gel blocks prior to dehydration in an ethanol gradient (30% to 100% ethanol in 10 min steps). The blocks were then gradually embedded in Spurr resin overnight and the resin polymerized at 60 °C. 70 nm ultrathin sections were collected on pioloform-coated 100 mesh copper grids (Agar Scientific, Stansted, Essex, UK) and were imaged using a JEOL JEM 1400 transmission electron microscope operated at 120 kV and a digital camera (Gatan ES1000W, Abingdon, Oxon, UK).

5.2.4 Polarised Optical Microscopy

The phase composition of the dry films was analysed using POM on a Nikon Optiphot2-pol polarised optical microscope fitted with a 530 nm full retardation plate and a Sony DXC-950P colour camera. Camera footage of a drying droplet was also recorded through the microscope using a Veho discovery VMS-004 USB microscope.

5.3 Optical characterisation

5.3.1 Angle resolved spectrophotometry

Angle resolved spectrophotometry (ARS) was used to measure the iridescence of the Bragg stacks and the angle dependence of the reflection of CPL from the EISA thin films. The goniometer setup, shown in Figure 5-5 shows two arms to which various filter configurations can be arranged. The arms move in a 2θ configuration around a point where

the sample under investigation is mounted. Optical fibres are used to illuminate the sample by delivering light from an Ocean Optics HPX 2000 high powered Xenon light source. The second optical fibre collects reflected light and delivers it to an Ocean Optics USB2000+ spectrometer detector.

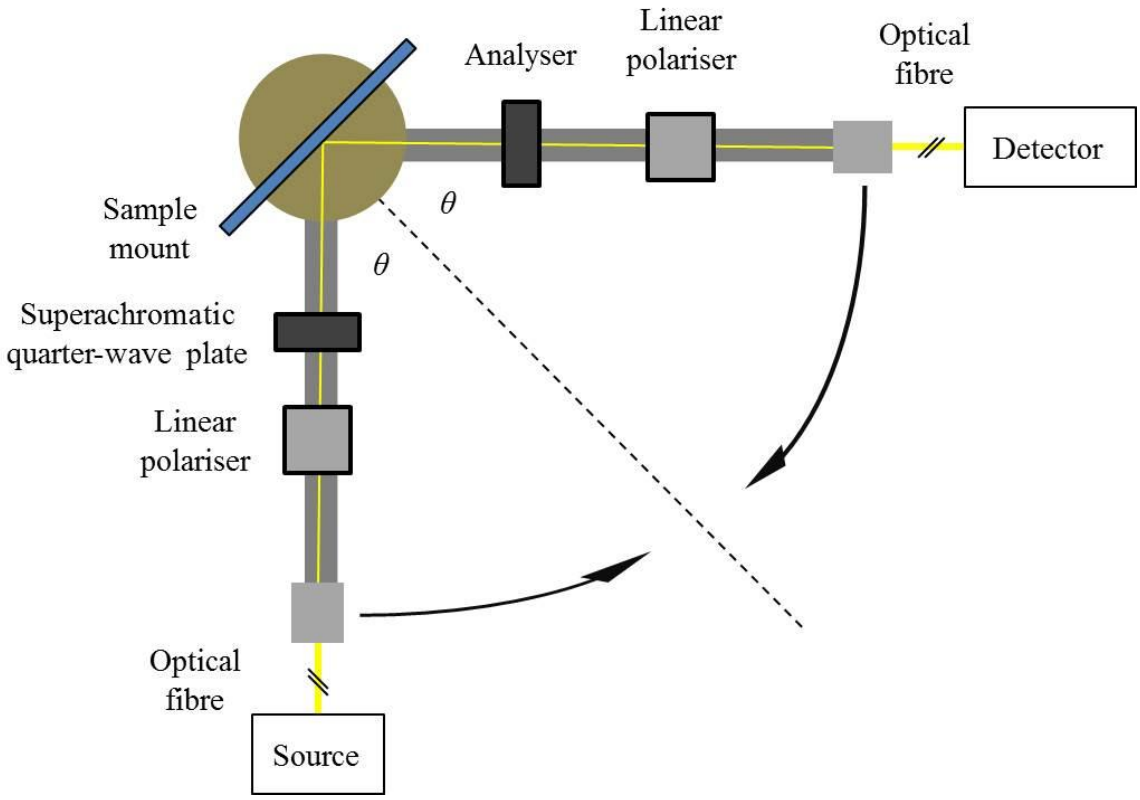

Figure 5-5 Schematic of the goniometer setup.

Iridescent behaviour of the Bragg stack films was analysed using the goniometer setup in Figure 5-5 where spectra was recorded through angles 5–70°. The Bragg stack films were illuminated with non-polarised light. To measure the angle dependence of the reflection of CPL from the EISA thin films the goniometer was fitted with Thor Labs superachromatic quarter-wave plates which were configured to illuminate and analyse the sample with CPL.

5.3.2 Microspectrophotometry

The reflection of unpolarised light and CPL from dried films was recorded using microspectrophotometry (MSP). MSP facilitates the characterisation of smaller regions of a given sample by combining optical fibres and spectrometers with the resolution of an optical microscope. This method allows investigators to isolate individual regions of colour for measurements, that from an otherwise larger region may express a mixture of colours. A GE Quartzline^{TM} projection lamp (Source 1/2 in Figure 5-6) illuminates the film and the lens/filter configuration direct reflected and transmitted light to an optical fibre positioned in the eye piece of the microscope. The optical fibre is connected to an Ocean optics USB2000+ spectrometer. Spectra are visualised in graphical format on a PC. The MSP setup allows circular polarising filters to be positioned in the microscope so that samples may be illuminated and analysed with CPL.

Calculating the CNC distribution in EISA thin films involved the need to collect reflection and transmission data from neighbouring points along the diameter of the film. This was achieved by mounting the samples onto a micrometer stage which was then fixed to the optical microscope stage. The film could then be moved in the *x*-*y* plane to within 2μm of a desired position.

Two optical characterisation techniques were employed to analyse the properties of the Bragg stack films. Optical data were obtained using angle resolved spectrophotometry (ARS) and microspectrophotometry (MSP). ARS is a goniometer arrangement where spectra are taken via a 2-θ setup.

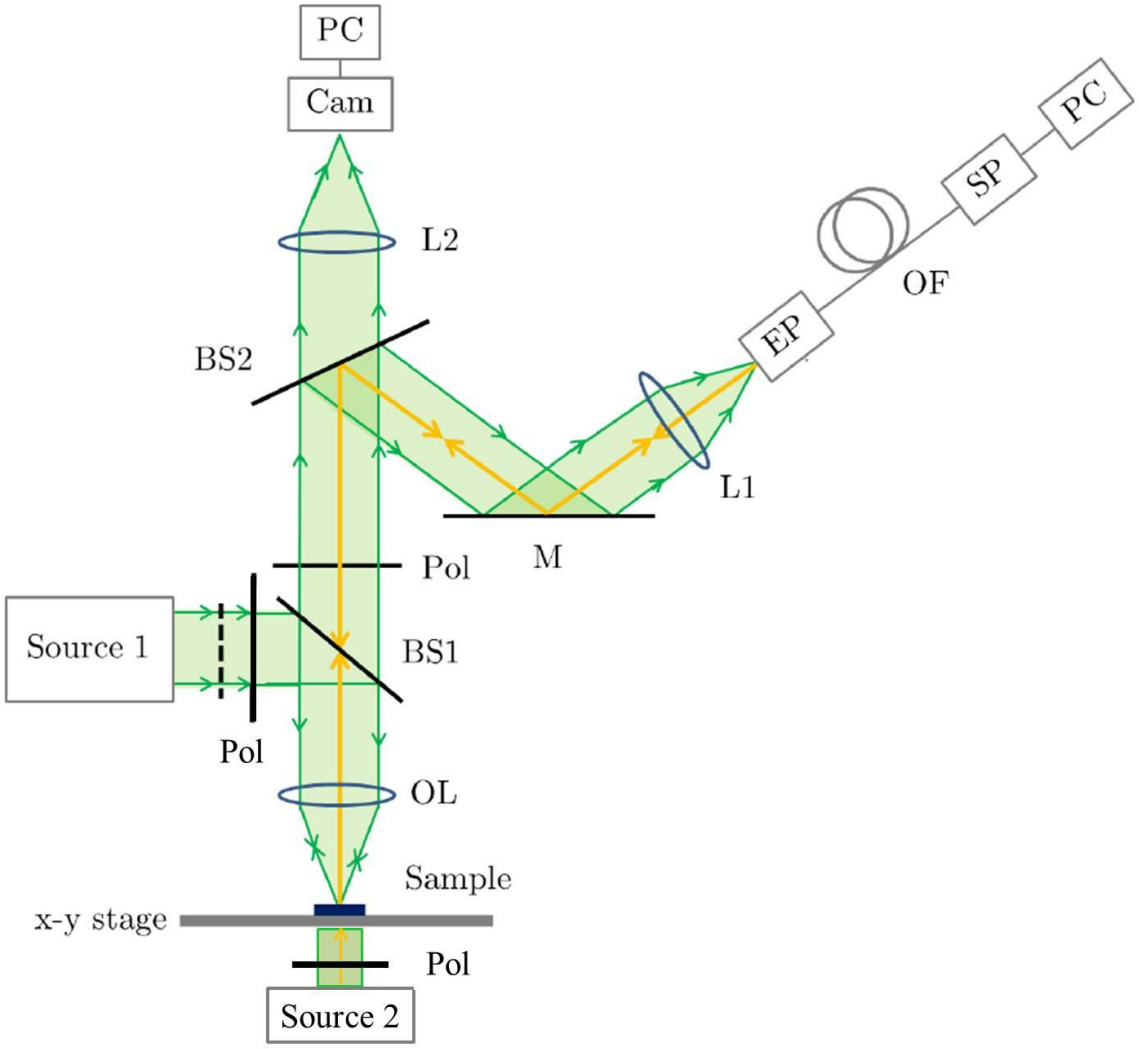

Figure 5-6 Schematic of the optical microscopy and MSP configuration. Light from Source one is reflected by the beam splitter BS1 down to the objective lens (OL; with magnifications between 5× and 100×) where it is focused on to the sample. Reflected light is passed back through the OL to another bean splitting mirror (BS2) where it is either directed to a camera connected to a personal computer (PC) or to the eye piece (EP) via a focusing lens (L1, L2). The EP can be connected to an optical fibre (OF) linked to a USB spectrometer (SP, PC). Light source 2 allows for a sample to be observed in transmission mode. Polarisers (Pol) can be inserted to illuminate/analyse samples with CPL in either reflection of transmission mode. M is a mirror.

5.3.3 Ellipsometry

Tuning the Bragg stack films to reflect a desired colour requires foreknowledge of layer thicknesses and RIs. Once these have been obtained the reflection of visible light from Bragg stacks with varying layer thicknesses can be modelled. Ellipsometry was used to measure both the bilayer thicknesses and the RI of varying numbers of bilayer stacks. Ellipsometry measures the phase shift in the polarisation of the reflected light from the sample under investigation. The measured values are expressed as Ψ and Δ which relate to the ratio of Fresnel reflection coefficients R_p and R_s for p- and s- polarised light, respectively

$$\rho = \frac{R_{\mathrm{p}}}{R_{\mathrm{s}}} = \tan(\psi)\, e^{i\Delta}. \tag{43}$$

The experimental setup is presented in Figure 5-7 and the instrument used was a J. A. Woollam WVASE ellipsometer. The ellipsometry layer thickness and RI results were used to generate growth profiles which assists the visualisation of the evolution of film thickness and refractive index as a function of the number of bilayers deposited in each bilayer stack.

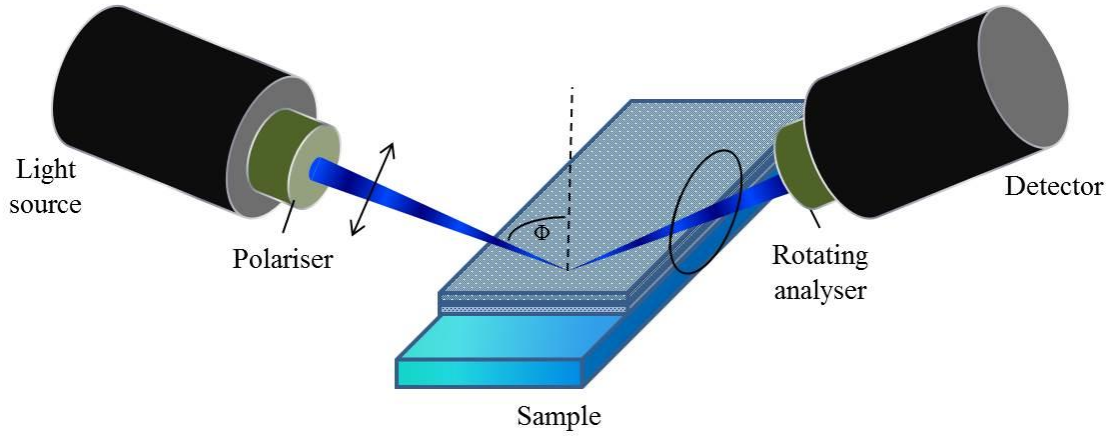

Figure 5-7. Schematic of the ellipsometer setup used to evaluate the bilayer thicknesses and refractive indices.

5.4 Theoretical modelling

5.4.1 Modelling the reflection of linear and circularly polarised light

Modelling the reflection of linear and circularly polarised light from the multilayered and chiral structures considered in this thesis can be achieved by one-dimensional matrix method calculations. The 3D multilayer and cholesteric structures have a RI variation in only one dimension and so can be simplified to a 1D problem for the purposes of modelling. The structural parameters, layer and pitch lengths, were measured from SEM and TEM images. These values were used in the computer programme to define the physical dimensions of the multilayer Bragg stack and the cholesteric structure. The other required parameter is the refractive index values which were obtained from the literature and ellipsometry data. Models of multilayer reflection of non-polarised light were solved using the transfer matrix method (TMM).[229] The models of reflection for CPL were solved

by applying Jones calculus to a CNC medium.[230] Pitch lengths (average of 308 nm with a standard deviation of 17.3 nm, Figure 7-10a), measured from TEM images in ImageJ[231], were discretised into thin sections and then piled so that the principle axes of the successive layers is turned through a small angle. Refractive indices (*n*) used for the birefringent CNCs were those of 1.595 and 1.534.[232] The coding was generated in house by I. Hooper and is based on the theory of reflection from multi-layered and chiral structures as described in Sections 2.2 and 2.3.2.

Chapter 6 Layer by Layer Bragg Stacks

The growth profile and modelling data inform the layer construction necessary to produce narrow band thin film Bragg reflectors. The following Chapter will outline the green and orange reflecting Bragg stacks made, the visual appearance of the films, their structure, morphology and iridescent behaviour. The films were made during a 3 week visit to the Polymer and Nanocomposites Lab at A&M University in Texas, USA. This Chapter will also include a comparison with a natural reflector found in the *C. rajah* beetle integument.

6.1 CNC morphology and layer growth profiles

The CNCs retained as a suspension were visualised using TEM. Images of the CNCs are shown in Figure 6-1(a,b) where their rod shaped morphology can be seen. The surface of the CNCs is not smooth but has fine ridges running along the long axis of the rod. The ends are also multi-faceted and shard like. The lengths and widths of the CNCs were measured and the results are presented in the histograms in Figure 6-1(c,d). The average

length and width of the CNCs was 178 nm × 12 nm with standard deviations of 79.3 nm and 4.6 nm respectively.

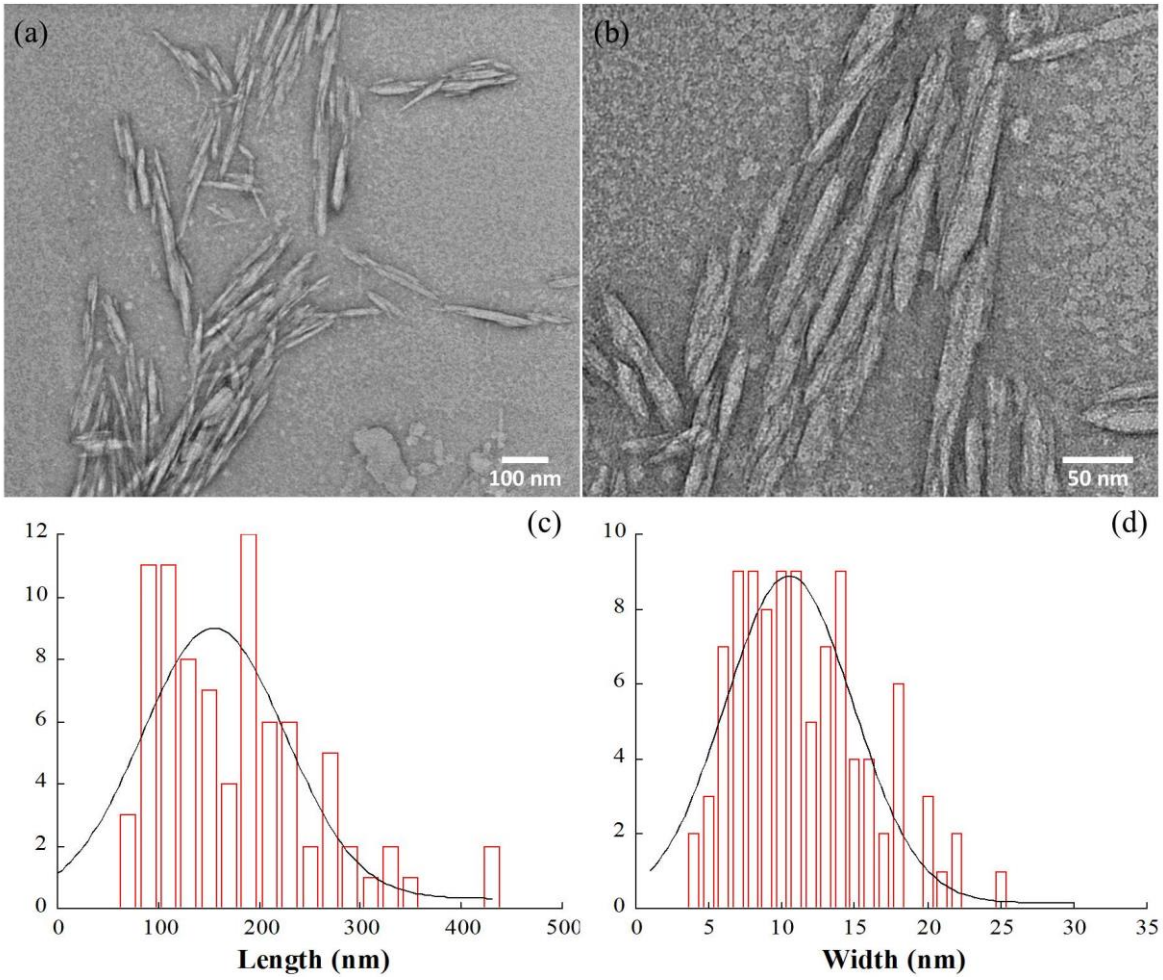

Figure 6-1 Typical transmission electron micrographs of CNCs. The lower magnification image (a) provides a wider field of view of CNC distribution on the copper grid and the higher magnification image (b) provides detail of CNC morphology. Size distribution plots of the length (c) and width (d) measurements, each with a Gaussian fit, taken using ImageJ software from TEM images. The average length and width dimensions were 178 nm × 12 nm.

The CNCs were observed to aggregate, rarely were individual CNCs observed. This is due to van de Waals forces and the high surface to volume ratio which results in particles of

this size possessing high surface energy. This made defining ends, for length measurements particularly, very difficult. The larger CNCs observed may be in fact be two smaller CNCs aligned parallel to each other. The close proximity of CNCs means that it becomes harder to distinguish between them.

The charge density was measured by conductometric titration and the CNCs have a sulphate-ester charge density of 37 ± 2.6 mmol/kg. This value sits at the higher end of values from literature that range from 24-38 mmol/kg[226,233,234].

The films, outlined in Table 6.1, were assembled using the LbL dipping method via a robotic system using a 1-minute dipping time. The very first solution dipped into, which was the PEI solution, was held for 5 minutes followed by 1-minute immersion times. Before the A and B layers were combined, A and B bilayers were assembled and their layer thicknesses and refractive indices were measured using ellipsometry. The ellipsometry results subsequently informed the assembly of the complete Bragg stack with AB layering.

Measurements taken using ellipsometry were used to generate growth profiles of the high (A) and low (B) refractive index layers. The growth profiles are shown in Figure 6-2. This information is given for both PEI/VMT and SiO_2/CNCs, Figure 6-2(a and b) respectively. Both systems exhibit linear growth, which is typical for bilayers containing nanoparticles[24,29,197]. The relationship between the number of bilayers and RI was not linear and evolves differently in each case. The RI of the PEI/VMT bilayers shows greater consistency after the build-up of 10 bilayers, after which the RI ranges from 1.65-1.66. SiO_2/CNCs show a gradual decrease in RI with increasing bilayer number before levelling out from 20 to 60 bilayers. Values of RI range from 1.4-1.42. It is in these bilayer ranges

(above 10 bilayers for PEI/VMT and above 20 bilayers for SiO_2/CNCs) where consistent Bragg stripes can be deposited.

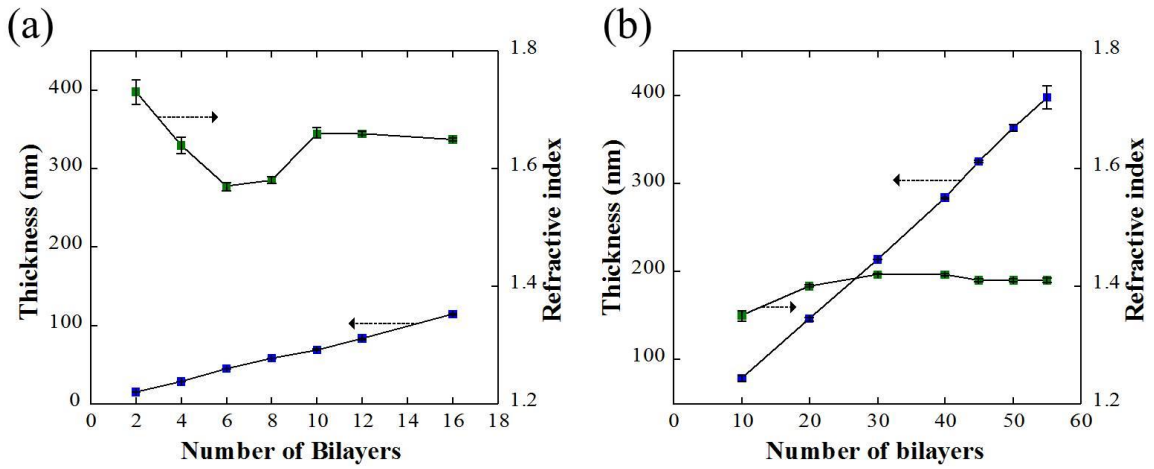

Figure 6-2. Thickness and refractive index as a function of bilayer number for PEI/VMT (a) and SiO_2/CNC (b) layers.

6.2 Modelled optical behaviour

The required parameters for the A and B layers of the green stack and the orange stack are shown in Table 6.1. The modelled reflectance generated using TTM for the green film occurs in a narrow band which peaks at 559 nm at normal incidence as shown in Figure 6-3(a). The peak reflectance blue-shifts (to ~410 nm) with increasing incident angle which is a common hallmark of iridescence and is where the hue is observed to change with varying viewing angle. Figure 6-3(b) highlights this characteristic iridescent reflectance of unpolarised light for the green reflecting Bragg stack.

Table 6.1 A and B layer parameters for a green and an orange reflecting multilayer

Colour	Layer	Refractive index	Thickness (nm)	Number of bilayers
Green	A	1.65	115	16
	B	1.41	230	32
Orange	A	1.65	105	15
	B	1.38	110	15

A blue-shifting peak initially located at 559 nm is clearly seen with increasing incident angle. The reflectance from the theoretical AB layer thicknesses and RIs for 1, 2, 5 and 24 layers is presented in Figure 6-3(c) and for many more layers in Figure 6-3(d). A rapid increase in reflectance intensity is observed with increasing layer number. The rate varies significantly between the first few bilayers and nearly doubles from 1 to 5 bilayers. The rate of the increasing peak intensity (R_{max}) reduces sharply once the number of bilayers is greater than 6. With the increasing reflectance intensity is a gradually decreasing bandwidth. There is also a 0-20% oscillation of reflectance in the background. This is due to the RI interlayer differences being much smaller than the difference of the RIs between air and the material which give rise to a thin film interference effect[235].

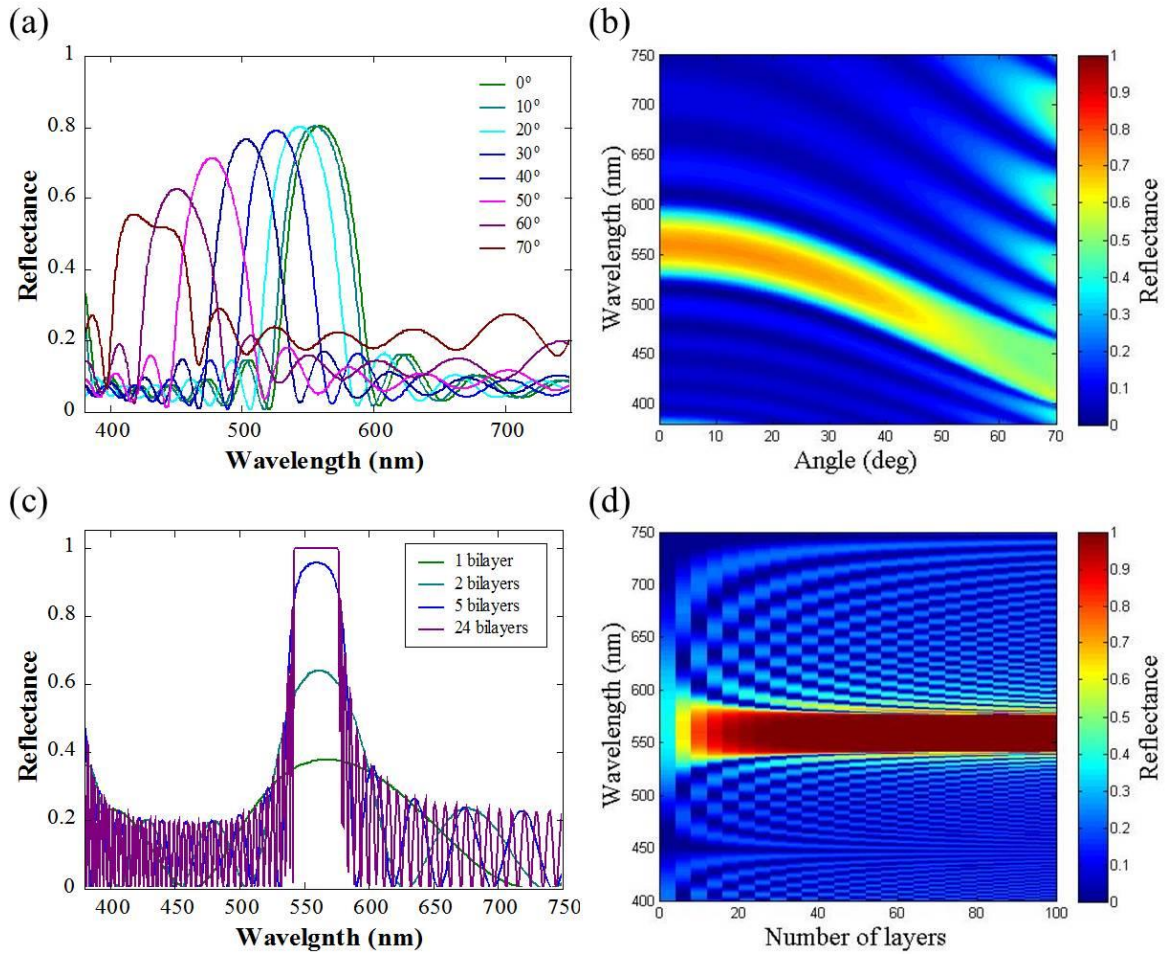

Figure 6-3 Numerical calculations of the optical behaviour of the green reflecting multilayer described in table 6.1 (a) Unpolarised reflectance for incident angles of 0-70 degrees. (b) Reflectance map showing the angle-dependence of unpolarised reflectance. (c) Normal incidence reflectance for 1, 2, 5 and 24 bilayers. (d) Reflectance map showing the numerical variation of normal incidence reflectance as a function of increasing bilayer number.

Beyond the 6th layer the addition of further material makes minimal difference to R_{max} until the 24th bilayer is added and the reflectance becomes completely saturated. It is at this point the structure is reflecting 100% of certain wavelengths (assuming no absorption) so no further increase in R_{max} will be observed. These reflected wavelengths that cannot propagate through the structure are a feature known as a photonic band gap. Another common feature of multilayers having small

RIs is that the bandwidth is inversely proportional to the number of layers; hence many layers are needed to produce a narrow bandwidth[235].

This modelling approach informed the fabrication process, providing a window of bilayer numbers which could produce significant reflectance. The theoretical reflectance results for the orange reflecting film are shown in Figure 6-4.

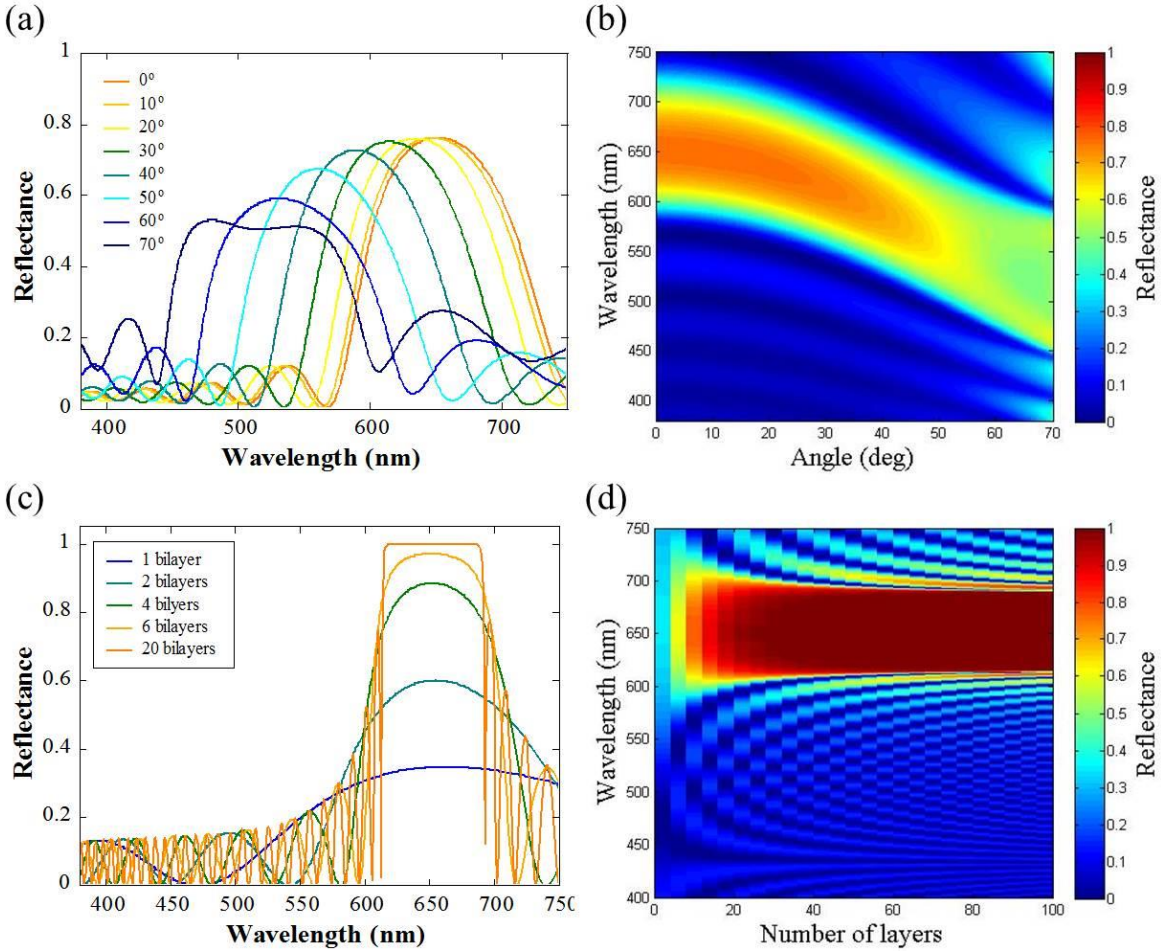

Figure 6-4 Numerical calculations of the optical behaviour of the orange reflecting multilayer described in Table 6.1 (a) Unpolarised reflectance for incident angles of 0-70°. (b) Reflectance map showing the angle-dependence of unpolarised reflectance. (c) Normal incidence reflectance for 1, 2, 4, 6 and 20 bilayers. (d) Reflectance map showing the theoretical variation of normal incidence reflectance as a function of increasing bilayer number.

Peak reflectance occurs at a wavelength of 652 nm (Figure 6-4a), across a broader band than that of the modelled green system, and exhibits similar iridescent behaviour (Figure 6-4a-b) which is again seen as a characteristic blue-shift with increasing incident angle. A similar increase in reflectance to the green reflecting film is observed with an increasing bilayer number which proceeds to saturation beyond 20 bilayers (Figure 6-4c-d). An additional tool was developed to compile reflectance results for varying AB thicknesses and their respective RIs. The chart produced presents the colour as it would appear to the naked eye for specific layer thickness/RI combinations (Figure 6-5).

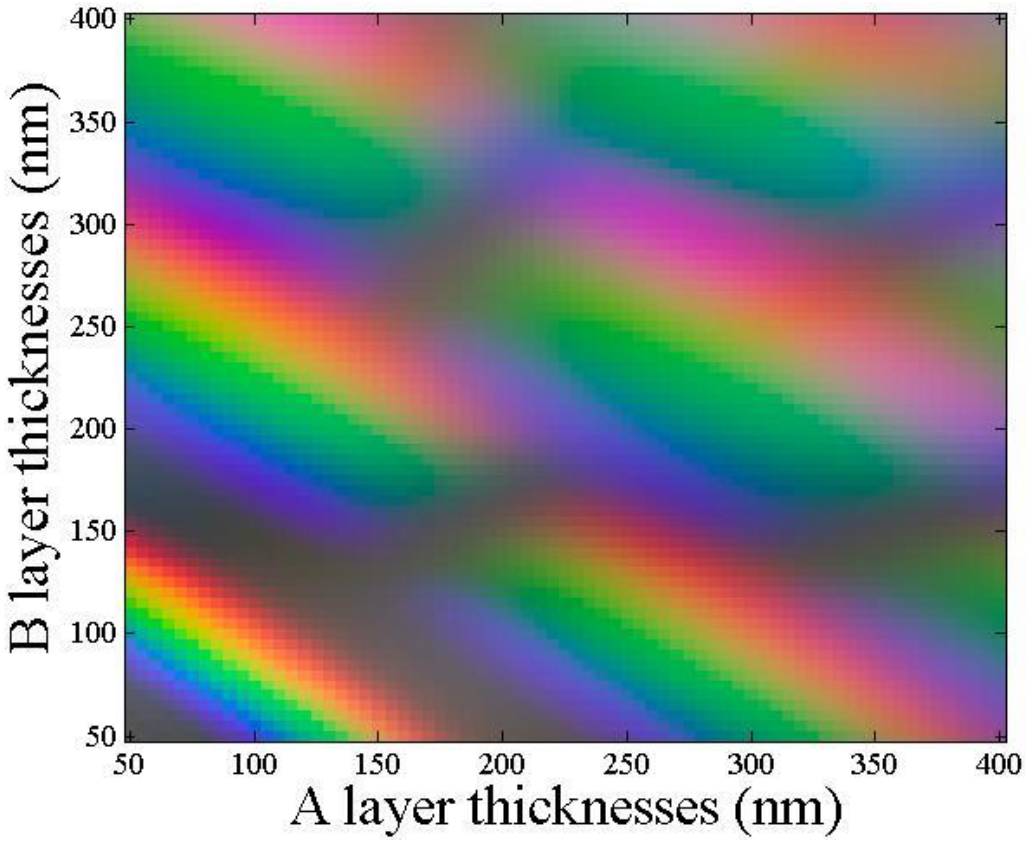

Figure 6-5 Colour map showing RGB values for varying AB thicknesses and respective RIs.

This was achieved by first calculating the reflectance for each thickness/RI combination and then calculating their respective RGB values (as explained in Section 2.4). The corresponding RGB colour is then plotted as a function of the A and B thicknesses. The colour map in Figure 6-5 highlights the ability of specific thickness combinations to generate coherent reflection in the visible range. The clear colour bands in the bottom left hand corner represent those reflected from layer thickness combinations that produce systems with reflectance corresponding to saturated colour. The regions where the thickness would need to be above either 220 nm for the A layer or 200 nm for the B layer represent systems with reflectance corresponding to less saturated colour. Films with thickness combinations in the region where colour is more saturated are more susceptible to defects which would cause the reflection of multiple colours and result in broad band reflection corresponding to a less saturated colour. A plot like Figure 6-5 can be generated to inform the synthesis of new Bragg stacks as it identifies which Bragg sack systems are less susceptible to defects if colour saturation is not an issue. Where colour saturation is important the plot can be used to identify a system that would produce good colour saturation. Care would have to be taken to ensure defects are kept to a minimum.

6.3 Bragg Stack Appearance and Morphology

The Bragg stacks were prepared with varying $(AB)_nA$ combinations and images of the films are presented in Figure 6-6 (a,b). Each stack combination is separated by a tide mark that runs horizontally across the film. The tide marks are apparent on both films and are created by the small differences in height between solutions into which they have been

dipped during the assembly process. Lower colour reflectance around the edges of the film is a result of water run off during the washing and drying process. Air blown onto the film pushes the water outwards and downwards, thereby increasing the area of lower colour reflectance down the film. The LbL-assembled film is flat, so iridescence is not discernible until it is tilted. On a macroscopic scale the green and orange colours appear homogenous, a result of the flat substrate and the even layer deposition of the LbL process. If the layer thicknesses varied during fabrication, a broader reflection band would result and appear less optically saturated[30]. The orange film appears less saturated than expect. The layer thickness combination of this film would place reflectance from the bottom left hand corner of the colour map in Figure 6-5. The reasons for this become apparent upon magnification of the film surface. With increasing magnification, a separation of colour was observed and is a result of variation in film height. This was true for both films but more so in the orange film which was less saturated. The microscope images in Figure 6-6 show each film surface imaged under increasing magnification. The green film (Figure 6-6a) displays greater homogeneity at a lower magnification. The separation of colours becomes visible at a higher magnification where green and blue patches appear due to varying film thickness. The colour separation has little effect on the position of the peak shown in the reflection curves presented below the images in Figure 6-6. Magnification of the orange film surface revealed clear colour separation interspersed with evenly spaced streaks 150-200 μm long and 10-20 μm across. At low magnification the streaks appear yellow with the overall film producing broad band reflection with a broad peak at approximately 640 nm. Increasing the magnification revealed a broader spectrum of colour across the streaks which blue-shift towards the centre.

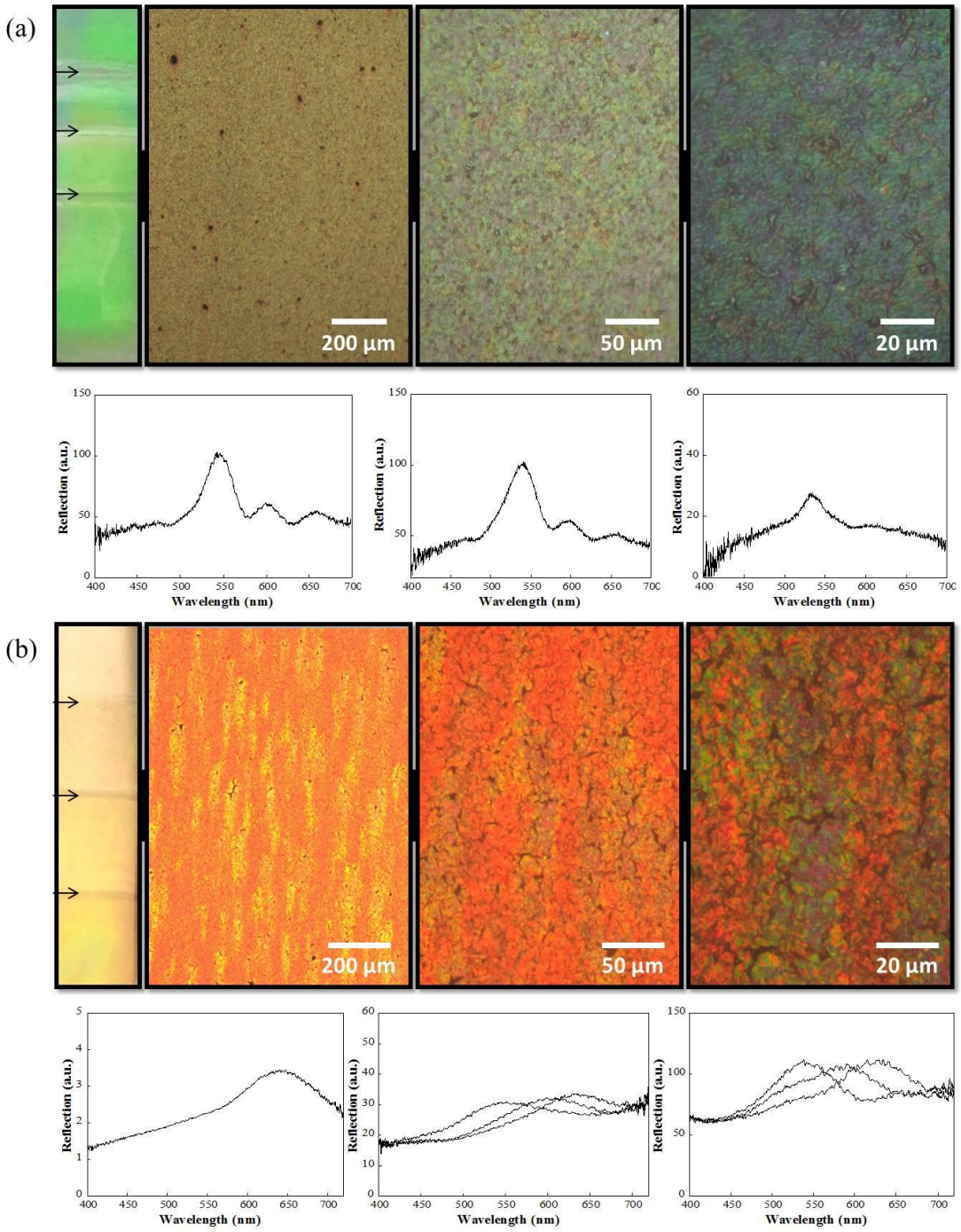

Figure 6-6 Images of the green (a) and the orange (b) reflecting film with microscope images showing the variations in the surface morphology and colouration as a function of scale (with magnification increasing from left to right) and corresponding MSP spectra. Each magnified image corresponds to the MSP spectra below it. The MSP spectra show reflectance from each surface shown in the images. In (b) multiple reflectance curves are presented as they correspond to the different coloured regions seen in the image. The black arrows highlight the tide marks.

Corresponding peaks in the reflection curves were obtained and together are responsible for the broad band reflection on the macro scale. These features are most likely a result of particles (inclusions) interfering with the flow of water during the rinsing and drying steps. Particles/defects can be seen at the top of each streak which then taper toward the bottom and align with the direction of the water and air used in the washing phase.

In addition to the variability observed in the orange film is the variability observed in films made during initial tests. The variability was caused by the process itself, whereby water running down the substrate damaged the film. The damage occurred towards the edge of the film, perhaps where most of the water was pushed during the washing and drying stages. This effect is seen in the photograph in Figure 6-7(left). The colouration on left hand side towards the bottom of the film has diminished and appears dull. Reflection data was recorded using MSP from 5 points across each of the films. The points are highlighted by the yellow spots in the photograph. The respective reflection curves are presented graphically on the right and a trend of increasing variability can be seen down the substrate. The $(AB)_3A$ film shows some variation but this could also be due to the tide marks above and below the narrow strip of film. Only a slight dip in reflection is seen at the very left-hand edge of the $(AB)_4A$. Larger variations in reflection are seen in films $(AB)_5A$ and $(AB)_6A$. In the $(AB)_5A$ film peak shifts and decreases in reflection are seen in data points 4 and 5. Data point 5 for the $(AB)_6A$ film shows a significant reduction in reflection and a broadening of the reflectance band altogether. The reason for the film damage on one side of the substrate could be due to the alignment of the substrate to the water and air blowers which results in more water being moved to that particular side of the substrate before running off. This can be accommodated for by having larger substrates or resolved by adjusting the alignment of the substrate with the washing hoses.

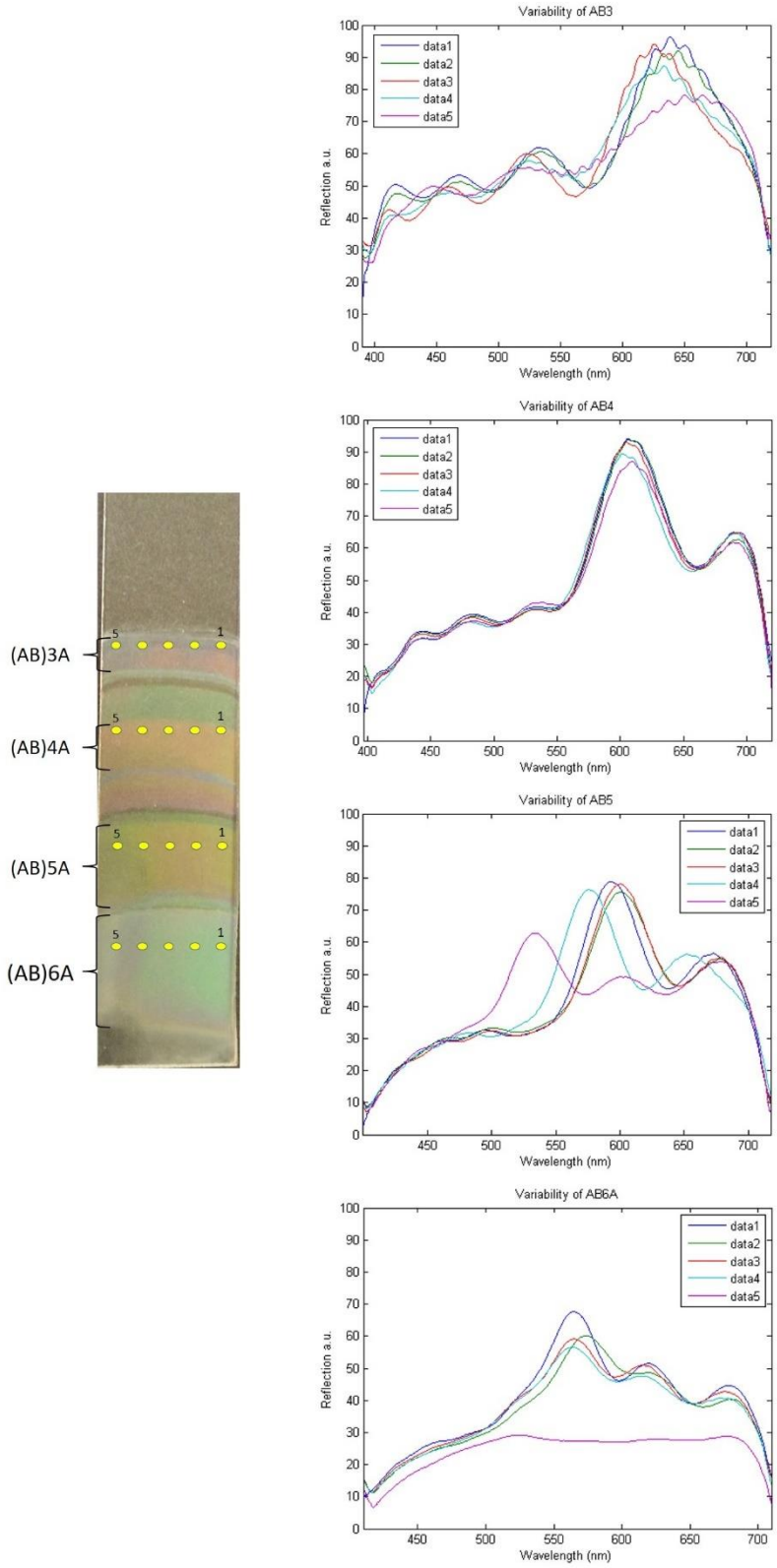

Figure 6-7 Photograph of a test sample showing varying numbers of bilayered films (left). Five data points are highlighted where reflection spectra were taken. The respective curves are presented in the graphs (right).

6.4 SEM and TEM Analysis

The structures of the stacks were characterised using SEM and TEM. Figure 6-8(a) shows an SEM image of a cross-section of the green film and confirms the desired dense laminar structure of the A layers where the VMT 2D platelets have formed stacked sheets held together by the electrostatic forces between the platelets and the PEI polymer. In contrast, the colloidal silica and CNC combination has formed an isotropic porous structure. These porous layers are seen in Figure 6-8(a) in between the denser PEI/VMT sheeted layers. This was one of the intentions of the fabrication process because such porosity generates a low effective RI for the B layers as explained in Section 5.1.1.

The TEM images presented in Figure 6-8(b) also show that the fabricated films comprise alternating light contrasted and dark contrasted layers. The darker layers represent the high RI A layers and the lighter layers the low RI B layers. Upon closer inspection of the A layer (Figure 6-8c), a distinguishable laminar arrangement of VMT (the darker lines) and PEI can be discerned. The curvature in the layers is understood to be a result of the microtoming process where sample sectioning and exposure to water may compromise the structural integrity of the film.

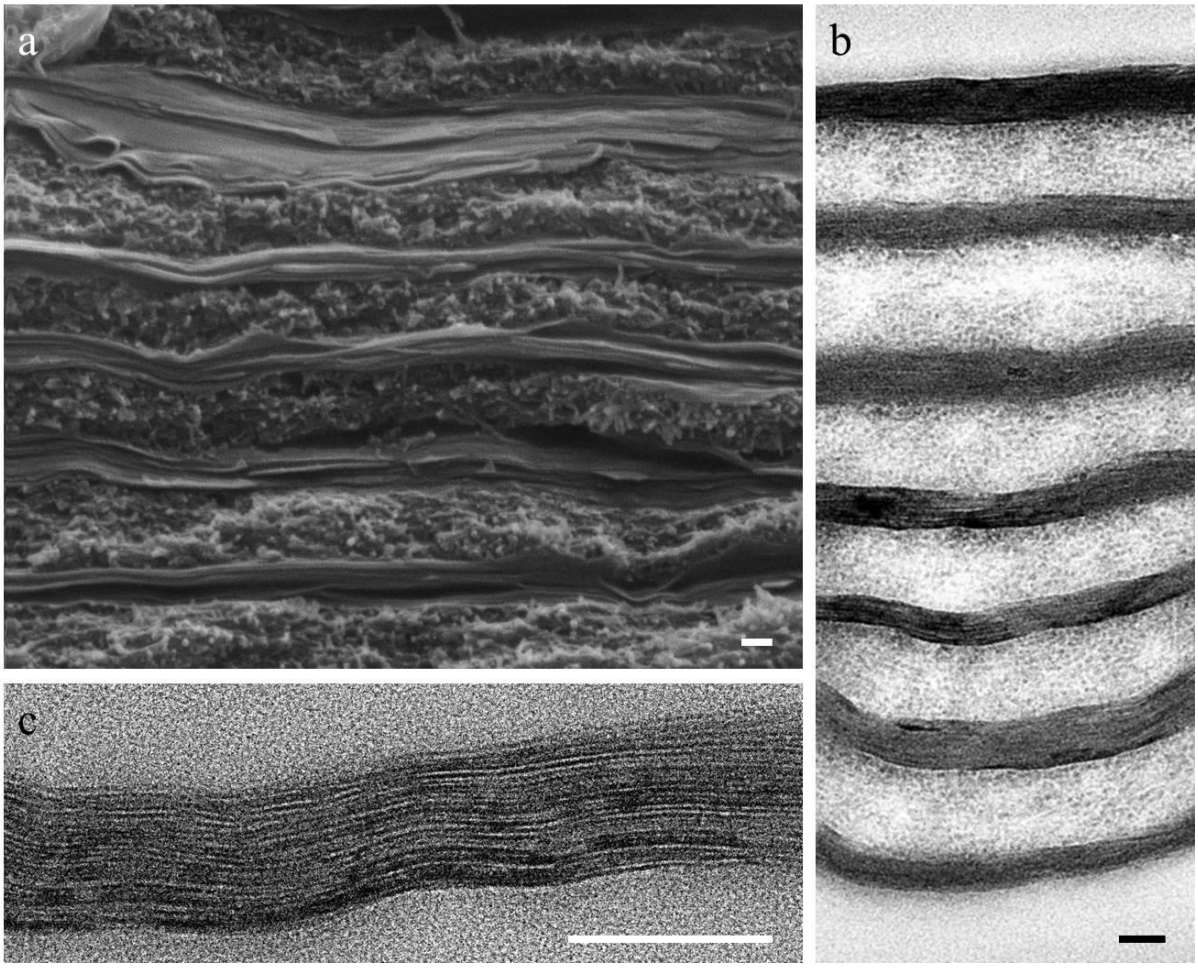

Figure 6-8 (a) SEM image of the green film cross-section. (b) TEM images of the orange film cross sections. (c) Magnified section of (b) highlighting the bilayer structure in the A layer. Scale bars are 100 nm.

6.5 Optical Characterisation

Reflectance of unpolarised light was collected from both the green and orange films using the ARS setup described in Section 5.3.1 and illustrated in Figure 5-5. The results for the green reflecting film at normal incidence show narrow band reflection with a peak

reflection at 558 nm (Figure 6-9a) which are in good agreement with the 559 nm peak reflection and side bands calculated numerically (Figure 6-9b). Side bands are also seen in the reflectance curves and are indicative of the homogeneity of the film. The peak reflectance blue-shifts with increasing incidence angle, this iridescent behaviour is more clearly shown in Figure 6-9(c) and is a close match to the numerically calculated reflectance for increasing incidence angle (Figure 6-9d). The overall match between the experimental and numerically calculated results is very good. The most obvious difference is that the reflection from the green film corresponds to a less saturated colour. This could be due to the small variations in layer thickness across the film. Evidence of this is seen in the SEM images in Figure 6-8a, and in the colour variation in the high magnification image shown in Figure 6-6a which is derived from variation in layer thicknesses.

The optical reflectance results from the orange film (Figure 6-9e,g) are in relatively good agreement with the numerically calculated reflectance (Figure 6-9f,h). The orange film, like the green film, has less saturated colour reflectance. The peak reflectance at normal incidence for the orange film and the numerically calculated system is also different, at 699 nm and 652 nm respectively. The system still expresses iridescent behaviour characteristic of multilayer Bragg stacks (Figure 6-9g) and a strong match is seen in the reflectance curves shown for varying incident angles.

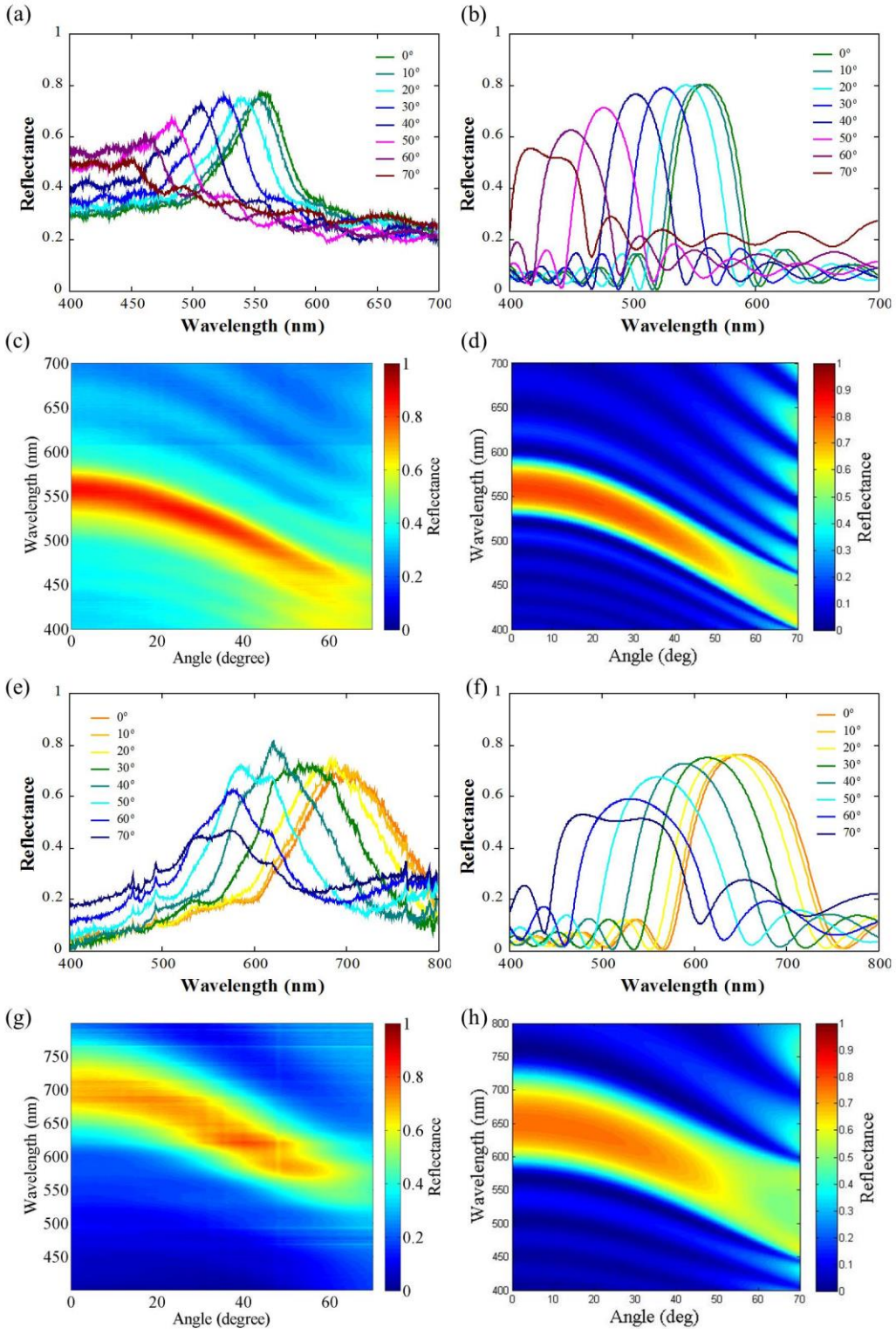

Figure 6-9 (a-d) Experimental and theoretical reflectance spectra from the green film and corresponding reflectance colour maps showing the angle-dependence of unpolarised reflectance. (e-h) Experimental and theoretical reflectance spectra from the orange film and corresponding reflectance colour maps showing the angle-dependence of unpolarised reflectance.

Evident in the experimental data are anomalies that are not as easily explained. These anomalies are seen in the spectral data taken from the fabricated films. An early double peak is seen in light reflected at 50˚ incidence. At 40˚ and 60˚ incidence the reflected spectral profiles show a shoulder on the right and left respectively of the main peaks. High saturation levels are seen in the reflection profiles of the green film. These anomalies are not seen in the modelled data.

6.6 Modelling the anomalies

Attempts were made to model variations in layer construction to intentionally produce such anomalies and understand what is causing them. Changes in reflection are most likely to occur due to variations in layer thicknesses and this is expected, to a certain degree, within fabricated films. Evidence of this variation is seen in the microscopy work presented in Figure 6-6 and Figure 6-8. The modelled anomalies therefore are based on variations in layer thicknesses which were selected from the colour-map presented in Figure 6-5. The results presented in Figure 6-10 highlight the changes in reflection profiles that maintain an intensity equivalent to those obtained in Figure 6-9(a and e). Other variations introduced to layer thicknesses produced reflection curves with significantly less intensity which would not contribute to the anomalies observed in the experimental data.

Initially small changes were introduced to simulate defects in layer consistencies. Variation was observed when small changes were made to one or two of the bilayers. By changing the A and B layers by up to 10 nm in two of the bilayers the peak reflectance bands could be shifted either to the left or to the right depending on whether the layer thicknesses were

increased or decreased (Figure 6-10a). Layer decreases shifted the peak to the left and increases shifted the peak to the right. Significant changes in the spectral profile were seen when broad variations were introduced to all either the B layers or the A layers (Figure 6-10b). This was done to simulate a chirped structure which is known to give broad band reflection and multiple peak maxima.

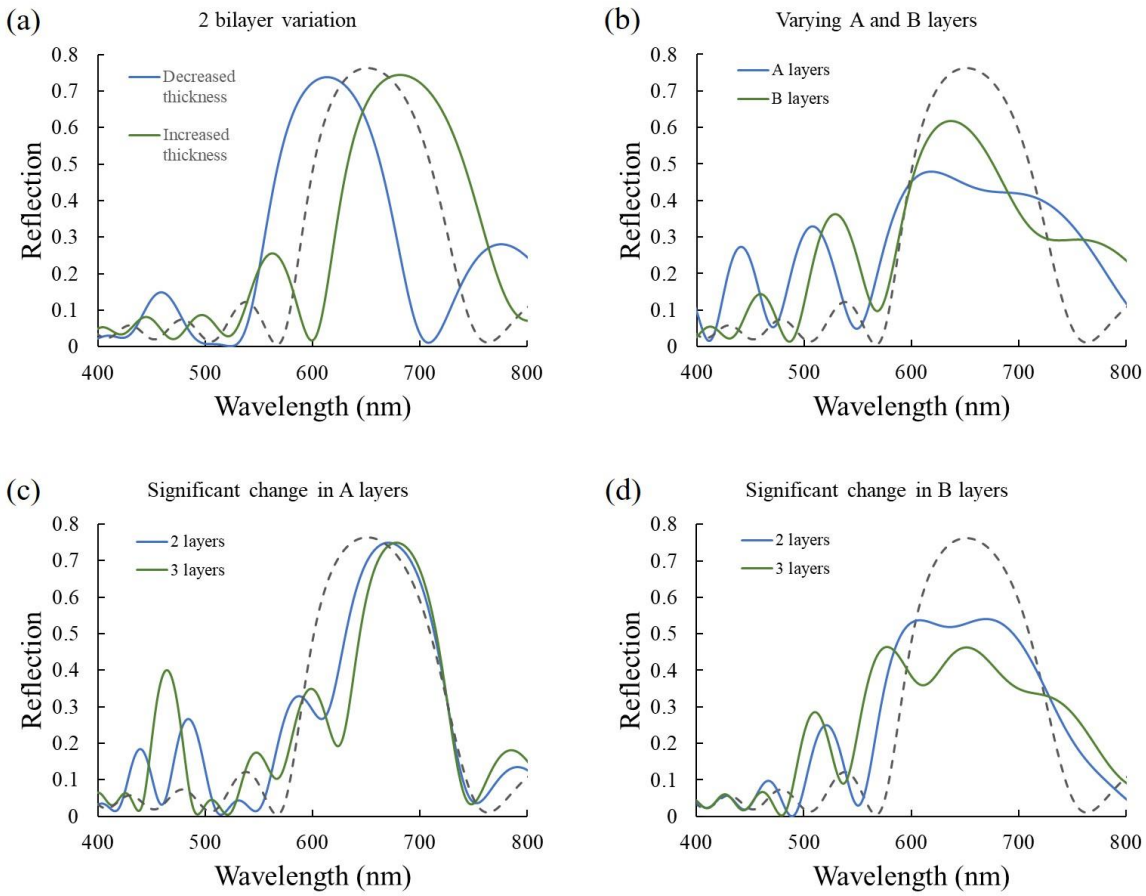

Figure 6-10 Modelled spectral reflection profiles for variations introduced to the orange film bilayers. (a) 10 nm increases and decreases in A and B layers in 2 of the 6 bilayers. (b) Variations made to every A and B layer in the stack ranging from 75-125 nm and 50-110 nm respectively in 10 nm intervals. (c) Significant increase to 325 nm to 2 and 3 of the A layers. (d) 2 and 3 of the B layers at 260 nm increase. The dashed line shows the modelled reflection at normal incidence from the original stack for reference.

By varying the thicknesses of the B layers, a shoulder was introduced to the right of the peak reflectance band. Increases were seen in the side bands when either the A or B layers were varied. Varying the A layers produced more significant changes with a broadening of the peak reflectance band and a shoulder to the right of this band close to becoming a second peak. When significant changes were introduced to 2 and 3 of the A layers in the stack (Figure 6-10c), the peak intensity was maintained and shifted to the right. A narrower peak reflectance band was produced with the addition of relatively high intensity side bands which simply became more pronounced as more layers were changed to the increased thickness. One variation that did result in a double peak reflectance band was the increase in thickness of B layers to 260 nm. This change in just 2 of the layers resulted in a spectral profile with two peaks as shown in Figure 6-10(d). Other changes in reflectance include peak broadening and higher intensity side bands. The double peaks are further developed with 3 altered layers with further peak broadening and increasing side band intensities. It is plausible that a combination of varying A and thicknesses responsible for the peak broadening and shoulders observed in the experimental data. It is however unlikely that significant increases in layer thicknesses are responsible for the early onset of the double peak as the evidence seen in the microscopy images shows only small variation in layer thicknesses.

The effect of incidence angle on the reflection profiles exhibiting the greatest change due to layer variations is presented in Figure 6-11. The reflection spectra are given for angles from 0-70˚ for the regime of varying A layer thicknesses (Figure 6-11a) and for the significant increase in 3 B layer thicknesses (Figure 6-11b). In each case a blue-shift is seen with increasing incidence angle and little is lost in the peak intensity.

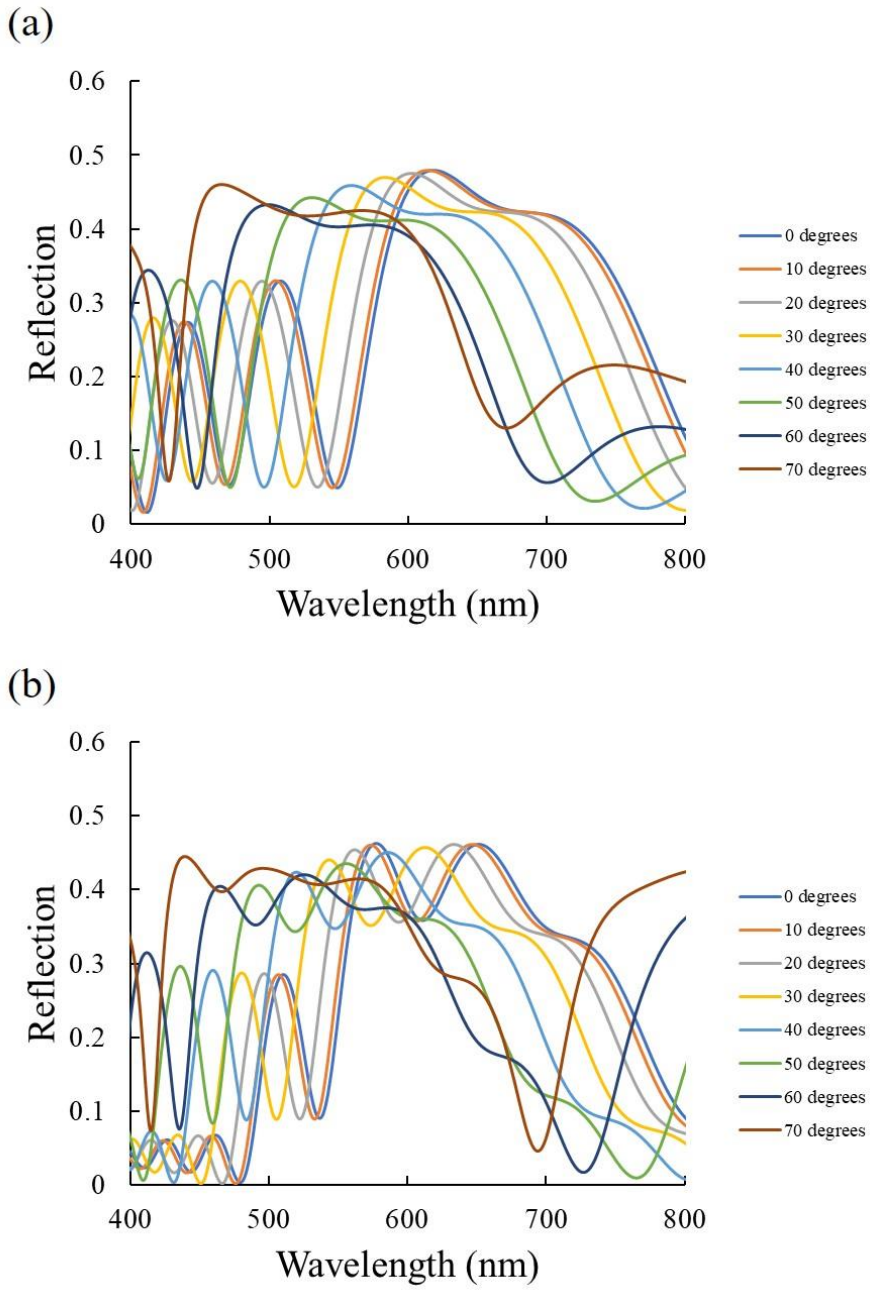

Figure 6-11 Effect of incidence angle on (a) variations made to A layers in the stack, ranging from 50-110 nm in 10 nm intervals and (b) significant increase to 260 nm of 3 B layers.

Both also undergo band broadening with increasing incidence angle. The loss of intensity in the experimental data occurs more slowly with increasing incidence angle like the loss seen here because of layer thickness variations. This also suggests that the periodicity is aligned parallel to the substrate as any crystalline periodicities aligned at an angle to the substrate will scatter light away from the detector and result in a more rapid loss in intensity with increasing incidence angle.

6.7 Natural Comparison

The appearance and structure of the stacks were characterised using TEM and compared to the layered system in the integument of a *C. rajah* beetle. Figure 6-12(a-c) shows photograph images of the *C. rajah* elytron and LbL-assembled green and orange Bragg stacks. The green and orangey-yellow colouration of the beetle elytron influenced the colouration aimed for in the assembled Bragg stacks. As shown in the image (Figure 6-12c) and the spectra previously presented (Figure 6-9e), the Bragg stack shows a more red-shifted peak than the stripe seen from the beetle elytron (Figure 6-12a). The aim was to mimic the system to display a desired colour, which in this case was orange. Figure 6-12(d) shows a typical TEM image cross-section through the structurally coloured elytra of the *C. rajah* beetle.

The periodicity visible in Figure 6-12(d) is derived from the alternating light contrasted and dark contrasted layers aligned parallel to the elytral surface. This differential contrast is associated with differential uptake of the staining chemicals in the elytron during TEM sample preparation. In the beetle itself, the high RI is understood to arise from regions rich

in melanin compared to the regions low in melanin content that are associated with low RI[17]. The layers have thicknesses of 70-120 nm which is of the order of visible light. A typical TEM image of a cross-section of the fabricated film is shown in Figure 6-12e and similarly comprises alternating light contrasted and dark contrasted layers of thicknesses between 100-210 nm. These thicknesses are not comparable to the modelled thicknesses due to changes that may have occurred during TEM preparation. Like those of the beetle, these layers have thicknesses of the order of visible light wavelengths.

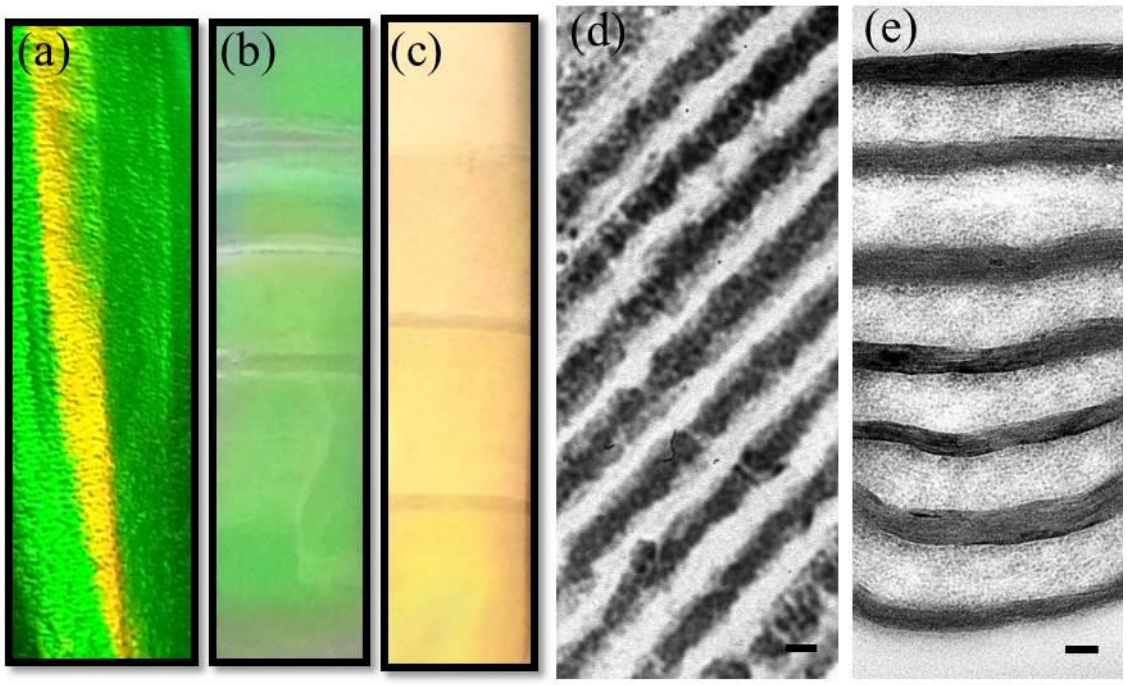

Figure 6-12 Photographs of the C. *rajah* beetle elytron (a), LbL-assembled green (b) and orange (c) Bragg stacks, and TEM cross section images of the *C. rajah* (d) and LbL-assembled green Bragg stack (e). Scale bars in both images represent 100 nm.

The images clearly show that each Bragg stack system is comprised of multilayers. The materials in each system are however different which results in inevitable differences in reflection behaviour. These differences in optical reflection are shown in Figure 6-13 where the chromaticity values (Figure 6-13a) highlight the difference in appearance of the *C. rajah* cuticle and the fabricated Bragg stacks. These differences are further enhanced by the reflection curves in Figure 6-13(b) which show a significant difference in a peak reflection at 700 nm from the orange Bragg stack and a peak reflection at 581 nm from the yellow stripe of the *C. rajah* beetle.

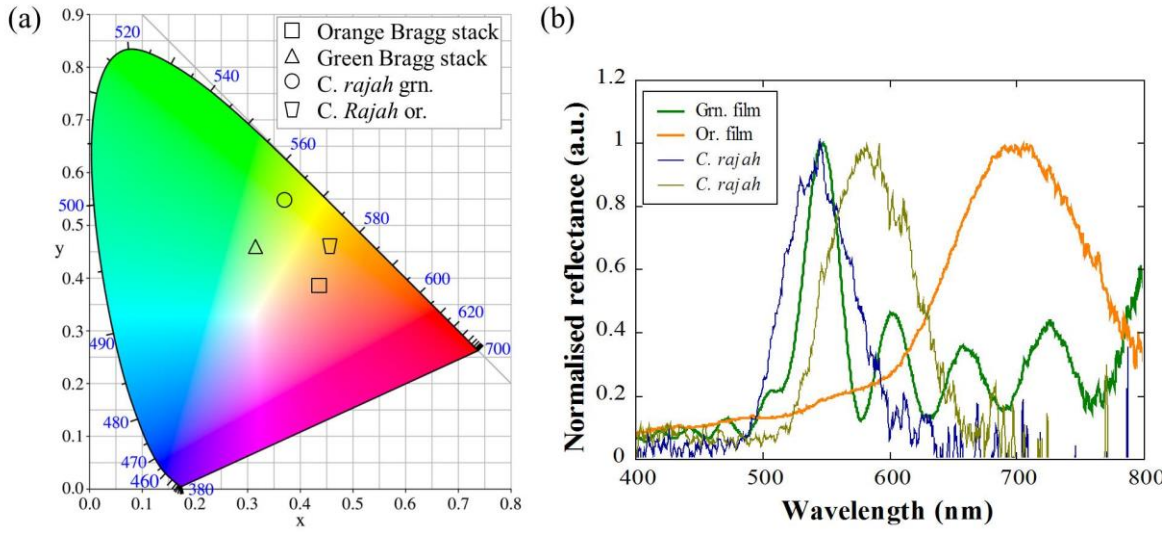

Figure 6-13 (a) CIE diagram with the chromaticity coordinates highlighted for the fabricated Bragg stacks and the *C. raja*h beetle. (b) Reflection curves for the *C. rajah* green and yellow regions and the two fabricated Bragg stacks.

The greens of the Bragg stack and the *C. rajah* possess similar peak reflections of 547 nm and 542 nm respectively. The idea of mimicking was not to develop an exact copy of the

C. rajah system but to display iridescent colour by synthetically constructing a system based on the *C. rajah* structure and optical behaviour.

The fabricated Bragg stacks possess a periodic structure derived from the selected materials that give rise to alternating high and low RI layers. The optical behaviour of this system can be calculated numerically and produce experimental results in good agreement with predictions. The iridescent fabricated Bragg stacks were made using an affordable, renewable material and were assembled using the LbL technique which can be altered to operate on an industrial scale. The LbL process also accommodates a wide range of constituent materials and substrates of varying size, stiffness and geometry.

6.8 Summary

CNCs have been applied to an LbL regime for fabricating thin multi-layered structurally coloured films. These films incorporated polyelectrolyte/clay and colloidal silica/cellulose nanocrystals that were applied by LbL deposition. The system was tuned by understanding the correlation between the number of bilayers and the resulting thickness and refractive index; information that was then used to model colour appearance for given bilayer combinations. The fabricated films exhibited similar morphology and optical properties to the integument of the bright green iridescent South East Asian *C. rajah* beetle. The structure within the films is a multi-layered system comprising layers of contrasting refractive index with thicknesses on the order of the wavelength of visible light. The fabricated films appear green and orange to the naked eye with peak reflections at 547 nm and 699 nm wavelengths respectively which blue-shift with increasing incidence/viewing angle. The green film possesses a narrow reflectance band matching both the numerical

model and the *C. rajah* beetle. The fabricated orange film possesses a reflectance band like the *C. rajah*. This band was broader due to the striations carved into the surface. It is assumed the film damage occurred during the washing process and possibly because inclusions were present in one of the solutions used for this film as no other damage was observed in the other films. The advantage of fabricating films in this way is that the LbL technique is simple, can be applied to complex geometries, is open to a range of materials and can be expanded to a cost effective continuous process.

Chapter 7 Circular Dichroism in CNC Thin Films

The optical properties of EISA CNC thin films are derived from the cholesteric structures formed during the liquid crystal phase as the concentration of the solution increases. The varying conditions during the drying process result in compositional changes which affects the optical behaviour across the film. Presented in this Chapter is evidence, obtained from a range of optical techniques, of the varying optical behaviours across EISA CNC films. More significantly, evidence is presented showing consistent reflection of RCP light from distinct regions of EISA CNC thin films which before were believed to only reflect LCP light. Alongside this, evidence of a correlation between CNC distribution and the reflection of RCP light is also presented. This work has recently been published by the author[236]. This Section also includes evidence of a correlation between phase composition, obtained from POM, and CPL reflection which compliments the work previously reported.

7.1 Optical analysis

As outlined in Section 5.1.2, sessile droplets from the 6 wt% CNC suspension were cast onto glass slide (GS) substrates. The cast droplets took approximately 15 minutes to dry and were pinned in every case, so that the resulting lateral dimensions of the films were equal to those of the cast droplet. The droplet shrank in the vertical plane as evaporation progressed. Once the droplet ceiling reached the height of the dry film forming around the edge, shrinkage occurred laterally. This lateral shrinkage created a drying line between the droplet and the dry film forming around the edge. The attractive van der Waal's forces at droplet-substrate interface induced contact angles of 29.7° (with a SD of 2.3°) which meant the droplet was pulled towards the substrate and formed a relatively flat, wide dome. Flow of replenishing solution towards the edge where pinning occurred was observed. Under these conditions the evaporation rate at the thin edge was rapid, increasing the net migration of water and suspended CNCs to the edge which has resulted in a clear coffee ring effect. The CNCs appeared to undergo rotation due to surface tension torque, described in Section 3.3, aligning parallel with the edge of the droplet having approached the edge in a perpendicular fashion. This process was visualised by viewing CNC droplets between crossed polarisers in a microscope setup (Figure 7-1). The blue and yellow interference colours in the images in Figure 7-1 are derived from the CNC long axis alignment with the slow optical axis of the quarter wave plate as described in Section 2.3.1. The compass in Figure 7-1(a) indicates the alignment of the long axis for each colour region. CNCs in the blue region are aligned with their long axis parallel to the film edge (the film edge is parallel to the dashed white line and in the direction of the white arrow). inwards. This growth was visible and occurred as yellow regions approached the edge and were then rapidly converted to blue regions.

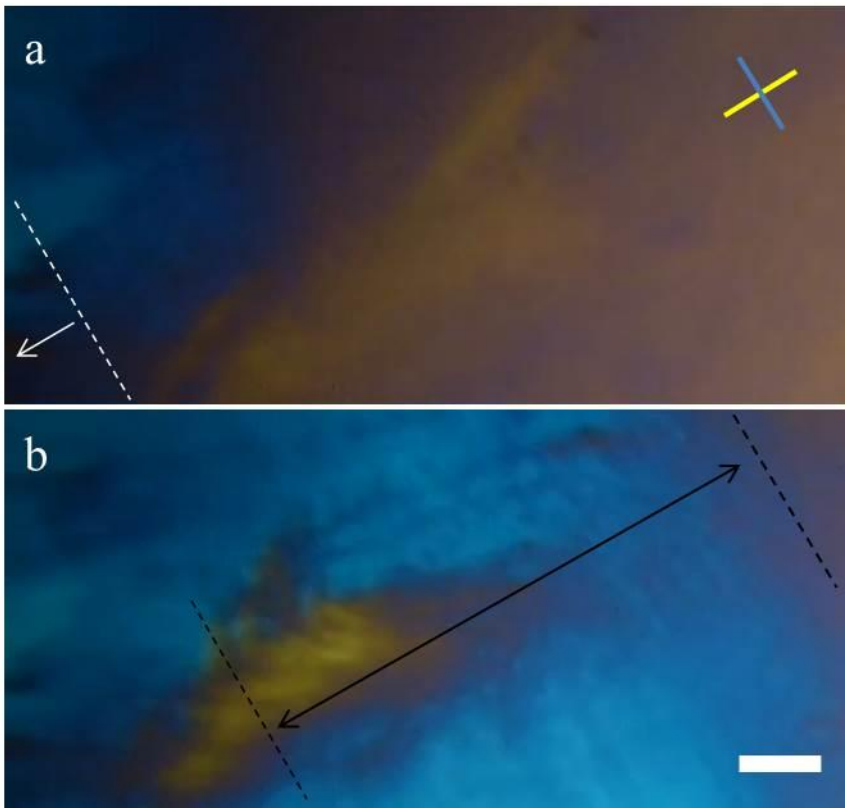

Figure 7-1 (a) A still image taken from video footage of a drying droplet. The white arrow points towards the film edge and the broken line runs parallel to the film edge. The compass in the top right corner indicates the orientation of the CNCs long axis to the slow optical axis of the wave plate. (b) The same area of the film 14 seconds later where the black dashed lines and arrow indicate the growth of the blue phase. Scale bar is 100 µm. Images are unpublished data.

The CNCs approaching the edge have their long axis aligned perpendicular to the film edge and appear yellow. In Figure 7-1(a) the blue region slowly grew from the edge. With progressive drying the blue region increased (indicated by the black lines) and the approaching yellow region disappears (Figure 7-1b). This change is due to the rotation of the CNCs at the dry edge. The change in orientation results in a change in the interference

colour observed which in this case is from yellow to blue. Where there is insufficient room for CNCs to rotate they remain in the orientation as when they approached the edge, hence the yellow island in Figure 7-1(b).

In the dry film, this is evidenced by a band of colour which is seen around the edge of the film (Figure 7-2a). This is indicative of the coffee ring effect (as described in Section 3.3) and is a result of the liquid crystalline ordering induced by the forces carrying and aligning CNCs at the edge of the film. At higher magnifications (Figure 7-2b and Figure 7-4a) the coloured ring is discretised into a broader spectrum of colour where narrow bands of red and yellow are seen at the very edge and broader bands of blue and indigo are seen inside the narrower bands. Also, visible in this region is a surface roughness texture which is further highlighted in the dark field image in Figure 7-2(c) where light readily scatters from the more textured regions. These regions consist of surface roughness and defects in the otherwise homogenous liquid crystalline structure which appears dark except for where it is obscured by the scattered light from the surface roughness. POM images highlight the effect of the drying mechanics which has resulted in a relatively homogenous film as shown in Figure 7-2(d). The colours are indicative of the alignment of the slow optical axis of the CNCs to the retardation plate as explained in Section 2.3.1 and illustrated in Figure 3-4(b). The CNC nematic phase aligns parallel to the film edge and follows the curvature of the film. As the nematic phase follows the curvature of the film through 360˚, CNCs are aligned at varying angles with respect to the polarising filters. This gives rise to the Maltese cross seen in Figure 7-2(d).

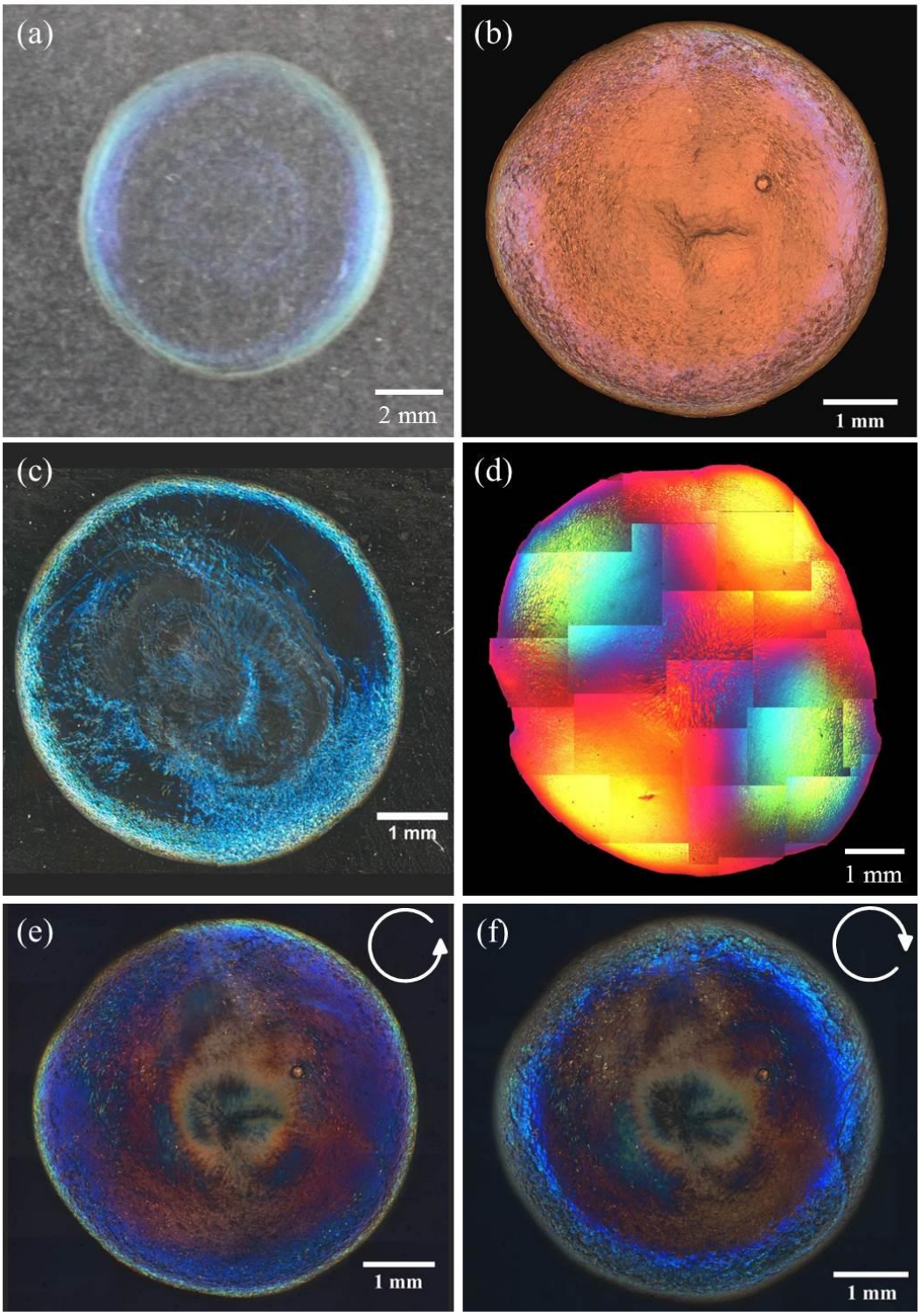

Figure 7-2 A photograph of a CNC thin film on a glass substrate (a). Bright field image of reflection of non-polarised light from a CNC thin film highlighting the iridescent ring, present due to the coffee ring effect (b). Dark field image of a CNC thin film highlighting isotropic regions from which light is scattered (c). POM image highlighting CNC phase distribution across the film (d). Reflection of LCP and RCP from the same CNC thin film (e-f).

In the prepared films, the CNCs were forced to align parallel to the edge of the film and so possess a preferential optical direction. This was consistent around the whole film and is why blue and yellow complimentary quadrants separated by the Maltese cross are seen in Figure 7-2(d). The most interesting feature observed was when the films were illuminated with CPL. The expected reflection of LCP light was observed in a strip around the very edge of the film (Figure 7-2e). However, inside of and adjacent to the LCP reflecting strip was a region reflecting RCP light. This region forming a ring around the film is shown in Figure 7-2(f). The significant and consistent reflection from this region suggested the possibility of a phase change, possibly even a change in chirality, which has not been observed in LC or dried films of CNCs before. Further investigation of the relationship between phase composition and CPL reflection was carried out by obtaining higher magnification images of the birefringent effects observed in POM (Figure 7-2d). A series of higher magnification images were compiled to show a strip of film from the edge towards the centre which was compared to scaled images showing the reflection of RCP and LCP light (Figure 7-3centre). A correlation was found between the change in reflection of CPL and the phase composition of the film. The edge of the film is at the top of each image and the area above the top dashed white line is where the reflection of LCP is dominant and the phase composition is relatively homogenous. In the area between the dashed lines, the reflection of RCP is more dominant and is where multiple phases begin to appear. The phase composition in this region of film is less homogenous. Moving past the second dashed line to the bottom of the centre image, another change in phase is seen. The colours of the multiple phases in this region appear more saturated. It should be noted that the centre image represents transmitted light and the increase in colour saturation may correspond to a significant decrease in film density.

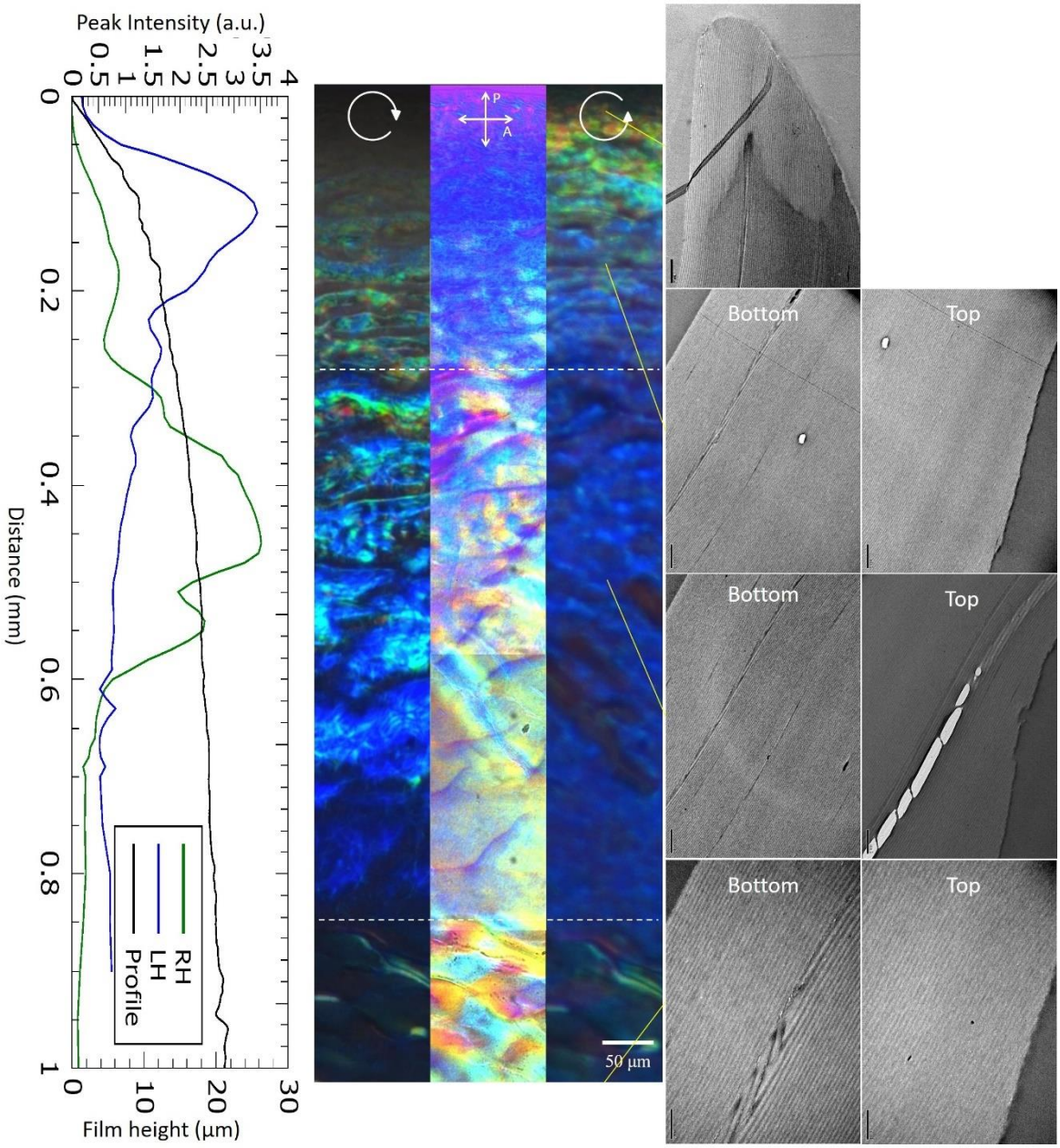

Figure 7-3 Centre: Three images of the same section of film showing RCP reflection (left), birefringence (centre) and LCP reflection (right) from a narrow section of an EISA CNC thin film. The edge of the film is at the top of the images. Dashed lines highlight phase changes correlating to variations in CPL reflection. Left: Peak intensity of LH and RH CP reflection as a function of distance from the edge of the film. The reflection profiles are shown against the film height profile. Right: TEM images showing film morphology at various intervals from the edge. TEM scale bars are 2 µm.

A decrease in film density would also explain and correspond to the decrease in reflection observed in the CPL images on both sides. Peak reflection profiles of LHCP and RHCP are shown in Figure 7-3 left. These are presented with the film height profile and show little correlation between film height and peak intensity. The peak reflection of LHCP and RHCP light are clearly shown to occur in separate regions of the film. These peak reflections correlate with a change in phase composition in the film. TEM investigation of the film revealed little about the distinguishable features observed in the light microscope. TEM images are presented in Figure 7-3 right. These findings are discussed in greater detail below.

7.2 MSP Analysis

The CNC film presented in Figure 7-4(a) and Figure 7-3(centre) was characterised using MSP fitted with CPs. Areas from each of the LCP and RCP reflecting regions were investigated in both reflection and transmission. The close-up image in Figure 7-4(a) shows reflection of LCP light in a narrow strip around the edge of the film. Within this reflection strip are bands of colour which are orange at the very edge of the film and which blue-shift across the strip to appear more violet. The colour reflection diminishes in intensity approximately 200 μm from the edge of the film. The corresponding colour map in Figure 7-4 (b) highlights the reflection of wavelengths from ~550 nm at the very edge which then blue-shift to ~400 nm across the reflecting strip towards the centre of the film. The reflection of RCP light is seen in a similarly narrow strip adjacent to and inside the LCP region (Figure 7-4c). This strip is similar in width but presents a narrower band of

colour as can be seen in the colour map which shows a complete blue-shift from ~520 nm to ~450 nm (Figure 7-4d).

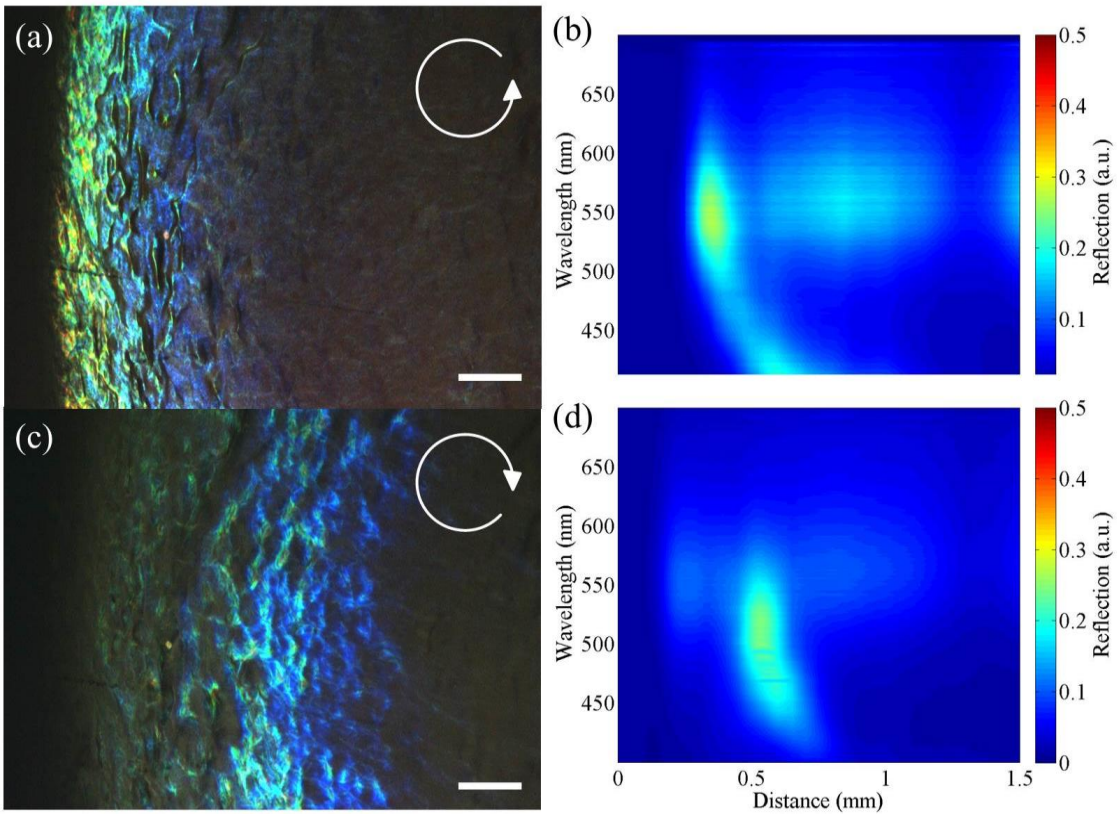

Figure 7-4 (a) Typical microscope image showing LCP reflection from the edge of a CNC film and the corresponding MSP spectra, presented as a colour map showing reflection of LCP light as a function of distance (b). Typical microscope image showing RCP reflection from the same CNC thin film shown in (a) and the corresponding colour map (c-d) respectively. Scale bars are 100 µm.

The bands are separate and distinct; this is confirmed by the MSP data taken from the same section of film using LCP and RCP filters Figure 7-4(b,d). Reflection and transmission spectra were further obtained from specific areas within each LCP and RCP reflecting regions (Figure 7-5 and Figure 7-6) and show complimentary colour transmission of RCP and LCP light. The region where LCP light is reflected consistently transmits RCP light. The strip reflecting RCP light also showed complimentary transmission of LCP light. The

image in Figure 7-5(a) shows the area where reflection and transmission of LCP and RCP spectra were taken from in the LCP reflecting region. The relative intensities of the images

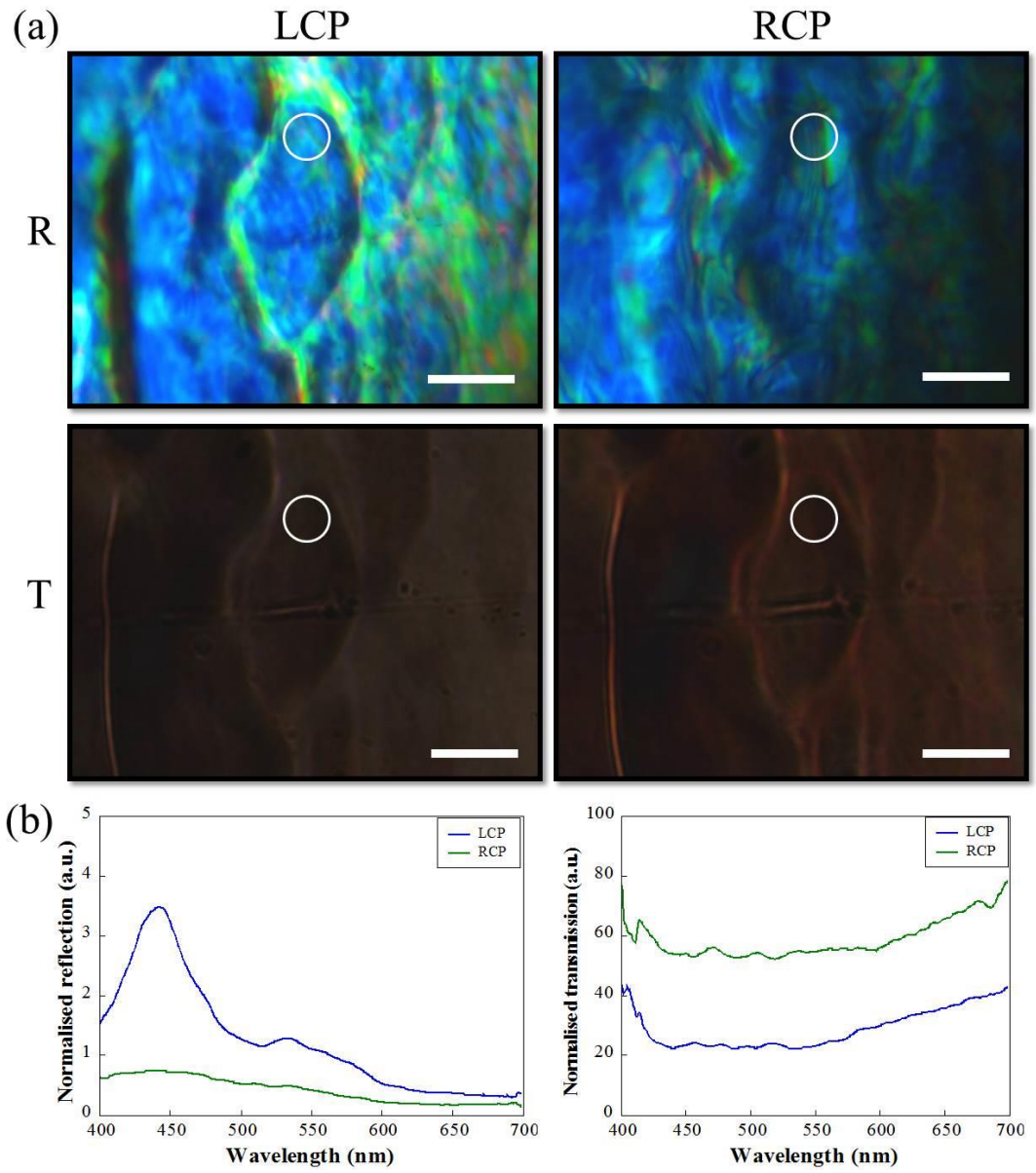

Figure 7-5 Optical microscope images of the same area of the film observed through LCP and RCP filters in reflection and transmission (a). The area of the film was within the region reflecting LCP light. The circle marks the location of the beam spot. (b) LCP and RCP light reflection (left) and transmission (right) spectra taken from the area marked in (a). Scale bars are 20 µm.

indicate the dominance of LCP reflection and the complimentary RCP transmission. The corresponding spectra are presented in Figure 7-5(b) where clear dominant reflection intensity is seen for LCP light and a complimentary intensity of transmitted RCP light. It can also be seen that reflected RCP and transmitted LCP are not completely cancelled out. Likewise, the images and spectra for the RCP reflecting region show complimentary reflection and transmission of RCP and LCP light (Figure 7-6a). The complimentary reflection and transmission data (Figure 7-6b) suggests the possible presence of a right handed chiral structure and that the film changes from a left handed chiral structure at the edge to a right handed chiral structure further in. Although complimentary reflection/transmission was measured at specific points within each region, the data recorded from each reflecting region was not always consistent. Some areas in both regions showed nearly equal intensities of reflected LCP and RCP light. In one area investigated of the RCP reflecting region LCP light was observed to reflect with a greater intensity than the reflection of RCP. The corresponding transmission curves for these areas were not complimentary and show that the regions, though consistent on a broad scale have many inconsistencies on a microscale (Figure .1 and A.2 of the appendix). The reflection of LCP light was consistently present in the RCP reflecting region while the reflection of RCP from the LCP reflecting region was not always present (Figure A.1). The inconsistency in the RCP reflecting region indicates the presence of a left-handed structure and that RCP light could be reflected from structural defects which may be a result of the reduction in the amount of CNCs being carried to the edge as the drying line progresses toward the centre of the film. TEM analysis was performed to shed light on this issue

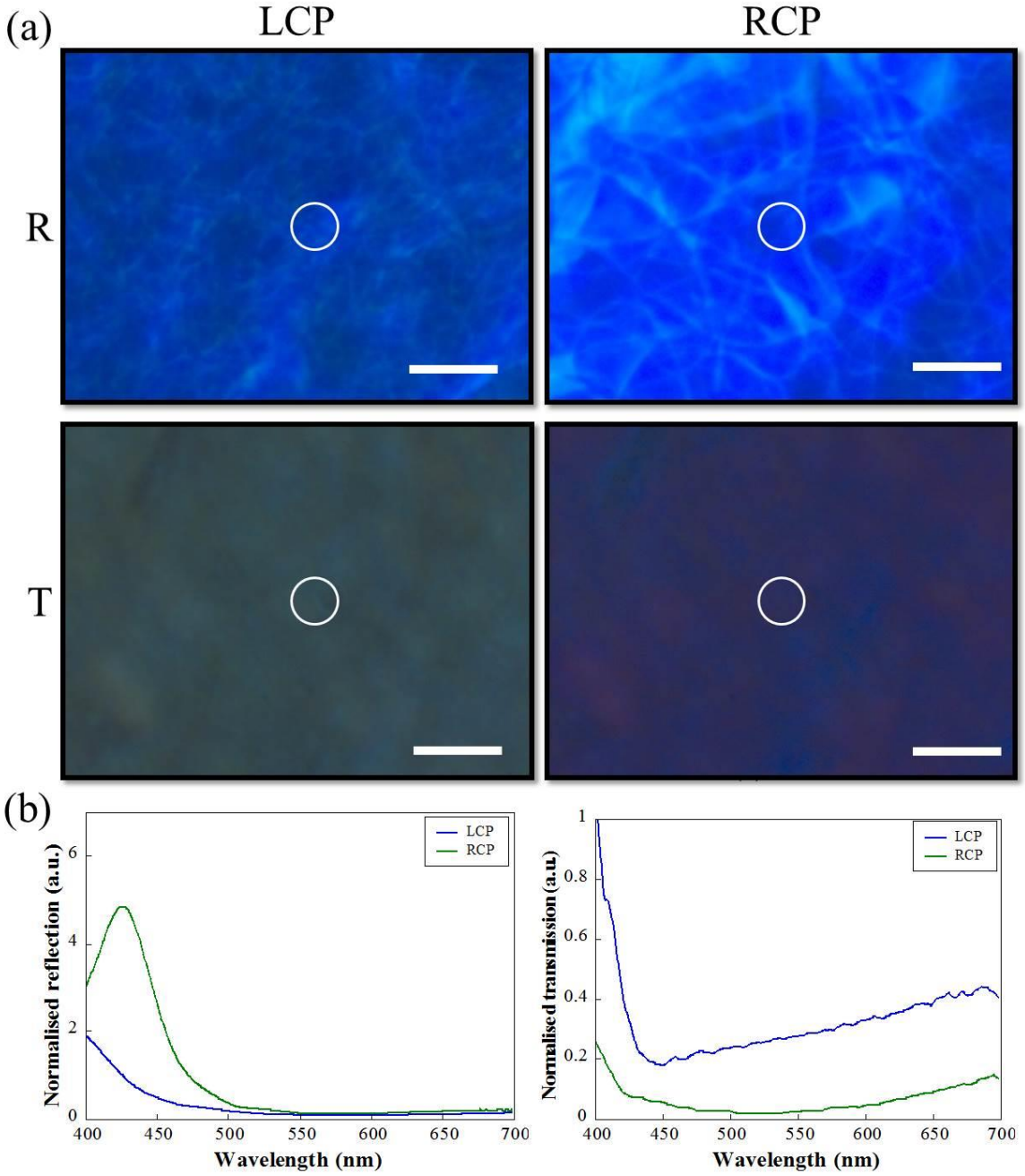

Figure 7-6 (a) Optical microscope images of the same area of the film observed through LCP and RCP filters in reflection and transmission. The area of the film was within the region reflecting RCP light. (b) LCP and RCP light reflection (left) and transmission (right) spectra taken from the area marked in (a). Scale bars are 20 µm.

7.3 TEM Analysis

The ultrastructure of cross sections of EISA CNC thin films were analysed using TEM, the preparation of which is explained in Section 5.2.3. A TEM image of a section through a complete edge of a CNC thin film is shown in Figure 7-7(a). From the very edge of the film a multilayer structure is clearly seen with layers aligned parallel to the film surface and what would have been the substrate surface the film was cast upon. What was surprising was how uniform the multilayer structure is throughout the film. Figure 7-7(b) shows a continuation of this structure from the edge and Figure 7-7(c) a section from the centre of the film where the only obvious disruption to the film is the damage caused during TEM sample preparation. The multilayer structure is consistent throughout the film. The dark patches in Figure 7-7(a) and (b) are where there is an excess of the uranyl acetate used to stain the samples. It was, however discovered that staining was not necessary and that sufficient contrast was obtained in the film structure to differentiate specific features. The light and dark lines that make up the overall multilayer structure observed in Figure 7-7 are produced by the twisting of the nematic phase along the helical axis which gives rise to a periodic variation in RI. The higher RI regions offer greater resistance to passing electrons and so appear darker than the lower RI regions that offer less resistance. The curvature responsible for the layering observed was visualised at higher magnification. TEM images of oblique cut cross sections of the CNC thin film are shown in Figure 7-8(a,b).

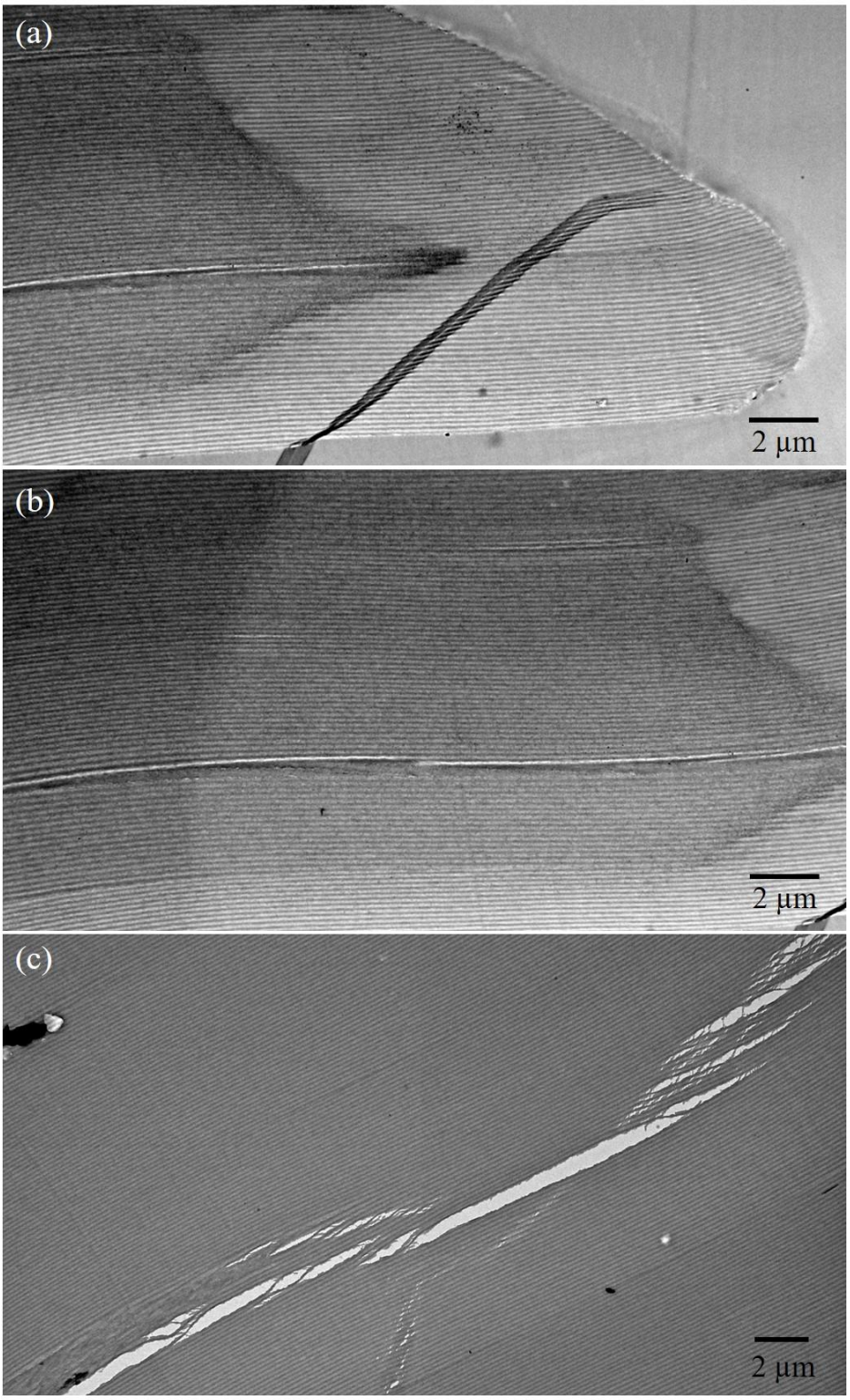

Figure 7-7 TEM images of a CNC film cross-section. The edge of the CNC film (a) with a visible multilayer structure. The lamella structure is consistent throught the film as shown in (b) which is an image of a part of the film adjacent to (a) and one taken from the centre of the film (c) where the lameller structure is also seen. The dark ribbon in (a) is where the film has folded during sample preparation.

The curvature seen in these images is indicative of a chiral structure, the arches of which are called Bouligand curves. Particular areas at the edge of the films were investigated to assess the direction of the curvature. The Bouligand curves in the EISA CNC thin films investigated were all found to 'arc' in the same direction and though it is not possible to identify handedness of the chiral structure it was assumed that the presence of opposite curvature direction would suggest a change in handedness from one region to another. This search was by no means exhaustive; it was impractical to look at every region of every film on such a small scale with such a small field of view. The uniform multilayer and chiral structures throughout the film are in agreement with SEM investigations of Park *et al.*[182] and Majoinen *et al.*[39]. It was thought that a change in structure would be observed in the images in regions where RCP light is reflected, for example, the presence of a unidirectional layer within helicoidal regions has been observed in certain beetle integument[52,237]. The unidirectional layer exhibits half-wave retarding properties which changes the handedness of incident CPL so that both hands of CPL can be reflected when only one polarisation is incident. No such layer was seen in the TEM images. Defects can be another cause in the change of polarisation state of incident light. Some examples of defects observed are shown in Figure 7-9. The defects found in the layered structure are consistent with the observations of Wang *et al.*[171] which are described in Section 3.4. The main defect observed was identified to occur periodically in every film and was that of a phase boundary, examples of which can be seen in Figure 7-9(a,b,c). These defects are created after the formation of tactoids during the initial self-assembly process which then fuse to form the overall film.

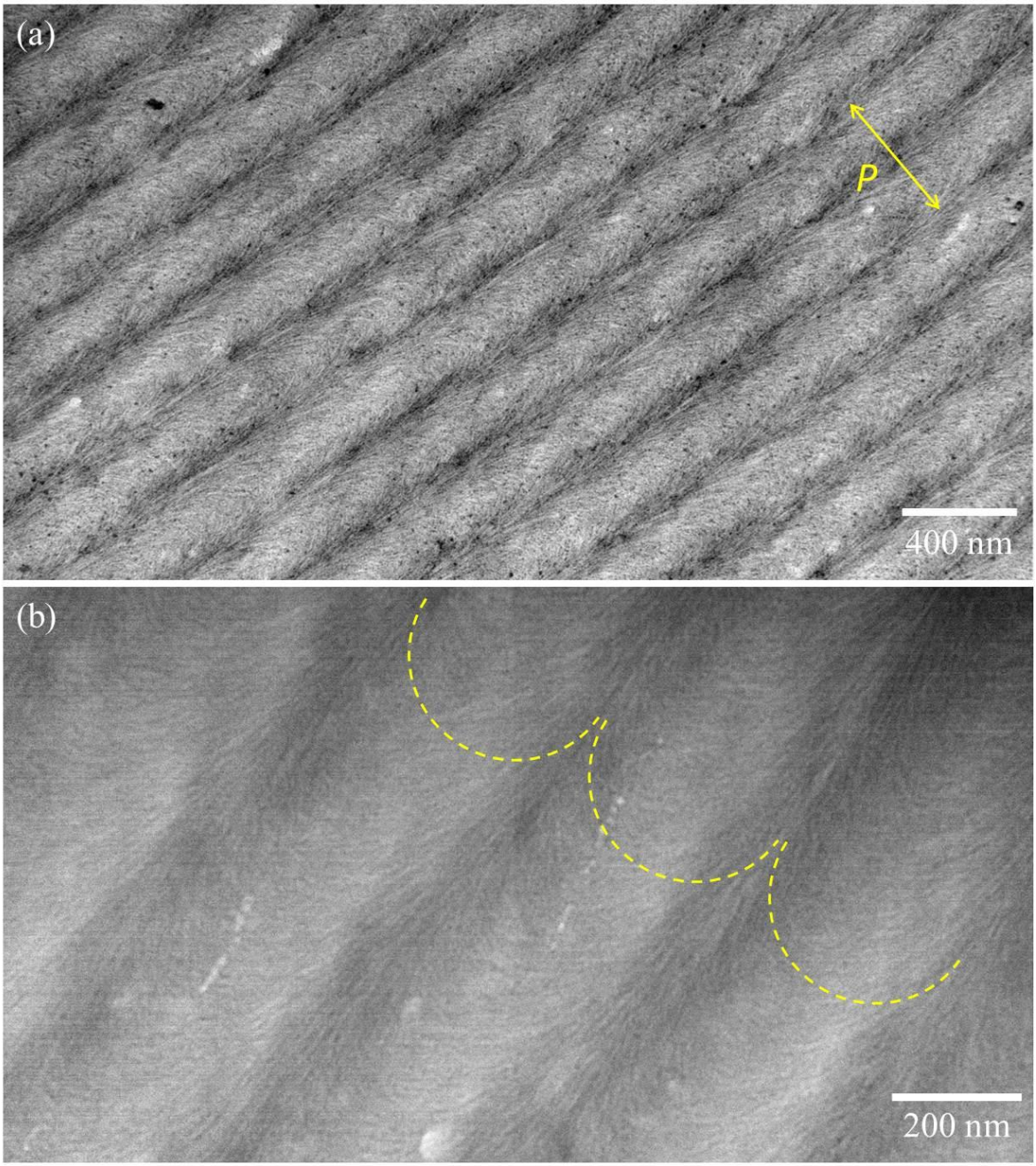

Figure 7-8 (a). A typical TEM image of a CNC film cross-section showing the ultrastructure between each layer. The pitch length is indicated by *P*. (b) Higher magnification TEM image where the Bouligand curvature is visible (highlighted by the yellow dashed lines).

In Figure 7-9(a) three phases can be seen at the top middle and bottom of the image. They formed from separate tactoids and developed until sedimentation which occurred before

the phases could completely align thus forming the phase boundaries. The chevrons formed in Figure 7-9(b) are thought to occur from one tactoid pushing its way into the continuous structure of another causing it to open up. The phases either side are left oriented at an angle to each other. The defect in Figure 7-9(c) is a disruption in the continuous layers of a single phase. The other defect found is shown in Figure 7-9(d). It consists of multiple ellipsoidal regions that are between 4-25 μm in length and 1.2-4 μm thick. They align parallel to the layers in the film structure and are distributed randomly in a given section of film from top to bottom. Due to film damage on this particular sample the specific region of the film could not be identified and linked to an RCP reflecting region. The defects appear to be isotropic as no regular structure is discernible. As far as the capacity of the defects goes to affect change in the polarisation state of incident light there is little to suggest any of them are responsible. The fusion defects are small and occur just as much in both reflecting regions of the film. There is no obvious difference between the reflecting regions of the film outlined in Figure 7-3. There is also no evidence that a relatively discrete phase boundary can either change the polarisation state of incident light or reflect the opposite hand. It has been shown that replacing a thin layer of a given liquid crystal with an isotropic material as a defect that defect modes are induced for both polarisation sates of incident light[238,239]. It would be unlikely that the isotropic ellipsoidal defects were responsible for RCP reflection as they were only observed in one of the films analysed. With no obvious change in structure between the LCP and RCP reflecting regions the spectroscospic method for measuring the CNC distribution was used to establish a relationship between the change in polarisation and the structure (Section 7.4.).

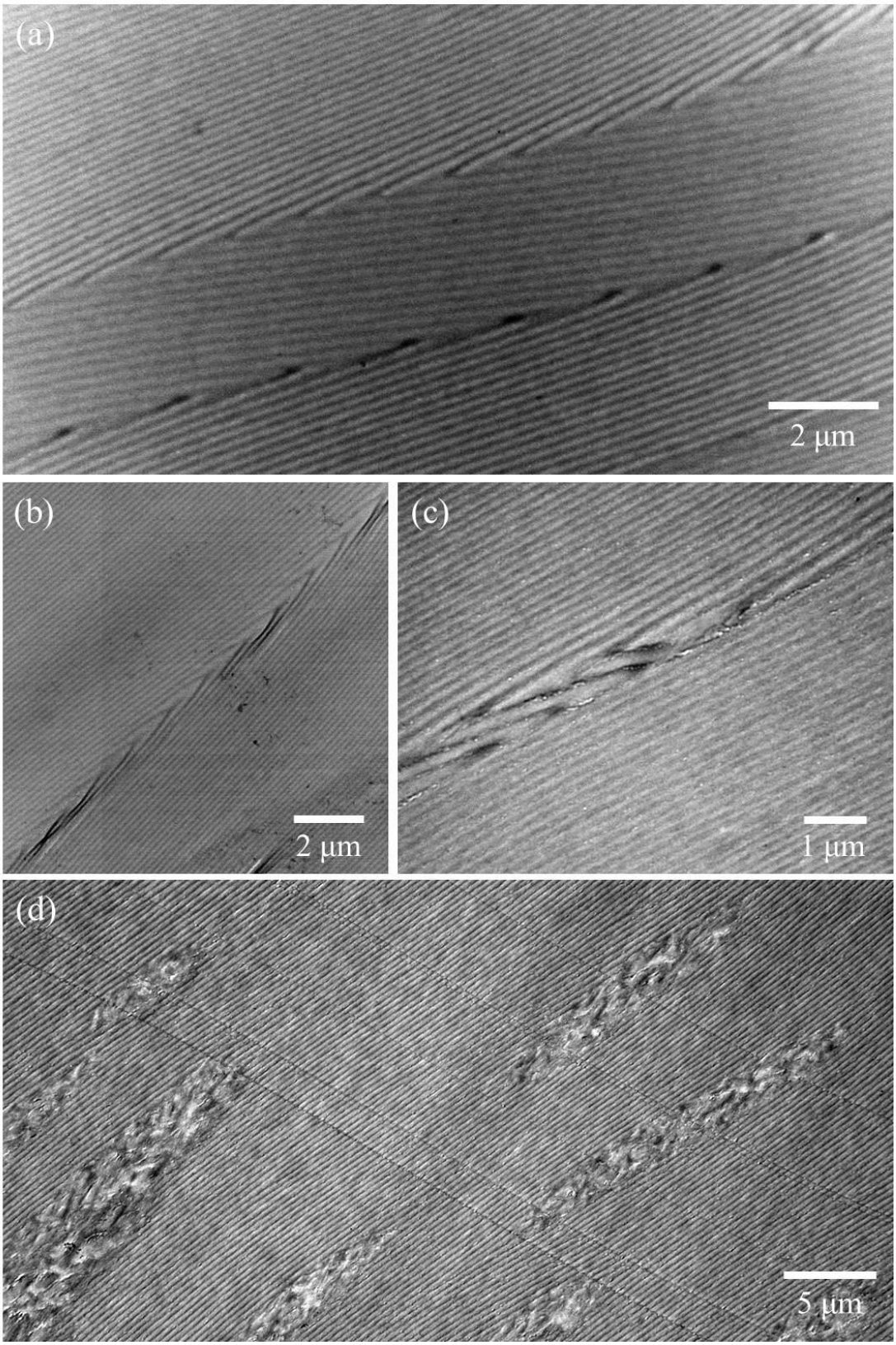

Figure 7-9 TEM images showing film defects. (a-c) Tactoid fusion defects. (d) localised isotropic defects.

The TEM analysis did provide information on pitch lengths which informed the simulations performed to calculate reflection of LCP light and pseudo Bragg reflections. Measurements of the pitch length were averaged from 5 sections of a film where images of the full top to bottom cross section could be obtained. Small variations in pitch length were observed from measurements taken along the z-axis and are expressed in the averaged values in Figure 7-10(a). The two largest error bars are a result of phase boundary defects and not due to large differences in the continuous layers. The pitch lengths were observed to vary along the film normal, tending to be shorter at the bottom (~270 nm) of the film and longer at the top (~310 nm). The pitch lengths were used to simulate reflection from the cholesteric structure as described in Section 5.4.1. The blue curve in Figure 7-10(b) represents the simulated narrow band reflection of LCP light which has peak reflectance at 432 nm. The experimental reflection curve (green) is in good agreement with a peak reflection of 420 nm and high saturation. Similarly the pseudo Bragg reflection curves in Figure 7-10(c) are also in good agreement. The curve representing the experimental measurements (green) is broader and less saturated than the curve representing the modelled reflection (blue). The peak reflection of the modelled curve is 391 nm and 394 nm for the experimental curve. Spectroscopic measurements using the goniometer reflection measurement setup explained in Section 5.3.1 were performed to explore the angle dependence of the reflection of LCP and RCP light. The data presented in Figure 7-10(d) shows that for incident angles ranging from 10 to 60° optical behaviour for LCP and RCP light follow a similar monotonic decrease with an increasing incident angle. This decrease in reflection with increasing incident angle is associated with the shift in the peak intensity and is typical behaviour of the continuous structure examined here.

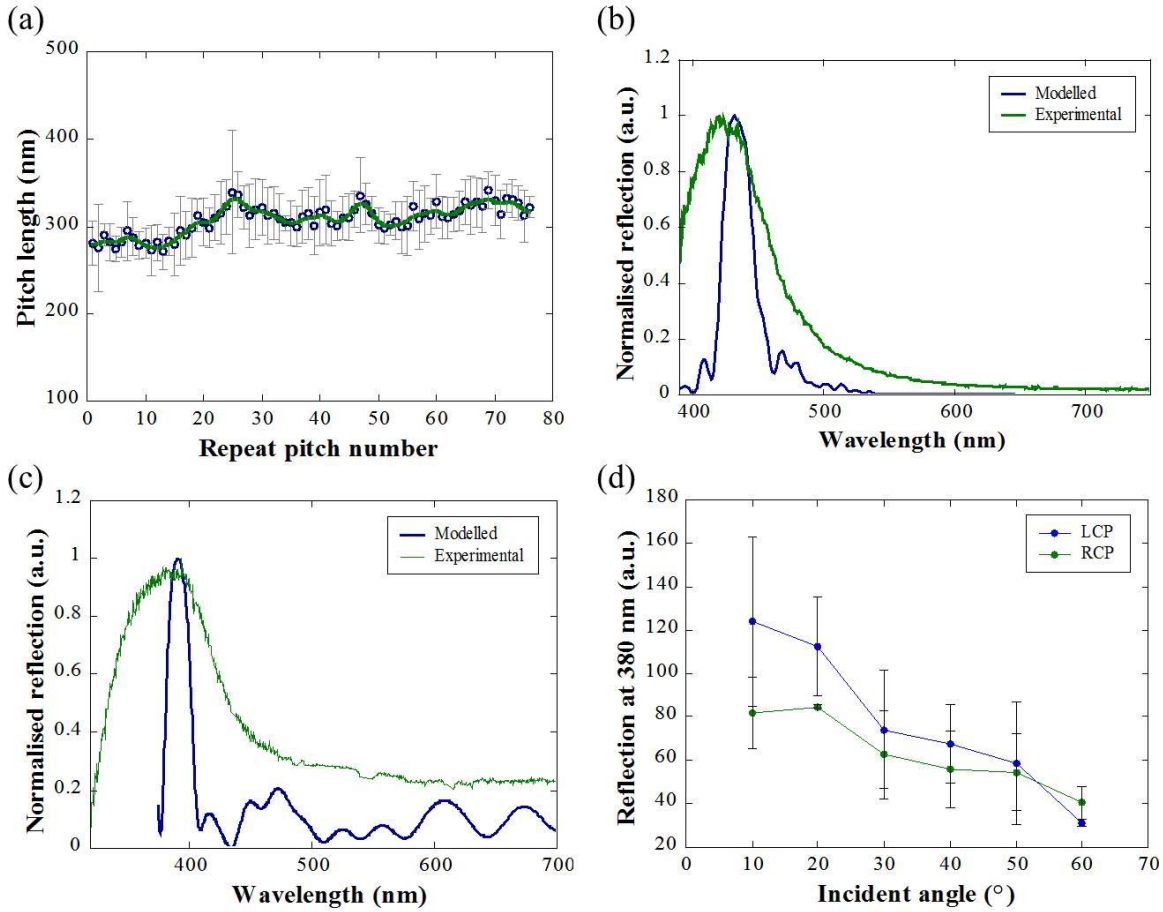

Figure 7-10 (a) Pitch profile along the z axis for a given section of film. (b) Modelled and experimental reflection measurements of LCP light based on the pitch measurements in (a). (c) Modelled and experimental reflection measurements of non-polarised light from the multilayer stack. (d) LCP and RCP reflection at 380 nm as a function of the incidence angle, of which both follow a similar trend.

The reflection measurements outlined match theoretical simulations of reflectance of both LCP and non-polarised light from the films (Figure 7-10 b and c) and no significant difference was seen in the angle-dependence of reflected CPL. The reflection of RCP light remains unexplained as no evidence could be discerned in the TEM cross-sections for a structure that would produce such an effect.

7.4 Film volume and CNC mass distribution

As the reflection of RCP could not be explained by the more conventional methods the spectroscopic approach outlined in Section 5.1.2 was developed to assess CNC distribution. This approach involved combining film dimensions with spectroscopic techniques to obtain information about the distribution of CNCs along a given line spanning a diameter of a CNC film. Average nanocrystal dimensions (length and width) were measured from transmission electron micrographs, an image of which is shown in Figure 7-11. The TEM image is shown alongside distributions of CNC length and width measurements.

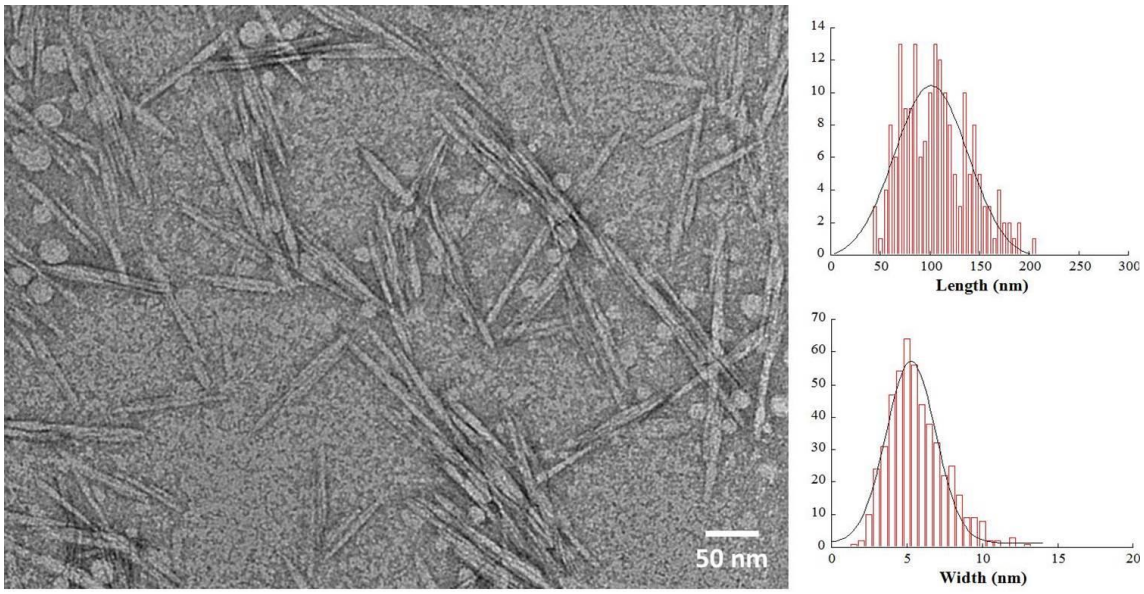

Figure 7-11 A typical TEM micrograph of CNCs and the histograms of length and width measurements superimposed by a Gaussian fit (solid line).

The average length and width of an individual CNC was 108 nm × 6 nm (with respective standard deviations of 34.5 nm and 1.9 nm). From these averaged values the volume and

mass (based on a density of 1.5 g cm^{-3}) of a single CNC (V_{CNC} and m_{CNC}) were calculated at 388.8×10^{-20} cm^3 and 5.8×10^{-18} g respectively. With a known mass of a single CNC the total number (N) of CNCs in a film was calculated using the equation,

$$N = m/m_{\mathrm{CNC}} \tag{44}$$

where m is the mass of the film which is 6 wt.% of the cast droplet. The volume of the film (V) is then obtained by multiplying N by the volume of individual nanocrystals. So,

$$NV_{\mathrm{CNC}} = V. \tag{45}$$

The mass of the solid content and the theoretical volume were calculated for film number 1 to be 0.654 mg and 436×10^6 μm^3 respectively. The volumes of 8 films were calculated using an average area and individual areas (as explained in Section 5.2.1) are presented in Table 7.1. A very good match can be seen between the volumes calculated from one averaged area and from individual areas with the better values possessing a difference between 0.2×10^6 μm^3 and 6.2×10^6 μm^3. Films 2 and 3, though still very similar differed significantly more than the other films with differences of 68×10^6 μm^3 and 46.8×10^6 μm^3 respectively. These larger differences are the result of additional peaks that appear in the profile data for specific cross sections recorded. The peaks are most likely the profiles of contaminants on the surface of the film during profilometry. When calculating the volume from the individual profiles the additional peaks are perpetuated, which explains the higher values of 515.9×10^6 μm^3 and 492×10^6 μm^3 respectively.

Table 7.1 The mass of CNCs in each film and the theoretical and calculated volumes of the dry films.

Film number	Mass of CNCs (mg)	Theoretical Volume ($\times 10^6$ μm^3)	Volume based on average area ($\times 10^6$ μm^3)	Volume from individual areas ($\times 10^6$ μm^3)
1	0.654	436	483.1 ±0.0077	483.3 ±0.0077
2	0.534	356	447.9 ±0.0076	515.9 ±0.0083
3	0.540	360	445.2 ±0.0067	492.0 ±0.0079
4	0.594	396	504.2 ±0.0061	504.3 ±0.0061
5	0.618	412	548.5 ±0.006	548.6 ±0.006
6	0.564	376	528.7 ±0.0063	528.7 ±0.0063
7	0.612	408	475.7 ±0.0067	478.3 ±0.0067
8	0.540	360	529.6 ±0.0074	535.8 ±0.0075

The reason the values (447.9×10^6 μm^3 and 445.2×10^6 μm^3) of the volume calculated from one averaged area are smaller is because the additional peaks are minimised when averaged with profiles without additional peaks. A good match is seen overall between the theoretical volumes calculated and the volumes calculated from profilometry measurements. The theoretical volume values are smaller, this expected result was discussed in Section 5.1.2, with respective differences to the higher measured volumes of 10%, 21%, 20%, 22%, 25%, 29%, 14% and 32%. These values, as far as packing fractions are concerned are very low and would indicate a very efficient packing of CNCs within the films[240,241].

Non-polarised light was used to take reflection and transmission spectra across the diameter of the film as shown in Figure 5-3(a). Absorbance was then calculated for a number of points and used to correlate that distribution of the known mass within the volume of the film from which spectra had been taken from. A distribution profile showing mass distribution at the edge of the film is presented in Figure 7-12(a) along with the film cross section profile. A complete film distribution is shown in Figure A.3 where the only significant variation occurs at the very edge of the film. It is at the very edge that differences in optical behaviour are observed and is why only the highlighted section is presented here. It can be seen from Figure 7-12(a) that CNC concentrations are significantly higher at the edge of the film where a CNC concentration of 27.7 g cm^{-3} rapidly decreases to 2.4 g cm^{-3} and then undergoes an incremental decrease to ~0.7 g cm^{-3}. It is along this gradient that that the wavelength of light reflected and the reflection of CPL also changes. The vertical dashed lines in Figure 7-12(a) highlight the colour transitions from the edge of the film inwards. Colours at the red end of the visible spectrum are observed in the first band (up to the first dashed line). This then transitions to yellow and green colours in the middle band. In the broadest section, between the last two dashed lines, blue and purple colours are observed up to the final dashed line after which no more colour is observed or reflection is diminished. Along with the change in reflected wavelength between the dashed lines is a change in the concentration of CNCs. The increasing concentration of CNC material correlates with a red shift in the reflected wavelengths of light. This change fits with the understanding that higher CNC concentrations result in a tighter pitch which correlates to a red shift in reflected light[19,182,242].

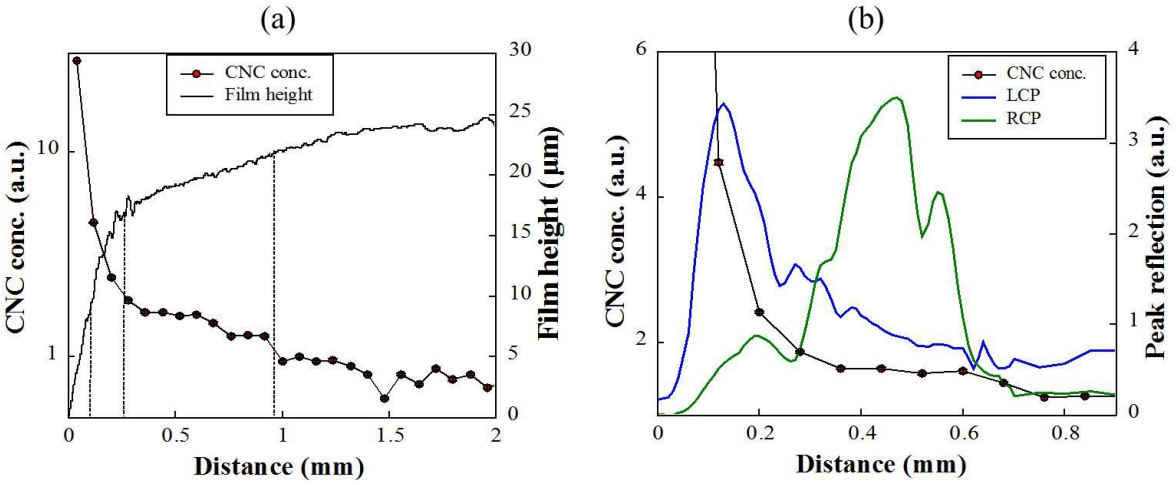

Figure 7-12 (a) Log plot of CNC concentration shown with film profile as a function of distance. Dashed lines indicate a colour transition. (b) Highlighted section of the CNC concentration shown with the peak reflection of LCP and RCP light along the film profile shown in (a).

Plotting the CNC concentration against the peak reflection of both LCP and RCP light (Figure 7-12b) reveals a clear difference between the CNC concentrations in the regions reflecting LCP light and those reflecting RCP light. LCP light is strongly reflected from regions of higher CNC concentration and RCP light from regions of comparatively lower CNC concentration. This observation compliments the data presented in Figure 7-3 and Figure 7-4, where a consistency is seen in variation between the regions of film reflecting CPL. The rapid decrease in concentration occurs in the region where LCP light is reflected. RCP light is reflected from regions where the CNC concentration is below 2g cm^{-3}. Reflection of both LCP and RCP light diminish when the CNC concentration falls below ~0.7g cm-3. Assuming there is no right handed chiral structure, the data suggests that a CNC concentration threshold exists, whereby below a specific CNC concentration changes may occur in the physical structure that are sufficient enough to alter the optical behaviour.

Further analysis of the CNC mass distribution data is presented in Figure 7-13. Absorbance (normalised to the film height) is shown to monotonically increase with increasing CNC concentration (Figure 7-13a).

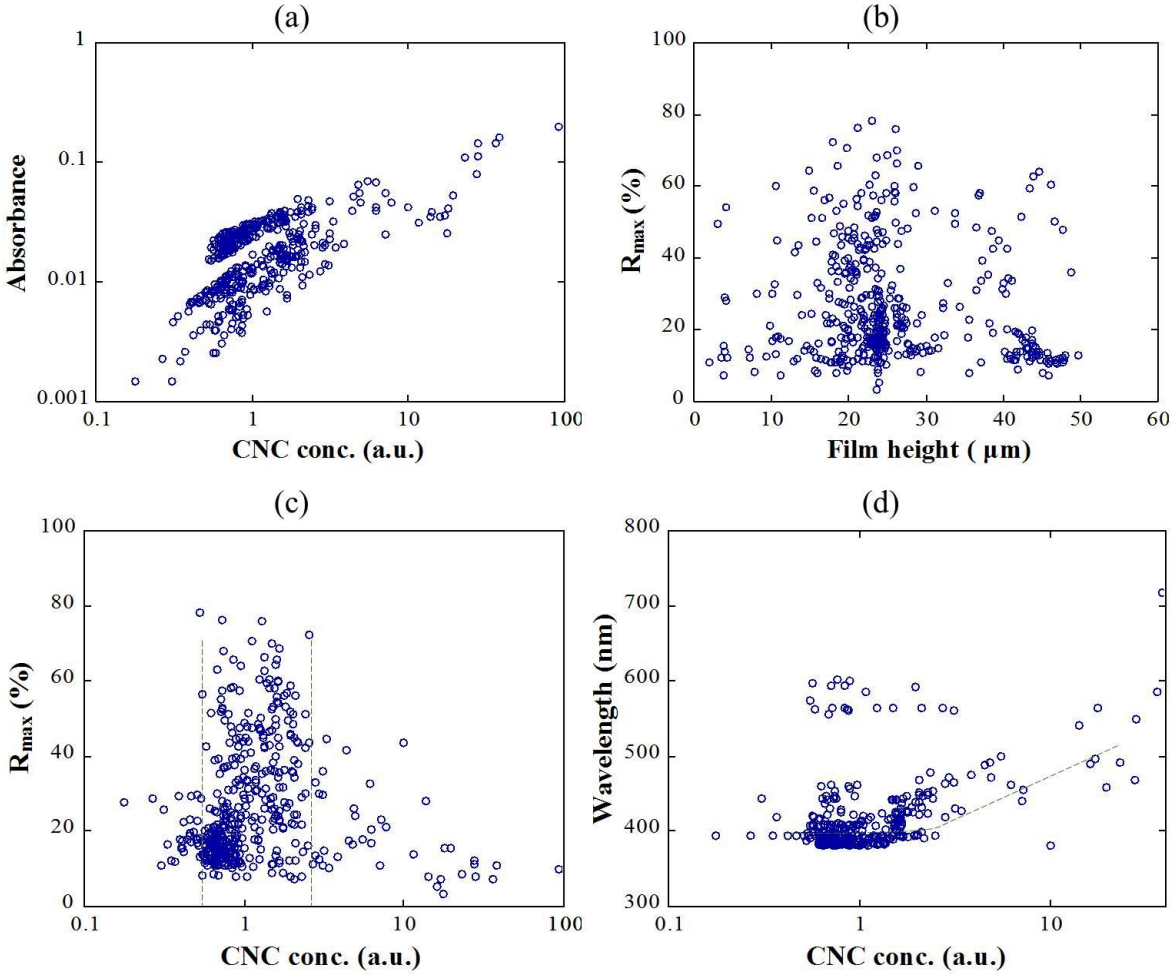

Figure 7-13 (a) Log plot of absorbance normalised to the film height as a function of CNC concentration. (b) Peak reflectance (R_{max}) as a function of film height. (c) Peak reflectance as a function of CNC concentration. The dashed lines highlight the narrow concentration band where R_{max} is high. (d) Plot of wavelength of reflected light as a function of CNC concentration. The dashed line highlights the red-shift in reflected wavelength with increasing concentration.

The peak intensity (R_{max}) reflection values of non-polarised light were not observed from the thickest film regions; reflection appeared to decrease with increasing film height until R_{max} was normalised to film height and it was seen, as shown in Figure 7-13(b), that no correlation was had between R_{max} and film height. The majority of the reflected light, however seems to occur at a film height of ~25 μm, approximately half the maximum film height. The highest intensity reflections also occur at this film height. A pronounced column of data is observed in Figure 7-13(c) where peak reflections occur within a narrow CNC concentration band (highlighted by the vertical dashed lines).

Figure 7-13(d) shows the reflected wavelengths, for the same films, as a function of CNC concentration. Two bands are seen, a narrow band at ~580 nm and a slightly broader band located at ~400 nm. As the CNC concentration increases the band located at ~400 nm red shifts and the narrow band at ~580 nm disappears. Both these transitions are directly correlated with a change in the concentration of CNCs, thereby providing a link between optical and structural features.

Consistencies in the reflection behaviour observed were found in films prepared on different substrates. Films were prepared on glass, quartz and graphene substrates where immediately a difference was observed in the contact angle between the substrate and the droplet. The increased contact angle of the films prepared on quartz and graphene resulted in films with smaller diameters and greater film heights. This change in volume/surface area ratio resulted in different drying conditions which produced a multiphase composition throughout the film. Figure 7-14(a) shows the relatively homogenous reflection band parallel to the film edge which contrasts with the variation seen in the reflection bands of films prepared on quartz and graphene, Figure 7-14(b and c) respectively.

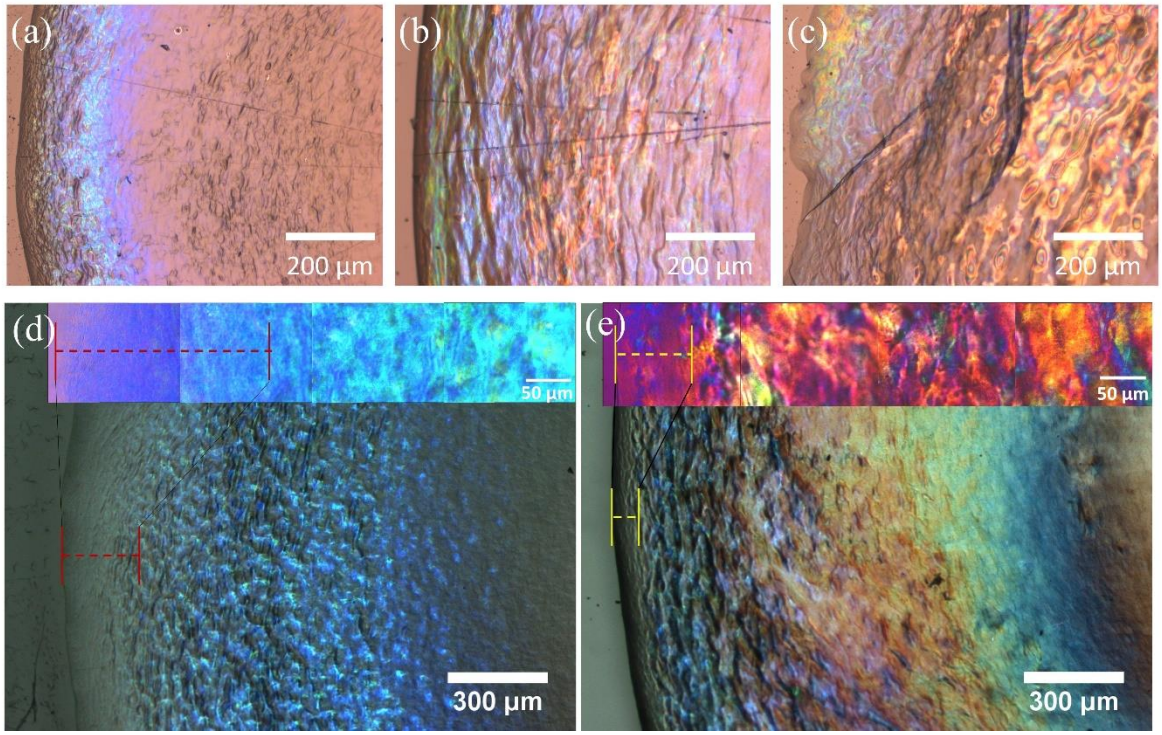

Figure 7-14 Light microscope images of the edge of CNC thin films prepared on glass (a) quartz (b) and graphene (c). Light microscope images showing the reflection of RHCP from films prepared on glass (d) and quartz (e). The inserts are respective POM images showing the phase composition of each film. The red and yellow scales highlight the correlation between reflection and change in phase composition.

The difference in phase composition between the film preapred on glass and the films prepared on quartz and graphene is seen more clearly in the POM images shown as inserts in Figure 7-14(d and e). The film prepared on quartz represents the graphene film which was excluded due to its poor reflection of CPL. The trend observed in the films prepared on glass where the reflection of RHCP correlates with a phase change is also seen in the film prepared on quartz and is highlighted in Figure 7-14(d and e) by the red and yellow sclae bars. The films prepared om glass showed no correlation betrween reflection and film

height. This was also the case for films prepared on quartz and graphene, evidence of which is presented in Figure 7-15. The peak reflections do not occur at peak film heights. Instead they appear to occur at specific CNC comcemtration/film height combinations. Spectroscopic techniques and polarised microscopy have confirmed that CPL is reflected by the film and that distinct and separate regions of the film reflect opposite hands of CPL. Associated with each region is a difference in phase composition, as conformed by POM analysis, and CNC concentration which has been confirmed by the spectroscopic technique developed by the author.

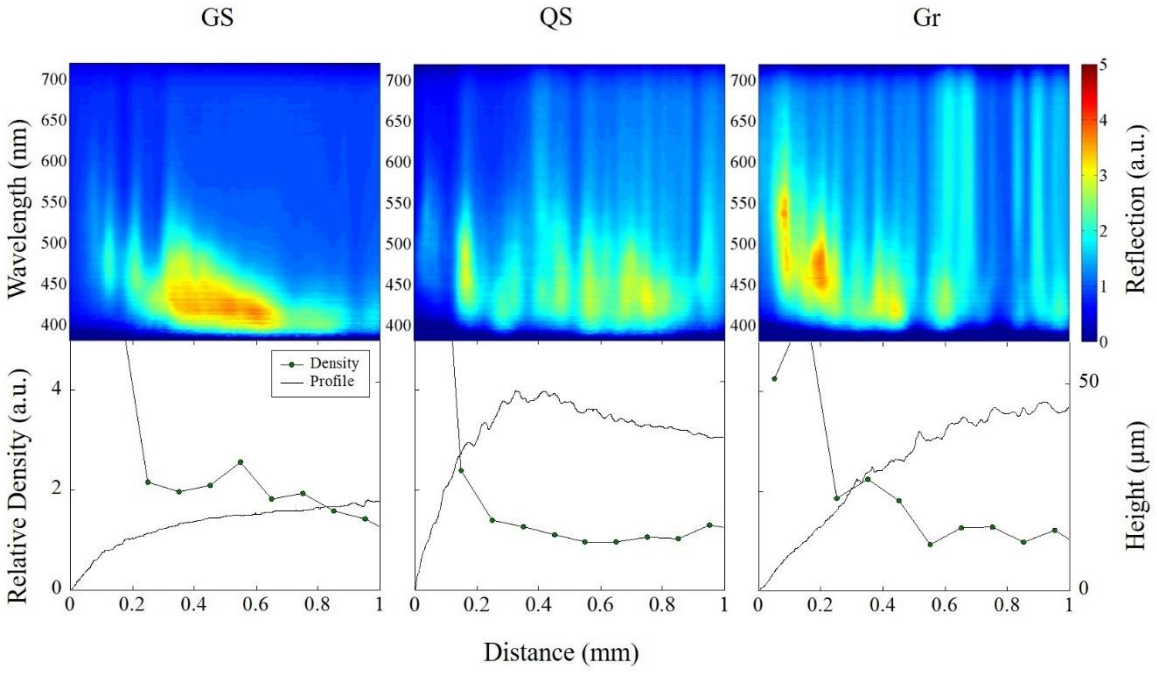

Figure 7-15 Top: Colour maps showing reflection as a function of distance from the edge of the films prepared on glass (GS), quartz (QS) and graphene (Gr). Bottom: The relative densities and profiles of each film below their respective colour map.

These investigations into CNC distribution have shown that progressing from the edge of the film towards the centre, the CNC concentration decreases and the film height increases. The increasing film height does not correlate with increasing reflection. Changes in optical behaviour have been observed, particularly a correlation between phase composition and the reflection of CPL. No visual confirmation of the structures responsible for the change in optical behaviour could be obtained but, one possibility is that defects are being introduced. The decreasing concentration of CNCs combined with the increasing film height could mean that defects are introduced to compensate. Defects are responsible for many of the useful properties found in everyday materials and are most likely responsible for the interesting phenomenon seen here.

7.5 Summary

To understand variation in optical behaviour of CNC EISA thin films a combination of techniques was employed to assess the radial distribution of CNCs within the film. This measurement required a known volume of the CNC EISA thin films which was achieved both theoretically and by experiment using profilometry. The volume was then used in conjunction with optical measurements to evaluate the distribution of CNCs along the diameter of the corresponding film. Differences in the nanocrystal concentration were found in regions expressing a significant difference in reflection of either LCP or RCP light. RCP light is shown to occur in a region of the film of low nanocrystal concentration and greater film height. The data also suggests that a concentration threshold may exist in EISA thin films, below which a CNC structure will tend toward inhomogeneity. POM analysis showed a clear difference in phase composition between the two reflecting

regions. The regions reflecting LCP light were homogenous whereas the RCP reflecting regions were inhomogeneous consisting of multiple phases. TEM analysis revealed the composition of the films which consisted of multilayers parallel to the film surface and base. The layered structure is homogenous and consistent throughout the film. Two types of defect were observed, phase boundaries which are believed to be produced because of tactoid coalescence during the EISA process. Discoid shaped regions that appear isotropic were also observed in one of the films. Structures responsible for the reflection of one handedness of CPL could be identified, but no variation in this structure that could have been responsible for the reflection of RCP was observed. Even though the results confirm reflection of both left and right CPL no other confirmation could be obtained on whether the structures possessed a right or a left handed chiral structure. It is assumed that a left structure reflects LCP light. A correlation of modelled and experimental data for the reflection of polarised and non-polarised light was presented and is well matched. Though an explanation of the structures responsible for the optical behaviour could not be presented here, the optical behaviour was correlated to variations in CNC distribution. LCP light was reflected from regions with a high concentration of CNCs and RCP is reflected from regions with low CNC concentrations.

Chapter 8 Conclusions

8.1 Main conclusions

The aim of this thesis was to develop structurally coloured films using CNCs. The approach considered was twofold, investigating the use of CNCs in an LbL regime to fabricate tunable structurally coloured thin films. The second aim explored the intrinsic ability of CNCs to self-assemble into chiral crystalline phases out of solution. The aim here was to understand how the drying mechanics of CNC droplets effects the distribution of CNC material within EISA thin films and identify any correlations between this and the films optical properties, looking specifically at the CPL response. Though the optical properties of cholesterics are well understood, the variation in the optical properties in CNC EISA thin films is not fully understood and this work contributes to understanding the obstacles faced in developing and achieving homogeneity in such films. Structurally coloured films have great potential as a sustainable and cost-effective alternative to

traditional forms of colouration and introduces a vivid iridescent colour palette to industries where aesthetics are important. The angle dependence of incident light and change in λ with pitch length means Bragg reflectors also have great potential for use in sensing and as optical filters. The specific optical profile of fabricated Bragg stacks will be difficult to mimic by other means, making them applicable to the security industry where they could be used as marks of authentication. Cellulose is also the most abundant and renewable material on earth which makes it an obvious choice where its properties can meet desired outcomes.

Investigations into the use of CNCs in an LbL regime saw the successful fabrication of thin multi-layered structurally coloured films. These films incorporated polyelectrolyte/clay and colloidal silica/cellulose nanocrystals that were applied by LbL deposition and the system was tuned to exhibit similar optical properties to the integument of the bright green iridescent South East Asian *C. rajah* beetle. The techniques used to tune the films have resulted in film outcomes matching the predicted behaviour. The films were fabricated by combining materials and controlling the deposition of layers to tune the RI and layer thicknesses. The structure within the films is a multi-layered system comprising layers of contrasting refractive index with thicknesses on the order of the wavelength of visible light. The fabricated films appear green and orange to the naked eye with peak reflections at 547 nm and 699 nm wavelengths respectively. The films are iridescent as the reflected wavelengths blue-shift with increasing incidence/viewing angle. The green film possesses a narrow reflectance band matching both the numerical model and the *C. rajah* beetle. The fabricated orange film possesses a reflectance band similar to the *C. rajah.* This band was broader due to the striations carved into the surface. It is assumed the film damage occurred during the washing process and possibly because inclusions were present in one

of the solutions used for this particular film as no other damage was observed in the other films. The advantage of fabricating films in this way is that the LbL technique is simple, can be applied to complex geometries, is open to a range of materials and can be expanded to a cost effective continuous process.

In order to understand CNC distribution in EISA thin films a novel technique was developed. For the first time, the distribution of CNCs across the diameter of EISA thin films was measured using this technique which involved spectroscopic analysis along film diameters. This measurement required a known volume of the CNC EISA thin films which was achieved both theoretically and by experiment using profilometry. The results of both the theoretical and experimental measurements are in good agreement with each other. The volume was then used in conjunction with optical measurements to evaluate the distribution of CNCs along the diameter of the corresponding film. The limitation of this method is that it only gives a relative concentration value. A reference would be needed to provide exact CNC concentration values.

A difference in the nanocrystal concentration has been shown to exist between regions expressing a significant difference in reflection of either LCP or RCP light. RCP light is shown to occur in a region of the film of low nanocrystal concentration and greater film height. The data also suggests that a concentration threshold may exist in EISA thin films, below which a CNC structure will tend toward inhomogeneity. Optical measurements showing significant reflection of both LCP and RCP light from separate regions within the same CNC thin films have been presented. This comes in contrast to the belief that only one polarisation of CPL can be reflected from a material that only forms a left handed chiral structure. POM analysis showed a clear difference in phase composition between the

two reflecting regions. The regions reflecting LCP light were homogenous whereas the RCP reflecting regions were inhomogeneous consisting of multiple phases. TEM analysis has revealed that the films are composed of multilayers parallel to the film surface and base. The layered structure is homogenous and consistent throughout the film. Two types of defect were observed, phase boundaries which are believed to be produced as a result of tactoid coalescence during the EISA process. Discoid shaped regions that appear isotropic were also observed in one of the films. Structures responsible for the reflection of one handedness of CPL could be identified, but no variation in this structure that could have been responsible for the reflection of RCP was observed. Even though the results confirm reflection of both left and right CPL no other confirmation could be obtained on whether the structures possessed a right or a left handed chiral structure. It is assumed that a left structure reflects LCP light. A correlation of modelled and experimental data for the reflection of polarised and non-polarised light was presented and is well matched. Though an explanation of the structures responsible for the optical behaviour could not be presented here, the optical behaviour was correlated to variations in CNC distribution. LCP light was reflected from regions with a high concentration of CNCs and RCP is reflected from regions with low CNC concentrations.

CNCs have shown great potential for producing structurally coloured films. The LbL process enables the fabrication of reproducible homogenous films and is open to modification which would be needed to facilitate the covering of larger substrates. One of the limitations of the technique is the need to wash between each dipping; the constant stream of water can erode certain areas where water build up is significant which on a larger substrate will become more significant. A spray up LbL process would be a good solution to this. The rapid nature of absorption onto the substrate limits the scope for

introducing structures that would give the films additional optical behaviours, an advantage of the EISA thin film. The slow assembly process that forms the chiral structures means a range of optical behaviours can be utilised. The difficulty however is controlling homogeneity over a specified area.

The relationship between CNC distribution and the CP response presented in this thesis, along with the use of CNCs in fabricating iridescent thin films contribute to the development of homogenous structurally coloured thin films. This work highlights the potential there is to design tailored optical thin films that are viable on an industrial scale using an abundant renewable material.

8.2 Future Work

This work presents a unique use for CNCs in structurally coloured thin films. It has also introduced a novel technique for investigating the distribution of CNCs in CNC EISA thin films. There are avenues future investigations could take to further develop, understand and explain these films and their potential.

The introduction of additional materials, such as melanin to mimic more closely the makeup of the beetle integument would serve to increase the RI disparity between the A and B layers. This increase in disparity could lead to an increase in the intensity of reflected light, but would need to be balanced with the increase in absorption the melanin would affect. Another area to explore is the functionalisation of CNCs with various functional groups to introduce beneficial properties. Functional groups such as coumarin and benzophenone may be grafted onto the surface of the CNCs; such molecules are

photoreactive and undergo radical-mediated reactions upon UV exposure[243,244]. These nanocomposites may increase the mechanical properties and reduce swelling of the films. The reduced swelling would be of particular advantage as VMT is a hygroscopic material.

Additional work may also include a thorough TEM investigation to measure pitch lengths at various intervals across the CNC EISA thin films. These would then be used to model reflection from a given section of film and then plotted with corresponding experimental reflection data to achieve a more complete characterisation of film reflectance. Further investigation into where exactly RCP is coming from within the CNC film would reveal specific regions that may be observable in TEM images of the corresponding cross sections. The use of a micrometre, adjustable in the vertical plane, will allow measurements of distance along the height of the film where RCP light reflection is best resolved and along the same z-axis where LCP is best resolved. Such a study will allow a more accurate identification of specific regions of the film where RCP is reflected from. This work will also be applied to films prepared on substrates which induce varying contact angles and affect the drying mechanics and CNC alignment across the film.

Another branch of work would include the modelling of defects in the twist of the chiral structure. Such defects are not easily identified using TEM analysis but have been shown to effect the polarisation state incident light[245,246]. As well as the twist defect, numerical modelling can assess whether an isotropic region in the continuous structure is responsible for a change in polarisation[238]. Understanding of such defects and their causes could pave a way for fabricated films with a broad range of tailored optical properties.

8.3 Publications

8.3.1 Papers

- HEWSON, D., VUKUSIC, P., EICHHORN, S. J. Reflection of Circularly Polarized Light and the effect of Particle Distribution on Circular Dichroism in Evaporation Induced Self-assembled Cellulose Nanocrystal Thin Films. AIP Advances 7, 065308 (2017).

- TZENG, P., HEWSON, D., VUKUSIC, P., EICHHORN, S. J., GRUNLAN, J. C., Bio-inspired iridescent layer-by-layer assembled cellulose nanocrystal Bragg stacks. Journal of Materials Chemistry C, 3, 4260-4264 (2015).

8.3.2 Oral Presentations

- HEWSON, D., TZENG, P., VUKUSIC, P., EICHHORN, S. J., GRUNLAN, J. C. Bio-inspired iridescent layer-by-layer assembled cellulose nanocrystal Bragg stacks. Technical Research Institute, Boras, Sweden (April 2016).

- S.J. Eichhorn, D.J. Hewson, P. Vukusic, J.C. Grunlan, P. Tzeng. Structural colour using cellulose nanofibers. Physical Aspects of Polymer Science, Manchester Institute of Biotechnology, Manchester, UK (September 2015).

- HEWSON, D., TZENG, P., VUKUSIC, P., EICHHORN, S. J., GRUNLAN, J. C. Bio-inspired iridescent layer-by-layer assembled cellulose nanocrystal Bragg stacks. 12th International Conference on Materials Chemistry (MC12) York, UK (July 2015).

- HEWSON, D., VUKUSIC, P., EICHHORN, S. J. Characterising Cellulose Nanocrystal Multilayer Reflectors. International Training School on Nanocrystalline Cellulose. Valencia, Spain (May 2014).

8.3.3 Poster Presentations

- HEWSON, D., VUKUSIC, P., EICHHORN, S. J. Circular Dichroism in Cellulose Nanocrystal self-assembled thin films. Living Light conference, Scripps Institute, San Diego, USA (May 2016).

- HEWSON, D., TZENG, P., VUKUSIC, P., EICHHORN, S. J., GRUNLAN, J. C. Bio-inspired iridescent layer-by-layer assembled cellulose nanocrystal Bragg stacks. Physics and Chemistry in Polysaccharide Science, Warsaw, Poland (October 2015).

- HEWSON, D., VUKUSIC, P., EICHHORN, S. J. Structural Ordering responsible for Iridescent Colour in Cellulose Nanocrystal Thin Films. Institute of Physics, London, UK (September 2014).

- HEWSON, D., VUKUSIC, P., EICHHORN, S. J. Structural Ordering and Self-assembly in Mesogenic Cellulose Nanocrystal Phases. Science and Uses of Nanocellulose & Cellulose Foams and Films, Biocomposites Centre, Bangor, UK (March 2014).

Appendix

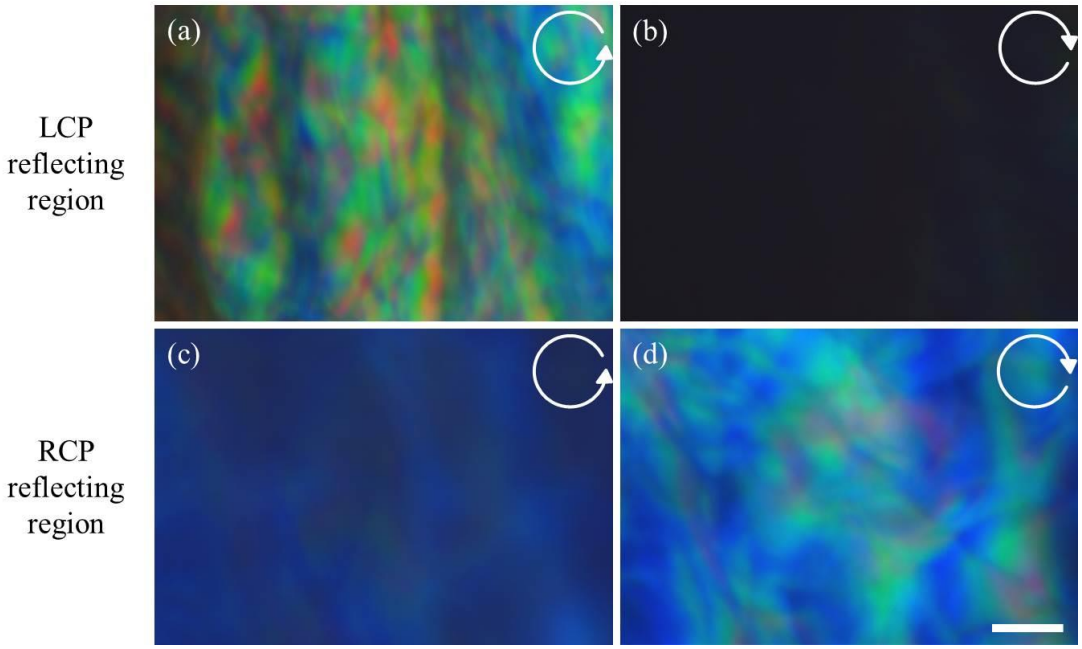

Figure A.1. High magnification MSP reflection of CPL from LCP (a,b) and RCP (c,d) reflecting regions. LCP reflection from an LCP reflecting region is clearly seen in (a) and no reflection is seen when illuminated with RCP (b). Reflection of LCP is seen from an RCP reflecting region (c), but is obscured by a stronger reflection of RCP (d).

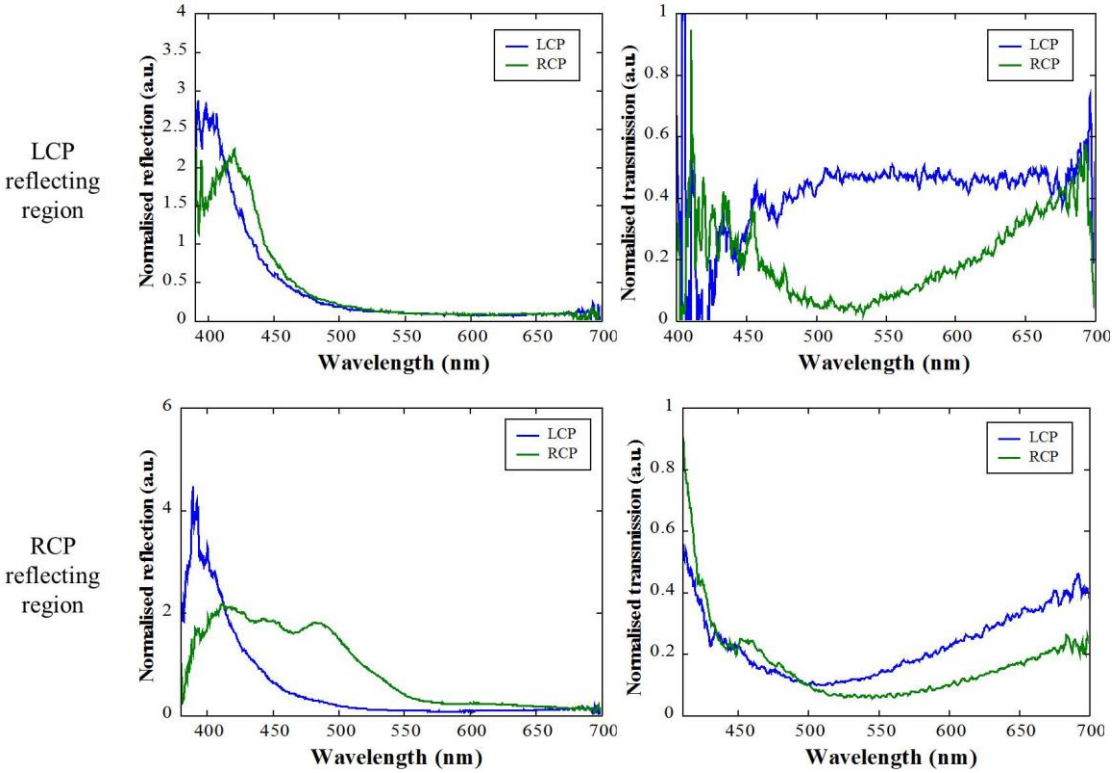

Figure A.2 Reflection and transmission spectra of LCP and RCP light from regions of the film where the reflection of LCP (top) and RCP (bottom) are dominant. The spectra recorded from the LCP reflecting region (top left) present data showing an almost equal intensity of reflected LCP and RCP light. The corresponding complimentary transmission is not seen. Instead LCP is more readily transmitted than RCP light (top right). Likewise from the RCP reflecting region, a dominant LCP light is reflected at greater intensity (bottom left) and very little difference is seen between the transmitted LCP and RCP light (bottom right).

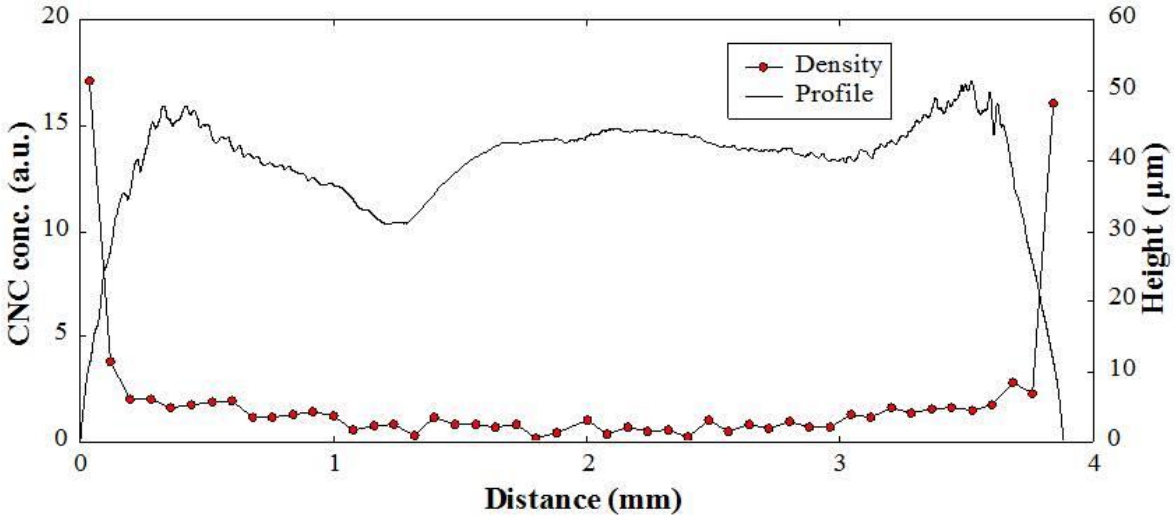

Figure A.3 A complete CNC distribution plot shown against the film profile the data is representing.

References

1. Bird, C. M., Berens, S. C., Horner, A. J. & Franklin, A. Categorical encoding of color in the brain. *Proc. Natl. Acad. Sci.* **111,** 4590–4595 (2014).

2. Jalil, N. A., Yunus, R. M. & Said, N. S. Environmental Colour Impact upon Human Behaviour: A Review. *Procedia - Soc. Behav. Sci.* **35,** 54–62 (2012).

3. Ho, H. N., Van Doorn, G. H., Kawabe, T., Watanabe, J. & Spence, C. Colour-temperature correspondences: When reactions to thermal stimuli are influenced by colour. *PLoS One* **9,** 1–7 (2014).

4. Chebat, J.-C. & Morrin, M. Colors and cultures: Exploring the effects of mall décor on consumer perceptions. *J. Bus. Res.* **60,** 189–196 (2007).

5. Ainsworth, R. A. Effects of Three Colors in an Office Interior on Mood and Performance ’. (1993).

6. Taylor, M. I., Turner, G. F., Robinson, R. L. & Stauffer Jr, J. R. Sexual selection, parasites and bower height skew in a bower-building cichlid fish. *Anim. Behav.* **56,** 379–384 (1998).

7. Wiklund, C. & Jarvi, T. Survival of Distasteful Insects After Being Attacked by Naive Birds: A Reappraisal of the Theory of Aposematic Coloration Evolving Through Individual Selection. *Evolution (N. Y).* **36,** 998 (1982).

8. Srinivasarao, M. Nano-optics in the biological world: beetles, butterflies, birds, and moths. *Chem. Rev.* (1999).

9. Mason, C. W. Iridescent Colors. *J. Phys. Chem.* **31,** 321–354 (1927).

10. Vukusic, P. & Sambles, J. Photonic structures in biology. *Nature* **424,** (2003).

11. Parker, A. R., McKenzie, D. R. & Large, M. C. J. Multilayer reflectors in animals using green and gold beetles as contrasting examples. *J. Exp. Biol.* **201,** 1307–1313 (1998).

12. Mcdonald, L. T., Finlayson, E. D., Wilts, B. D., Vukusic, P. & Mcdonald, L. T. Circularly polarized reflection from the scarab beetle Chalcothea smaragdina : light scattering by a dual photonic structure. (2017).

13. Seago, A. E., Brady, P., Vigneron, J.-P. & Schultz, T. D. Gold bugs and beyond: a review of iridescence and structural colour mechanisms in beetles (Coleoptera). *J. R. Soc. Interface* **6,** S165–S184 (2009).

14. Vukusic, P., Sambles, J. R., Lawrence, C. R. & Wootton, R. J. Quantified interference and diffraction in single Morpho butterfly scales. *Proc. R. Soc. B Biol. Sci.* **266,** 1403 (1999).

15. Ghiradella, H. Light and Color on the Wing: Structural colors in Butterflies and

Moths. *Appl. Opt.* **30,** 3492–3500 (1991).

16. Mason, C. W. Structural Colors in Feathers I. 201–251 (1923).

17. Noyes, J. a., Vukusic, P. & Hooper, I. R. Experimental method for reliably establishing the refractive index of buprestid beetle exocuticle. *Opt. Express* **15,** 4351 (2007).

18. Mouchet, S. R. *et al.* Controlled fluorescence in a beetle's photonic structure and its sensitivity to environmentally induced changes. *Proc. R. Soc. B Biol. Sci.* **283,** 20162334 (2016).

19. Lagerwall, J. P. F. *et al.* Cellulose nanocrystal-based materials: from liquid crystal self-assembly and glass formation to multifunctional thin films. *NPG Asia Mater.* **6,** e80 (2014).

20. Land, M. F. The physics and biology of animal reflectors. *Prog. Biophys. Mol. Biol.* **24,** 75–106 (1972).

21. Haque, M. A., Kurokawa, T. & Gong, J. P. Anisotropic hydrogel based on bilayers: color, strength, toughness, and fatigue resistance. *Soft Matter* **8,** 8008 (2012).

22. Ghazzal, M. N. *et al.* Tailored refractive index of inorganic mesoporous mixed-oxide Bragg stacks with bio-inspired hygrochromic optical properties. *J. Mater. Chem. C* **1,** 6202 (2013).

23. Deparis, O. *et al.* Theoretical condition for transparency in mesoporous layered optical media: Application to switching of hygrochromic coatings. *Appl. Phys. Lett.* **104,** 4–7 (2014).

24. Kurt, P. *et al.* Structural color via layer-by-layer deposition: layered nanoparticle arrays with near-UV and visible reflectivity bands. *J. Mater. Chem.* **19,** 8920 (2009).

25. Kreysing, M. *et al.* Photonic Crystal Light Collectors in Fish Retina Improve Vision in Turbid Water. *Science (80-.).* **336,** 1700–1703 (2012).

26. Allen, N. S. *et al.* Behaviour of nanoparticle (ultrafine) titanium dioxide pigments and stabilisers on the photooxidative stability of water based acrylic and isocyanate based acrylic coatings. *Polym. Degrad. Stab.* **78,** 467–478 (2002).

27. Lachheb, H. *et al.* Photocatalytic degradation of various types of dyes (Alizarin S, Crocein Orange G, Methyl Red, Congo Red, Methylene Blue) in water by UV-irradiated titania. *Appl. Catal. B Environ.* **39,** 75–90 (2002).

28. Mouchet, S. R. *et al.* Photonic scales of Hoplia coerulea beetle: any colour you like. *Mater. Today Proc.* **4,** 4979–4986 (2017).

29. Barhoum, M., Morrill, J. M., Riassetto, D. & Bartl, M. H. Rapid Sol–Gel Fabrication of High-Quality Thin-Film Stacks on Planar and Curved Substrates. *Chem. Mater.* **23,** 5177–5184 (2011).

30. Podsiadlo, P. *et al.* Layer-by-layer assembled films of cellulose nanowires with

antireflective properties. *Langmuir* **23,** 7901–6 (2007).

31. Eichhorn, S. J. *et al.* Cellulose nanowhiskers: promising materials for advanced applications. *Soft Matter* **7,** 303–315 (2011).

32. Habibi, Y., Lucia, L. a & Rojas, O. J. Cellulose nanocrystals: chemistry, self-assembly, and applications. *Chem. Rev.* **110,** 3479–500 (2010).

33. Revol, J. F., Bradford, H., Giasson, J., Marchessault, R. H. & Gray, D. G. Helicoidal self-ordering of cellulose microfibrils in aqueous suspension. *Int. J. Biol. Macromol.* **14,** 170–2 (1992).

34. Parker, R. M. *et al.* Hierarchical Self-assembly of Cellulose Nanocrystals in a Confined Geometry. *ACS Nano* accepted (2016). doi:10.1021/acsnano.6b03355

35. Guidetti, G., Atifi, S., Vignolini, S. & Hamad, W. Y. Flexible Photonic Cellulose Nanocrystal Films. *Adv. Mater.* **28,** 10042–10047 (2016).

36. Espinha, A. *et al.* Shape Memory Cellulose-Based Photonic Reflectors. *ACS Appl. Mater. Interfaces* **8,** 31935–31940 (2016).

37. Conley, K., Whitehead, M. A. & van de Ven, T. G. M. Probing the structural chirality of crystalline cellulose with induced circular dichroism. *Cellulose* **24,** 1–8 (2016).

38. Usov, I. *et al.* Understanding nanocellulose chirality and structure-properties relationship at the single fibril level. *Nat. Commun.* **6,** 7564 (2015).

39. Majoinen, J., Kontturi, E., Ikkala, O. & Gray, D. G. SEM imaging of chiral nematic films cast from cellulose nanocrystal suspensions. *Cellulose* **19,** 1599–1605 (2012).

40. de Vries, H. Rotatory power and other optical properties of certain liquid crystals. *Acta Crystallogr.* **4,** 219–226 (1951).

41. Kelly, J. A. *et al.* Responsive Photonic Hydrogels Based on Nanocrystalline Cellulose. *Angew. Chemie Int. Ed.* **52,** 8912–8916 (2013).

42. Dumanli, A. G. *et al.* Digital color in cellulose nanocrystal films. *ACS Appl. Mater. Interfaces* **6,** 12302–6 (2014).

43. Edgar, C. D. & Gray, D. G. Induced Circular Dichroism of Chiral Nematic Cellulose Films. *Cellulose* **8,** 5–12 (2001).

44. Cheung, C. C. Y., Giese, M., Kelly, J. a., Hamad, W. Y. & MacLachlan, M. J. Iridescent Chiral Nematic Cellulose Nanocrystal/Polymer Composites Assembled in Organic Solvents. *ACS Macro Lett.* **2,** 1016–1020 (2013).

45. Tyndall, J. On the Blue Colour of the Sky , the Polarization of Skylight , and on the Polarization of Light by Cloudy Matter Generally Author (s): John Tyndall Source : Proceedings of the Royal Society of London , Vol . 17 (1868 - 1869), pp . 223-233 Published by. in *The Royal Society* **17,** 223–233 (1869).

46. Fox, D. L. *Animal Biochromes*. (Cambridge University Press, 1953).

47. Strutt, J. *Scientific Papers*. (Cambridge University Press, 1899).

48. Haar, D. . Ter. *The Old Quantum Theory*. (Pergamon Press, 1967).

49. Mason, C. W. Structural Colors in Insects. I. *J. Phys. Chem.* **30,** 383–395 (1925).

50. Stavenga, D. G., Wilts, B. D., Leertouwer, H. L. & Hariyama, T. Polarized iridescence of the multilayered elytra of the Japanese jewel beetle, Chrysochroa fulgidissima. *Philos. Trans. R. Soc. London B Biol. Sci.* **366,** (2011).

51. Neville, A. C. & Caveney, S. Scarabaeid beetle exocuticle as an optical analogue of cholesteric liquid crystals. *Biol. Rev. Camb. Philos. Soc.* **44,** 531–62 (1969).

52. Caveney, S. Cuticle Reflectivity and Optical Activity in Scarab Beetles: The Role of Uric Acid. *Proc. R. Soc. London B Biol. Sci.* **178,** (1971).

53. Kolle, M. *Photonic Structures Inspired by Nature*. (Springer Science & Business Media, 2011).

54. Prum, R. O., Quinn, T. & Torres, R. H. Anatomically diverse butterfly scales all produce structural colours by coherent scattering. *J. Exp. Biol.* **209,** 748–65 (2006).

55. Vukusic, P. & Stavenga, D. G. Physical methods for investigating structural colours in biological systems. *J. R. Soc. Interface* **6 Suppl 2,** S133-48 (2009).

56. D'Alba, L. *et al.* Colour-producing β-keratin nanofibres in blue penguin (Eudyptula minor) feathers. *Biol. Lett.* **7,** 543–6 (2011).

57. Prum, R. O. & Torres, R. Structural colouration of avian skin: convergent evolution of coherently scattering dermal collagen arrays. *J. Exp. Biol.* **206,** 2409–29 (2003).

58. Denton, E. Reflectors in fishes. *Sci. Am.* **1,** (96-104) (1971).

59. Kolle, M. *Bio-inspired multifunctional photonic systems*.

60. Mäthger, L. M., Land, M. F., Siebeck, U. E. & Marshall, N. J. Rapid colour changes in multilayer reflecting stripes in the paradise whiptail, Pentapodus paradiseus. *J. Exp. Biol.* **206,** 3607–3613 (2003).

61. Vinther, J., Briggs, D. E. G., Prum, R. O. & Saranathan, V. The colour of fossil feathers. *Biol. Lett.* **4,** 522–5 (2008).

62. Vinther, J., Briggs, D. E. G., Clarke, J., Mayr, G. & Prum, R. O. Structural coloration in a fossil feather. *Biol. Lett.* **6,** 128–31 (2010).

63. Fernandes, S. N. *et al.* Structural Color and Iridescence in Transparent Sheared Cellulosic Films. *Macromol. Chem. Phys.* **214,** 25–32 (2013).

64. Saranathan, V. *et al.* Structure, function, and self-assembly of single network gyroid (I4132) photonic crystals in butterfly wing scales. *Proc. Natl. Acad. Sci.* **107,** 11676–11681 (2010).

65. Dolan, J. A. *et al.* Optical Properties of Gyroid Structured Materials: From Photonic

Crystals to Metamaterials. *Adv. Opt. Mater.* **3,** 12–32 (2015).

66. Mossakowski, D. Reflection Measurements Used In The Analysis Of Structural Colours Of Beetles. *J. Microsc.* **116,** 351–364 (1979).

67. Kurachi, M., Takaku, Y., Komiya, Y. & Hariyama, T. The origin of extensive colour polymorphism in Plateumaris sericea (Chrysomelidae, Coleoptera). *Naturwissenschaften* **89,** 295–8 (2002).

68. Noyes, J. A. Experimental Techniques for the Study of Natural Photonic Structures. (University of Exeter, 2008).

69. Yoshioka, S. & Kinoshita, S. Effect of Macroscopic Structure in Iridescent Color of the Peacock Feathers. *Orig. Pap. Forma* **17,** 169–181 (2002).

70. Pol Vigneron, J., Colomer, J.-F., Rassart, M., Ingram, A. L. & Lousse, V. Structural origin of the colored reflections from the black-billed magpie feathers. *Phys. Rev. E* **73,** 21914 (2006).

71. Deparis, O. & Vigneron, J. P. Modeling the photonic response of biological nanostructures using the concept of stratified medium: The case of a natural three-dimensional photonic crystal. *Mater. Sci. Eng. B* **169,** 12–15 (2010).

72. Michielsen, K., De Raedt, H. & Stavenga, D. G. Reflectivity of the gyroid biophotonic crystals in the ventral wing scales of the Green Hairstreak butterfly, Callophrys rubi. *J. R. Soc. Interface* **7,** 765–71 (2010).

73. Pouya, C., Stavenga, D. G. & Vukusic, P. Discovery of ordered and quasi-ordered photonic crystal structures in the scales of the beetle Eupholus magnificus. *Opt. Express* **19,** 11355 (2011).

74. Wilts, B. D., Michielsen, K., Kuipers, J., De Raedt, H. & Stavenga, D. G. Brilliant camouflage: photonic crystals in the diamond weevil, Entimus imperialis. *Proceedings. Biol. Sci.* **279,** 2524–30 (2012).

75. Mouchet, S., Vigneron, J.-P., Colomer, J.-F. & Deparis, O. Modeling Additive Color Effect in Natural Photonic Polycrystals Using the Layer Homogenization Method: The Case of the Diamond Weevil. in 541–542 (Springer, Dordrecht, 2015). doi:10.1007/978-94-017-9133-5_60

76. Ghiradella, H. Structure of butterfly scales: Patterning in an insect cuticle. *Microsc. Res. Tech.* **27,** 429–438 (1994).

77. Kertész, K. *et al.* Gleaming and dull surface textures from photonic-crystal-type nanostructures in the butterfly *Cyanophrys remus*. *Phys. Rev. E* **74,** 21922 (2006).

78. Michielsen, K. & Stavenga, D. G. Gyroid cuticular structures in butterfly wing scales: biological photonic crystals. *J. R. Soc. Interface* **5,** 85–94 (2008).

79. Saranathan, V. *et al.* Structure, function, and self-assembly of single network gyroid (I4132) photonic crystals in butterfly wing scales. *Proc. Natl. Acad. Sci. U. S. A.* **107,** 11676–81 (2010).

80. Shawkey, M. D. *et al.* Electron tomography, three-dimensional Fourier analysis and colour prediction of a three-dimensional amorphous biophotonic nanostructure. *J. R. Soc. Interface* **6 Suppl 2,** S213-20 (2009).

81. Kamita, G., Kolle, M., Huang, F. & Baumberg, J. J. Multilayer mirrored bubbles with spatially-chirped and elastically-tuneable optical bandgaps Abstract : **20,** 4430–4434 (2012).

82. Kolle, M. *et al.* Bio-inspired band-gap tunable elastic optical multilayer fibers. *Adv. Mater.* **25,** 2239–45 (2013).

83. Hsueh, H.-Y. *et al.* Inorganic Gyroid with Exceptionally Low Refractive Index from Block Copolymer Templating. *Nano Lett.* **10,** 4994–5000 (2010).

84. Augustine Urbas, Yoel Fink, and & Thomas*, E. L. One-Dimensionally Periodic Dielectric Reflectors from Self-Assembled Block Copolymer−Homopolymer Blends. (1999). doi:10.1021/MA9903207

85. Urbas, A. *et al.* Tunable Block Copolymer/Homopolymer Photonic Crystals**. *Adv. Mater* **12,** (2000).

86. Osuji, C., Chao, C.-Y., Bita, I., Ober, C. K. & Thomas, E. L. Temperature-Dependent Photonic Bandgap in a Self-Assembled Hydrogen-Bonded Liquid-Crystalline Diblock Copolymer. *Adv. Funct. Mater.* **12,** 753–758 (2002).

87. Sveinbjörnsson, B. R. *et al.* Rapid self-assembly of brush block copolymers to photonic crystals. *Proc. Natl. Acad. Sci. U. S. A.* **109,** 14332–6 (2012).

88. Lohmüller, T., Helgert, M., Sundermann, M., Brunner, R. & Spatz, J. P. Biomimetic Interfaces for High-Performance Optics in the Deep-UV Light Range. *Nano Lett.* **8,** 1429–1433 (2008).

89. Li, X., Gao, J., Xue, L. & Han, Y. Porous Polymer Films with Gradient-Refractive-Index Structure for Broadband and Omnidirectional Antireflection Coatings. *Adv. Funct. Mater.* **20,** 259–265 (2010).

90. Päivänranta, B. *et al.* Nanofabrication of Broad-Band Antireflective Surfaces Using Self-Assembly of Block Copolymers. *ACS Nano* **5,** 1860–1864 (2011).

91. Hecht, E. Optics. in (ed. Spatz, B.) 346–349 (Addison-Wesley, 1987).

92. Macleod, H. A. (Hugh A. *Thin-film optical filters*. (Institute of Physics Pub, 2001).

93. Starkey, T. A. & Vukusic, P. Light manipulation principles in biological photonic systems. *Nanophotonics Rev.* 1–49

94. Heavens, O. S. Optical properties of thin films. *Reports Prog. Phys.* **23,** 301 (1960).

95. Joannopoulos, J. D., Johnson, S. G., Winn, J. N. & Meade, R. D. *Photonic crystalsMolding the flow of light*. (Princeton University Press, 2008).

96. Mahlein, H. F. Generalized Brewster-angle conditions for quarter-wave multilayers at non-normal incidence. *J. Opt. Soc. Am.* **64,** 647 (1974).

97. Sheppard, C. J. R. Approximate calculation of the reflection coefficient from a stratified medium. *Pure Appl. Opt. J. Eur. Opt. Soc. Part A* **4,** 665–669 (1995).

98. Stewart, G. W. X-Ray Diffraction in Liquids. *Rev. Mod. Phys.* **2,** 116–122 (1930).

99. Bernal, J. D. & Mason, J. Packing of Spheres: Co-ordination of Randomly Packed Spheres. *Nature* **188,** 910–911 (1960).

100. Donald, A., Windle, A. & Hanna, S. *Liquid Crystalline Polymers*. (Cambridge University Press, 2006).

101. Chandrasekhar, S. *Liquid Crystals*. (Cambridge University Press, 1980).

102. Roman, M. & Gray, D. G. Parabolic focal conics in self-assembled solid films of cellulose nanocrystals. *Langmuir* **21,** 5555–61 (2005).

103. Jones, R. C. A New Calculus for the Treatment of Optical SystemsI Description and Discussion of the Calculus. *J. Opt. Soc. Am.* **31,** 488 (1941).

104. Foster, D. H. Chromatic Function of the Cones. in *Reference Module in Neuroscience and Biobehavioral Psychology* (2017). doi:10.1016/B978-0-12-809324-5.01324-9

105. Wyman, C., Sloan, P.-P. & Shirley, P. Simple Analytic Approximations to the CIE XYZ Color Matching Functions. *J. Comput. Graph. Tech.* **2,** 1–11 (2013).

106. Fairman, H. S., Brill, M. H. & Hemmendinger, H. How the CIE 1931 color-matching functions were derived from Wright-Guild data. *Color Res. Appl.* **22,** 11–23 (1997).

107. Brill, M. H. How the CIE 1931 color-matching functions were derived from Wright-Guild data. *Color Res. Appl.* **23,** 259–259 (1998).

108. Preston, R. D. *Fibre Structure*. (Elsevier, 2013).

109. Richmond, T. Higher plant cellulose synthases. *Genome Biol.* **1,** REVIEWS3001 (2000).

110. Doblin, M. S. Cellulose Biosynthesis in Plants: from Genes to Rosettes. *Plant Cell Physiol.* **43,** 1407–1420 (2002).

111. Albersheim, P., Darvill, A., Roberts, K., Sederoff, R. & Staehelin, A. Plant cell walls. From chemistry to biology. *Ann. Bot.* **108,** viii–ix (2011).

112. Delmer, D. P. & Amor, Y. Cellulose biosynthesis. *Plant Cell* **7,** 987–1000 (1995).

113. Morehead, F. F. Ultrasonic Disintegration of Cellulose Fibers Before and After Acid Hydrolysis. *Text. Res. J.* **20,** 549–553 (1950).

114. Rånby, B. G., Banderet, A. & Sillén, L. G. Aqueous Colloidal Solutions of Cellulose Micelles. *Acta Chem. Scand.* **3,** 649–650 (1949).

115. Rånby, B. G. Fibrous macromolecular systems. Cellulose and muscle. The colloidal

properties of cellulose micelles. *Discuss. Faraday Soc.* **11,** 158–164 (1951).

116. Mukherjee, S. M. & Woods, H. J. X-ray and electron microscope studies of the degradation of cellulose by sulphuric acid. *Biochim. Biophys. Acta* **10,** 499–511 (1953).

117. Marchessault, R. H., Morehead, F. F. & Walter, N. M. Liquid Crystal Systems from Fibrillar Polysaccharides. *Nature* **184,** 632–633 (1959).

118. Revol, J.-F. & Marchessault, R. H. In vitro chiral nematic ordering of chitin crystallites. *Int. J. Biol. Macromol.* **15,** 329–335 (1993).

119. Elazzouzi-Hafraoui, S. *et al.* The shape and size distribution of crystalline nanoparticles prepared by acid hydrolysis of native cellulose. *Biomacromolecules* **9,** 57–65 (2008).

120. Araki, J., Wada, M., Kuga, S. & Okano, T. Birefringent glassy phase of a cellulose microcrystal suspension. *Langmuir* **16,** 2413–2415 (2000).

121. Beck, S., Méthot, M. & Bouchard, J. General procedure for determining cellulose nanocrystal sulfate half-ester content by conductometric titration. *Cellulose* **22,** 101–116 (2015).

122. Abitbol, T., Kloser, E. & Gray, D. G. Estimation of the surface sulfur content of cellulose nanocrystals prepared by sulfuric acid hydrolysis. *Cellulose* **20,** 785–794 (2013).

123. Saito, T., Kimura, S., Nishiyama, Y. & Isogai, A. Cellulose nanofibers prepared by TEMPO-mediated oxidation of native cellulose. *Biomacromolecules* **8,** 2485–91 (2007).

124. Isogai, A., Saito, T. & Fukuzumi, H. TEMPO-oxidized cellulose nanofibers. *Nanoscale* **3,** 71–85 (2011).

125. Chen, H. *Biotechnology of lignocellulose: Theory and practice*. *Biotechnology of Lignocellulose: Theory and Practice* (2014). doi:10.1007/978-94-007-6898-7

126. Conley, K., Godbout, L., Whitehead, M. A. & Van De Ven, T. G. M. Origin of the twist of cellulosic materials. *Carbohydr. Polym.* **135,** 285–299 (2016).

127. Lu, P. & Hsieh, Y.-L. Preparation and properties of cellulose nanocrystals: Rods, spheres, and network. *Carbohydr. Polym.* **82,** 329–336 (2010).

128. Beck, S., Bouchard, J. & Berry, R. Dispersibility in Water of Dried Nanocrystalline Cellulose. *Biomacromolecules* **13,** 1486–1494 (2012).

129. Lu, P. & Hsieh, Y.-L. Preparation and characterization of cellulose nanocrystals from rice straw. *Carbohydr. Polym.* **87,** 564–573 (2012).

130. Wang, Q. Q. *et al.* Approaching zero cellulose loss in cellulose nanocrystal (CNC) production: recovery and characterization of cellulosic solid residues (CSR) and CNC. *Cellulose* **19,** 2033–2047 (2012).

131. Sacui, I. A. *et al.* Comparison of the Properties of Cellulose Nanocrystals and Cellulose Nanofibrils Isolated from Bacteria, Tunicate, and Wood Processed Using Acid, Enzymatic, Mechanical, and Oxidative Methods. *ACS Appl. Mater. Interfaces* **6,** 6127–6138 (2014).

132. Sugiyama, J., Vuong, R. & Chanzy, H. Electron diffraction study on the two crystalline phases occurring in native cellulose from an algal cell wall. *Macromolecules* **24,** 4168–4175 (1991).

133. George, J. & Sabapathi, S. N. Cellulose nanocrystals: synthesis, functional properties, and applications. *Nanotechnol. Sci. Appl.* **8,** 45–54 (2015).

134. Zhao, Y. & Li, J. Excellent chemical and material cellulose from tunicates: diversity in cellulose production yield and chemical and morphological structures from different tunicate species. *Cellulose* **21,** 3427–3441 (2014).

135. Sakurada, I., Nukushina, Y. & Ito, T. Experimental determination of the elastic modulus of crystalline regions in oriented polymers. *J. Polym. Sci.* **57,** 651–660 (1962).

136. Nishino, T., Takano, K. & Nakamae, K. Elastic modulus of the crystalline regions of cellulose polymorphs. *J. Polym. Sci. Part B Polym. Phys.* **33,** 1647–1651 (1995).

137. Diddens, I., Murphy, B., Krisch, M. & Müller, M. Anisotropic Elastic Properties of Cellulose Measured Using Inelastic X-ray Scattering. *Macromolecules* **41,** 9755–9759 (2008).

138. Tashiro, K. & Kobayashi, M. Theoretical evaluation of three-dimensional elastic constants of native and regenerated celluloses: role of hydrogen bonds. *Polymer (Guildf).* **32,** 1516–1526 (1991).

139. Malin Bergenstråhle, †, Lars A. Berglund, † and & Karim Mazeau*, ‡. Thermal Response in Crystalline Iβ Cellulose: A Molecular Dynamics Study. (2007). doi:10.1021/JP072258I

140. Eichhorn, S. J. & Davies, G. R. Modelling the crystalline deformation of native and regenerated cellulose. *Cellulose* **13,** 291–307 (2006).

141. Šturcová, A., Davies, G. R. & Eichhorn, S. J. Elastic Modulus and Stress-Transfer Properties of Tunicate Cellulose Whiskers. *Biomacromolecules* **6,** 1055–1061 (2005).

142. Hamad, W. Y. & Eichhorn, S. Deformation Micromechanics of Regenerated Cellulose Fibers Using Raman Spectroscopy. *J. Eng. Mater. Technol.* **119,** 309 (1997).

143. Rusli, R. & Eichhorn, S. J. Determination of the stiffness of cellulose nanowhiskers and the fiber-matrix interface in a nanocomposite using Raman spectroscopy. *Appl. Phys. Lett.* **93,** 33111 (2008).

144. Iwamoto, S., Kai, W., Isogai, A. & Iwata, T. Elastic Modulus of Single Cellulose Microfibrils from Tunicate Measured by Atomic Force Microscopy.

Biomacromolecules **10,** 2571–2576 (2009).

145. Revol, J.-F. *et al.* Chiral nematic suspensions of cellulose crystallites; phase separation and magnetic field orientation. *Liquid Crystals* **16,** 127–134 (1994).

146. Vafaei, S. *et al.* Effect of nanoparticles on sessile droplet contact angle. *Nanotechnology* **17,** 2523–2527 (2006).

147. Kuncicky, D. M. & Velev, O. D. Surface-Guided Templating of Particle Assemblies Inside Drying Sessile Droplets†. (2007). doi:10.1021/LA702129B

148. Mu, X. & Gray, D. G. Droplets of cellulose nanocrystal suspensions on drying give iridescent 3-D 'coffee-stain' rings. *Cellulose* **22,** 1103–1107 (2015).

149. Haywood Virginia A Davis, A. D. Effects of liquid crystalline and shear alignment on the optical properties of cellulose nanocrystal films. *Cellulose* (2016). doi:10.1007/s10570-016-1150-4

150. Liu, D. *et al.* Structure–color mechanism of iridescent cellulose nanocrystal films. *RSC Adv.* **4,** 39322 (2014).

151. Effect of thickness on the structural, optical and electrical properties of thermally evaporated PbI2 thin films | haider abbas - Academia.edu. Available at: http://www.academia.edu/2531956/Effect_of_thickness_on_the_structural_optical_and_electrical_properties_of_thermally_evaporated_PbI2_thin_films. (Accessed: 24th July 2014)

152. Larson, R. G. Transport and deposition patterns in drying sessile droplets. *AIChE J.* **60,** 1538–1571 (2014).

153. Davidson, Z. S. *et al.* Deposition and drying dynamics of liquid crystal droplets. *Nat. Commun.* **8,** 15642 (2017).

154. Yunker, P. J., Still, T., Lohr, M. A. & Yodh, A. G. Suppression of the coffee-ring effect by shape-dependent capillary interactions. *Nature* **476,** 308–11 (2011).

155. Hu, H. & Larson, R. G. Evaporation of a Sessile Droplet on a Substrate. (2002). doi:10.1021/JP0118322

156. Deegan, R., Bakajin, O., Dupont, T. & Huber, G. Capillary flow as the cause of ring stains from dried liquid drops. *Nature* 827–829 (1997).

157. Munshi, A. M., Singh, V. N., Kumar, M. & Singh, J. P. Effect of nanoparticle size on sessile droplet contact angle. *J. Appl. Phys.* **103,** (2008).

158. Hu, H. & Larson, R. G. Analysis of the Microfluid Flow in an Evaporating Sessile Droplet. (2005). doi:10.1021/LA047528S

159. Deegan, R. D. *et al.* Contact line deposits in an evaporating drop. *Phys. Rev. E* **62,** 756–765 (2000).

160. Yoshitsugu, K. & Ueno, I. Effect of suspended particles on spreading of volatile droplet on solid substrate. *J. Vis.* **14,** 285–294 (2011).

161. Deegan, R. D. *et al.* Capillary flow as the cause of ring stains from dried liquid drops. *Nature* **389,** 827–829 (1997).

162. Deegan, R. D. Pattern formation in drying drops. *Phys. Rev. E* **61,** 475–485 (2000).

163. Berteloot, G. *et al.* Evaporation of a sessile droplet: Inside the coffee stain. *J. Colloid Interface Sci.* **370,** 155–161 (2012).

164. Bigioni, T. P. *et al.* Kinetically driven self assembly of highly ordered nanoparticle monolayers. *Nat. Mater.* **5,** 265–270 (2006).

165. Kaya, D., Belyi, V. A. & Muthukumar, M. Pattern formation in drying droplets of polyelectrolyte and salt. *J. Chem. Phys.* **133,** 114905 (2010).

166. Loudet, J. C., Alsayed, A. M., Zhang, J. & Yodh, A. G. Capillary Interactions Between Anisotropic Colloidal Particles. *Phys. Rev. Lett.* **94,** 18301 (2005).

167. Loudet, J.-C., Yodh, A. G. & Pouligny, B. Wetting and Contact Lines of Micrometer-Sized Ellipsoids. (2006). doi:10.1103/PhysRevLett.97.018304

168. Madivala, B., Vandebril, S., Fransaer, J. & Vermant, J. Exploiting particle shape in solid stabilized emulsions. *Soft Matter* **5,** 1717 (2009).

169. Mashkour, M., Kimura, T., Kimura, F., Mashkour, M. & Tajvidi, M. Tunable Self-Assembly of Cellulose Nanowhiskers and Polyvinyl Alcohol Chains Induced by Surface Tension Torque. *Biomacromolecules* (2013). doi:10.1021/bm401287s

170. Peiss, C. N. Evaporation of small water drops maintained at constant volume. *J. Appl. Phys.* **65,** 5235 (1989).

171. Wang, P.-X., Hamad, W. Y. & MacLachlan, M. J. Structure and transformation of tactoids in cellulose nanocrystal suspensions. *Nat. Commun.* **7,** 11515 (2016).

172. Hanley, S. J., Revol, J.-F., Godbout, L. & Gray, D. G. Atomic force microscopy and transmission electron microscopy of cellulose from Micrasterias denticulata; evidence for a chiral helical microfibril twist. *Cellulose* **4,** 209–220 (1997).

173. Wilts, B. D., Dumanli, A. G., Middleton, R., Vukusic, P. & Vignolini, S. Chiral optics of helicoidal cellulose nanocrystal films. *APL Photonics* **2,** 40801 (2017).

174. Zhang, Y. P., Chodavarapu, V. P., Kirk, A. G. & Andrews, M. P. Nanocrystalline cellulose for covert optical encryption. in (eds. Tabor, C., Kajzar, F., Kaino, T. & Koike, Y.) 825808 (International Society for Optics and Photonics, 2012). doi:10.1117/12.906770

175. Shopsowitz, K. E., Qi, H., Hamad, W. Y. & Maclachlan, M. J. Free-standing mesoporous silica films with tunable chiral nematic structures. *Nature* **468,** 422–5 (2010).

176. Guo, J., Liu, F., Chen, F., Wei, J. & Yang, H. Realisation of cholesteric liquid-crystalline materials reflecting both right- and left-circularly polarised light using the wash-out/refill technique. *Liq. Cryst.* **37,** 171–178 (2010).

177. Querejeta-Fernández, A., Chauve, G., Methot, M., Bouchard, J. & Kumacheva, E. Chiral Plasmonic Films Formed by Gold Nanorods and Cellulose Nanocrystals. *J. Am. Chem. Soc.* **136,** 4788–4793 (2014).

178. Khan, M. K. *et al.* Flexible Mesoporous Photonic Resins with Tunable Chiral Nematic Structures. *Angew. Chemie Int. Ed.* **52,** 8921–8924 (2013).

179. Kelly, J. A., Shopsowitz, K. E., Ahn, J. M., Hamad, W. Y. & MacLachlan, M. J. Chiral Nematic Stained Glass: Controlling the Optical Properties of Nanocrystalline Cellulose-Templated Materials. *Langmuir* **28,** 17256–17262 (2012).

180. Caixeiro, S., Peruzzo, M., Onelli, O. D., Vignolini, S. & Sapienza, R. Disordered Cellulose-Based Nanostructures for Enhanced Light Scattering. *ACS Appl. Mater. Interfaces* **9,** 7885–7890 (2017).

181. Licen, M. *et al.* Correlation between structural properties and iridescent colors of cellulose nanocrystalline films. *Cellulose* **23,** 3601–3609 (2016).

182. Park, J. H. *et al.* Macroscopic Control of Helix Orientation in Films Dried from Cholesteric Liquid-Crystalline Cellulose Nanocrystal Suspensions. *ChemPhysChem* **15,** 1477–1484 (2014).

183. Azzam, F. *et al.* Tunable Aggregation and Gelation of Thermoresponsive Suspensions of Polymer-Grafted Cellulose Nanocrystals. *Biomacromolecules* **17,** 2112–2119 (2016).

184. Chen, Q., Liu, P., Nan, F., Zhou, L. & Zhang, J. Tuning the Iridescence of Chiral Nematic Cellulose Nanocrystal Films with a Vacuum-Assisted Self-Assembly Technique. *Biomacromolecules* **15,** 4343–4350 (2014).

185. Langmuir, I. The Constitution and Fundamental Properties of Solids and Liquids. *J. Am. Chem. Soc.* **39,** 1848–1906 (1917).

186. Langmuir, I. Method of substance detection. (1941).

187. Blodgett, K. B. Films Built by Depositing Successive Monomolecular Layers on a Solid Surface. *J. Am. Chem. Soc.* **57,** 1007–1022 (1935).

188. Iler, R. K. Multilayers of colloidal particles. *J. Colloid Interface Sci.* **21,** 569–594 (1966).

189. Berndt, P., Kurihara, K. & Kunitake, T. Adsorption of poly(styrenesulfonate) onto an ammonium monolayer on mica: a surface forces study. *Langmuir* **8,** 2486–2490 (1992).

190. Bertrand, P., Jonas, A., Laschewsky, A. & Legras, R. Ultrathin polymer coatings by complexation of polyelectrolytes at interfaces: suitable materials, structure and properties. *Macromol. Rapid Commun.* **21,** 319–348 (2000).

191. Nogueira, G. M., Banerjee, D., Cohen, R. E. & Rubner, M. F. Spray-Layer-by-Layer Assembly Can More Rapidly Produce Optical-Quality Multistack Heterostructures. *Langmuir* **27,** 7860–7867 (2011).

192. Svensson, O., Lindh, L., Cárdenas, M. & Arnebrant, T. Layer-by-layer assembly of mucin and chitosan—Influence of surface properties, concentration and type of mucin. *J. Colloid Interface Sci.* **299,** 608–616 (2006).

193. Priolo, M. A., Holder, K. M., Gamboa, D. & Grunlan, J. C. Influence of Clay Concentration on the Gas Barrier of Clay–Polymer Nanobrick Wall Thin Film Assemblies. *Langmuir* **27,** 12106–12114 (2011).

194. Shiratori, S. S. & Rubner, M. F. pH-Dependent Thickness Behavior of Sequentially Adsorbed Layers of Weak Polyelectrolytes. *Macromolecules* **33,** 4213–4219 (2000).

195. Irigoyen, J. *et al.* Responsive Polyelectrolyte Multilayers Assembled at High Ionic Strength with an Unusual Collapse at Low Ionic Strength. *Macromol. Rapid Commun.* **33,** 1964–1969 (2012).

196. Hazel L. Tan, Meredith J. McMurdo, Pan, G., Patten, P. & Van, G. Temperature Dependence of Polyelectrolyte Multilayer Assembly. *Langmuir* **19,** 9311–9314 (2003).

197. Shi, J., Hua, F., Cui, T. & Lvov, Y. M. Temperature Effect on Layer-by-Layer Self-assembly of Linear Polyions and Silica Multilayers. *Chem. Lett.* **32,** 316–317 (2003).

198. Zhang, H., Wang, D., Wang, Z. & Zhang, X. Hydrogen bonded layer-by-layer assembly of poly(2-vinylpyridine) and poly(acrylic acid): Influence of molecular weight on the formation of microporous film by post-base treatment. *Eur. Polym. J.* **43,** 2784–2791 (2007).

199. Wong, J. E., Díez-Pascual, A. M. & Richtering, W. Layer-by-Layer Assembly of Polyelectrolyte Multilayers on Thermoresponsive P(NiPAM- *co* -MAA) Microgel: Effect of Ionic Strength and Molecular Weight. *Macromolecules* **42,** 1229–1238 (2009).

200. Thomas, I. M. Thomas, I. M. Single Layer TiO2 and Multilayer TiO2-SiO2 Optical Coatings Prepared From Colloidal Suspensions. *Appl. Opt.* 2–5 (1987).

201. Chiarelli, P. A. *et al.* Controlled Fabrication of Polyelectrolyte Multilayer Thin Films Using Spin-Assembly. *Adv. Mater.* **13,** 1167–1171 (2001).

202. Cho, J., Char, K., Hong, J.-D. & Lee, K.-B. Fabrication of Highly Ordered Multilayer Films Using a Spin Self-Assembly Method. *Adv. Mater.* **13,** 1076–1078 (2001).

203. Richardson, J. J., Björnmalm, M. & Caruso, F. Technology-driven layer-by-layer assembly of nanofilms. *Science (80-.).* **348,** (2015).

204. Schlenoff, J. B., Dubas, S. T. & Farhat, T. Sprayed Polyelectrolyte Multilayers. *Langmuir* **16,** 9968–9969 (2000).

205. Van Tassel, P. R. Polyelectrolyte adsorption and layer-by-layer assembly: Electrochemical control. *Curr. Opin. Colloid Interface Sci.* **17,** 106–113 (2012).

206. Zhang, G., Dai, L., Zhang, L. & Ji, S. Effects of External Electric Field on Film Growth, Morphology, and Nanostructure of Polyelectrolyte and Nanohybrid Multilayers onto Insulating Substrates. *Langmuir* **27,** 2093–2098 (2011).

207. Barker, S. L. R., Ross, D., Tarlov, M. J., Gaitan, M. & Locascio, L. E. Control of Flow Direction in Microfluidic Devices with Polyelectrolyte Multilayers. *Anal. Chem.* **72,** 5925–5929 (2000).

208. Hamedi, M. *et al.* Nanocellulose Aerogels Functionalized by Rapid Layer-by-Layer Assembly for High Charge Storage and Beyond. *Angew. Chemie Int. Ed.* **52,** 12038–12042 (2013).

209. Kong, B.-S. *et al.* Layer-by-layer assembly of graphene and gold nanoparticles by vacuum filtration and spontaneous reduction of gold ions. *Chem. Commun.* **312,** 2174 (2009).

210. Randhawa, H. Review of plasma-assisted deposition processes. *Thin Solid Films* **196,** 329–349 (1991).

211. Amézaga-Madrid, P. *et al.* Synthesis, structural characterization and optical properties of multilayered Yttria-stabilized ZrO2 thin films obtained by aerosol assisted chemical vapour deposition. *Thin Solid Films* **516,** 8282–8288 (2008).

212. Robles, R. *et al.* Optical properties of large band gap β-In2S3−3xO3x compounds obtained by physical vapour deposition. *Opt. Mater. (Amst).* **27,** 647–653 (2005).

213. Sproul, W. D. Multilayer, multicomponent, and multiphase physical vapor deposition coatings for enhanced performance. *J. Vac. Sci. Technol. A Vacuum, Surfaces, Film.* **12,** 1595–1601 (1994).

214. Hagen, D. A., Foster, B., Stevens, B. & Grunlan, J. C. Shift-Time Polyelectrolyte Multilayer Assembly: Fast Film Growth and High Gas Barrier with Fewer Layers by Adjusting Deposition Time. *ACS Macro Lett.* **3,** 663–666 (2014).

215. Alba, M., Formentín, P., Ferré-Borrull, J., Pallarès, J. & Marsal, L. F. pH-responsive drug delivery system based on hollow silicon dioxide micropillars coated with polyelectrolyte multilayers. *Nanoscale Res. Lett.* **9,** 411 (2014).

216. Dreaden, E. C. *et al.* Bimodal tumor-targeting from microenvironment responsive hyaluronan layer-by-layer (LbL) nanoparticles. *ACS Nano* **8,** 8374–82 (2014).

217. Priolo, M. A., Gamboa, D., Holder, K. M. & Grunlan, J. C. Super Gas Barrier of Transparent Polymer−Clay Multilayer Ultrathin Films. *Nano Lett.* **10,** 4970–4974 (2010).

218. Kim, D. *et al.* Highly Size-Selective Ionically Crosslinked Multilayer Polymer Films for Light Gas Separation. *Adv. Mater.* **26,** 746–751 (2014).

219. Vengatajalabathy Gobi, K. & Mizutani, F. Layer-by-layer construction of an active multilayer enzyme electrode applicable for direct amperometric determination of cholesterol. *Sensors Actuators B Chem.* **80,** 272–277 (2001).

220. Campos, P. P. *et al.* Amperometric Detection of Lactose Using β-Galactosidase Immobilized in Layer-by-Layer Films. *ACS Appl. Mater. Interfaces* **6,** 11657–11664 (2014).

221. Sunny, S., Vogel, N., Howell, C., Vu, T. L. & Aizenberg, J. Lubricant-Infused Nanoparticulate Coatings Assembled by Layer-by-Layer Deposition. *Adv. Funct. Mater.* **24,** 6658–6667 (2014).

222. Du, X., Li, X. & He, J. Facile Fabrication of Hierarchically Structured Silica Coatings from Hierarchically Mesoporous Silica Nanoparticles and Their Excellent Superhydrophilicity and Superhydrophobicity. *ACS Appl. Mater. Interfaces* **2,** 2365–2372 (2010).

223. Patra, D. *et al.* Inorganic Nanoparticle Thin Film that Suppresses Flammability of Polyurethane with only a Single Electrostatically-Assembled Bilayer. *ACS Appl. Mater. Interfaces* **6,** 16903–16908 (2014).

224. Clift, M. J. D. *et al.* Investigating the interaction of cellulose nanofibers derived from cotton with a sophisticated 3D human lung cell coculture. *Biomacromolecules* **12,** 3666–73 (2011).

225. Dong, X. M., Revol, J.-F. & Gray, D. G. Effect of microcrystallite preparation conditions on the formation of colloid crystals of cellulose. *Cellulose* **5,** 19–32 (1998).

226. Jorfi, M., Roberts, M. N., Foster, J. E. & Weder, C. Physiologically Responsive, Mechanically Adaptive {Bio-Nanocomposites} for Biomedical Applications. **5,** 1517–1526 (2013).

227. Sinitskii, A. S., Khokhlov, P. E., Abramova, V. V., Laptinskaya, T. V. & Tretyakov, Y. D. Optical study of photonic crystal films made of polystyrene microspheres. *Mendeleev Commun.* **17,** 4–6 (2007).

228. Giasson, J. Etudes Microscopiques D'Helicoides De Systemes Cellulosiques In Vitro. (McGill University, 1995).

229. Berreman, D. W. Optics in Stratified and Anisotropic Media: 4×4-Matrix Formulation. *J. Opt. Soc. Am.* **62,** 502 (1972).

230. Jones, R. C. A New Calculus for the Treatment of Optical Systems IV. *J. Opt. Soc. Am.* **32,** 486 (1942).

231. Schneider, C. a, Rasband, W. S. & Eliceiri, K. W. NIH Image to ImageJ: 25 years of image analysis. *Nat. Methods* **9,** 671–675 (2012).

232. Klemm, D., Philipp, B., Heinze, T., Heinze, U. & Wagenknecht, W. *Comprehensive Cellulose Chemistry: Fundamentals and Analytical Methods, Volume 1*. (Wiley-VCH Verlag GmbH, 2004). doi:10.1002/3527601929

233. Rusli, R., Shanmuganathan, K., Rowan, S. J., Weder, C. & Eichhorn, S. J. Stress Transfer in Cellulose Nanowhisker Composites—Influence of Whisker Aspect Ratio and Surface Charge. *Biomacromolecules* **12,** 1363–1369 (2011).

234. Shanmuganathan, K., Capadona, J. R., Rowan, S. J. & Weder, C. Bio-inspired mechanically-adaptive nanocomposites derived from cotton cellulose whiskers. *J. Mater. Chem.* **20,** 180 (2010).

235. Kinoshita, S. *Structural Colours in the Realm of Nature*. (World Scientific Publishing Co. Pte. Ltd., 2008).

236. Hewson, D., Vukusic, P. & Eichhorn, S. J. Reflection of circularly polarized light and the effect of particle distribution on circular dichroism in evaporation induced self-assembled cellulose nanocrystal thin films. *AIP Adv.* **7,** (2017).

237. Finlayson, E. D., McDonald, L. T. & Vukusic, P. Optically ambidextrous circularly polarized reflection from the chiral cuticle of the scarab beetle Chrysina resplendens. *J. R. Soc. Interface* **14,** (2017).

238. Yang, Y. C. *et al.* Photonic defect modes of cholesteric liquid crystals. *Phys. Rev. E. Stat. Phys. Plasmas. Fluids. Relat. Interdiscip. Topics* **60,** 6852–6854 (1999).

239. Hodgkinson, I. J., Wu, Q. H., Thorn, K. E., Lakhtakia, A. & McCall, M. W. Spacerless circular-polarization spectral-hole filters using chiral sculptured thin films: Theory and experiment. *Opt. Commun.* **184,** 57–66 (2000).

240. Ye, X. *et al.* Shape Alloys of Nanorods and Nanospheres from Self-Assembly. *Nano Lett.* **13,** 4980–4988 (2013).

241. Schütz, C. *et al.* Rod Packing in Chiral Nematic Cellulose Nanocrystal Dispersions Studied by Small-Angle X-ray Scattering and Laser Diffraction. *Langmuir* **31,** 6507–6513 (2015).

242. Gençer, A., Schütz, C. & Thielemans, W. Influence of the Particle Concentration and Marangoni Flow on the Formation of Cellulose Nanocrystal Films. *Langmuir* **33,** 228–234 (2017).

243. Biyani, M. V. *et al.* Photoswitchable nanocomposites made from coumarin-functionalized cellulose nanocrystals. *Polym. Chem.* **5,** 5501 (2014).

244. Biyani, M. V., Jorfi, M., Weder, C. & Foster, E. J. Light-stimulated mechanically switchable, photopatternable cellulose nanocomposites. *Polym. Chem.* **5,** 5716–5724 (2014).

245. Gevorgyan, A. H. Chiral photonic crystals with an anisotropic defect layer: Oblique incidence. *Opt. Commun.* **281,** 5097–5103 (2008).

246. Kopp, V. I. & Genack, A. Z. Twist Defect in Chiral Photonic Structures. *Phys. Rev. Lett.* **89,** 33901 (2002).